Nanostructured non-precious metal catalyst and its behavior in the catalyst layer in PEM fuel cells

by

Ja-Yeon Choi

A thesis

presented to the University of Waterloo

in fulfillment of the

thesis requirement for the degree of

Doctor of Philosophy

in

Chemical Engineering (Nanotechnology)

Waterloo, Ontario, Canada, 2017

Examining Committee Membership

The following served on the Examining Committee for this thesis. The decision of the Examining Committee is by majority vote.

External Examiner	Dr. Jun Lu Chemist @ Argonne National Laboratory
Supervisor(s)	Dr. Zhongwei Chen Associate Professor
Internal Member	Dr. Michael Fowler Professor
Internal Member	Dr. Aiping Yu Associate Professor
Internal-external Member	Dr. Xianguo Li Professor, PEng

Author's Declaration

This thesis consists of material all of which I authored or co-authored: see Statement of Contribution included in the thesis. This is a true copy of the thesis, including any required final revisions, as accepted by my examiners.

I understand that my thesis may be made electronically available to the public.

Statement of Contributions

The body of this thesis is based on a combination of published work. Various sections are adapted from the following list of publications.

Section 3

JY. Choi, D.C. Higgins, G. Jiang, R. Hsu, J. Qiao, and Z. Chen, Iron-tetracyanobenzene complex derived non-precious catalyst for oxygen reduction reaction, Electrochimica Acta, 2015, 162, 224–229

Mr. Hsu and I carried out the experiments, collected and analyzed the data. Dr. Higgins, Mr. Hsu and I contributed equally to the writing of the paper and Mr Jiang, Dr. Qiao reviewed the manuscript.

Section 4

X. Fu, JY. Choi, P. Zamani, G. Jiang, M.A. Hoque, F.M. Hassan, and Z. Chen, Co–N decorated hierarchically porous graphene aerogel for efficient oxygen reduction reaction in acid, ACS applied materials & interfaces, 2016, 8 (10), 6488-6495

Dr. Hassan and Dr. Fu designed the experiments, and Dr. Fu synthesized the material. Mr. Zamani and I characterized and analyzed the material with Dr. Fu. Mr. Jiang and Dr. Hoque reviewed the manuscript.

Section 5

JY. Choi, L. Yang, T. Kishimoto, X. Fu, S. Ye, Z. Chen, and D. Banham, Is the rapid initial performance loss of Fe/N/C non-precious metal catalysts due to micropore flooding?, Energy & Environmental Science, 2016, In press (DOI: 10.1039/C6EE03005J)

Dr. Yang, Dr. Ye, Dr. Banham and I designed the experiment together. I carried out the lab experiments, collected and analyzed the experimental data with Dr. Banham and assisted with the writing of the paper. Dr. Fu synthesized and supplied the material, and all authors reviewed the manuscript.

X. Fu, P. Zamani, J. Y. Choi, F. Hassan, G. Jiang, D. C. Higgins, Y. Zhang and Z. Chen, In situ polymer graphenization ingrained with nanoporosity in a nitrogenous electrocatalyst boosting the performance of polymer-electrolyte-membrane fuel cells, Advanced Materials, 2016, In press (DOI: 10.1002/adma.201604456)

Dr. Fu and Mr. Zamani synthesized the catalyst. Dr. Fu, Mr. Zamani and I did characterization and analysis of the material, as well as the writing of the paper. Dr. Hassan, Mr. Jiang, Dr. Higgins and Dr. Zhang all contributed in the experimental design and review.

Abstract

Polymer electrolyte membrane (PEM) fuel cells have been viewed as promising power source candidates for transport, stationary, and portable applications due to their high efficiency and low emissions. The platinum is the most commonly used catalyst material for the oxygen reduction reaction (ORR) at the cathode of PEM fuel cells; however, the limited abundance and high cost of platinum hinder the large-scale commercialization of fuel cells. Two approaches being widely accepted to overcome this limitation are 1) to improve Pt utilization to boost the activity while reducing the loading, or 2) to develop non-precious metal catalysts (NPMCs) with sufficient activity and stability to be used in the PEM fuel cells. Of the NPMCs that have been developed, M/N/C (M=Fe, Co) catalysts have gone through several breakthroughs and shown the most promising results until now. Despite the ample amount of research and improvements, the activity and stability of these catalysts must be further improved to be practical in PEMFC applications.

The activity can be further enhanced by several different approaches including but not limited to: 1) use of different dopants (nitrogen, boron, sulfur, etc.) precursors, 2) use of different non-platinum group metals (Fe, Co, Mn), 3) utilizing high surface area support materials and 4) applying heat treatment in various conditions. The combination of these approaches affect the active site density and distribution, electronic structure of the active site thus affecting its kinetics and turn over frequency, electrical conductivity and stability of the catalyst in various ways. Although many researchers have reported promising performance in terms of catalytic activity, there is still enormous demand and potential for the catalysts to improve, especially enhancing its stability in a fuel cell test. Herein, two

chapters are included exploring with the above mentioned combinations to synthesize highly active and stable catalysts, followed by another chapter investigating its fuel cell performance and discussing possible causes of stability loss with a method to verify the issue with flooding of the microporous active sites.

In the first study, non-precious metal oxygen reduction reaction (ORR) catalysts were prepared by pyrolyzing a carbon supported complex consisting of iron acetate coordinated with 1,2,4,5-tetracyanobenzene (TCNB) in an iron phtalocyanine-like polymer arrangement. By employing these small precusursor molecules, it is expected that more uniform and complete coverage of the carbon support material can be obtained, and by using the *in situ* formation and polymerization of FePc, effective iron-center segregation can be achieved. The effect of heat treatment temperature is systematically investigated from 700 to 1000 ^{o}C, with ORR activity investigated by half-cell electrochemical evaluation in 0.1 M $HClO_4$. The highest ORR performance is obtained for the sample heat treated at 1000 ^{o}C, with this sample demonstrating high (> 98 %) selectivity towards the efficient 4 electron reduction mechanism, comparable with some of the best non-precious metal catalysts reported to date. The physical and surface properties of the prepared catalysts were investigated by high-resolution transmission electron microscopy (TEM), x-ray photoelectron spectroscopy (XPS) and thermogravimetric analysis (TGA). After heat treatment, a thin (< 10 nm) coating was observed on the surface of the carbon supports, attributed to residual species remaining from the heat treated precursor complex that provide the source of ORR activity. Decreased nitrogen contents are observed with an increase in heat treatment temperature, concurrent with an increase in the relative concentration of graphitic nitrogen species that likely plays a role in the ORR activity enhancement. The

results suggest that this type of catalyst has great potential used as a non-precious PEM fuel cell catalyst

In the second study, Co-N decorated porous graphene aerogel catalyst was synthesized as an efficient catalyst for ORR. Graphene, consisting of a two-dimensional (2D) monolayer of graphitic carbon atoms, has been viewed as a promising candidate for the fuel cell catalyst support, due to its many intriguing properties such as high aspect ratios, large surface areas, rich electronic states, good electron transport, thermal/chemical stability and good mechanical properties. In the preparation process, polyaniline (PANI) is introduced as a pore-forming agent to aid in the self-assemble of graphene species into a porous aerogel networks, and a nitrogen precursor to induce in situ nitrogen doping. Therefore, a Co-N decorated graphene aerogel framework with a large surface area (485 m^2 g^{-1}) and an abundance of meso/macro pores is effectively formed after heat treatment. Such highly desired structures can not only expose sufficient active sites for the ORR but also guarantee the fast mass transfer in the catalytic process, which provides significant catalytic activity with positive onset and half wave potentials, low hydrogen peroxide yield and remarkable stability that is comparable to commercial Pt/C in acid medium.

The activity of non-precious metal catalysts (NPMCs) has now reached a stage at which they can be considered as possible alternatives to Pt for some proton exchange membrane fuel cell (PEMFC) applications. However, challenges still remain in achieving acceptable stability (performance during potentiostatic or galvanostatic experiments). The most widely reported hypotheses for the instability of NPMCs include de-metalation, protonation/anion binding, and generation of H_2O_2. Recently, it has been proposed that the largest contribution to the instability of NPMCs is from flooding of micropores within the

catalyst particles leading to significant mass transport limitations. While indirect evidence has been obtained that appears to support this hypothesis, no study has yet been performed to directly target micropore flooding. In the last chapter, with a highly microporous catalyst made with dual nitrogen precursors (phenanthroline and polyaniline), a systematic study is performed to investigate micropore flooding in-situ before and after stability testing. The results do not support micropore flooding as being a large contributor to instability, at least for the family of NPMCs evaluated in this work. The protocol outlined here can be used by other researchers in the NPMC community to diagnose micropore flooding in their own respective catalysts.

In summary, this thesis combines both development and investigation from synthesis to an actual fuel cell test with diagnosis, an exploration to find the way to make non-precious metal catalysts commercially viable. Several recommendations for future work were suggested in the last section of this work to further apply the knowledge to design a highly active, durable, and low-cost NPMCs.

Acknowledgements

First of all, I would like to thank my supervisor, Professor Zhongwei Chen, and all my colleagues I've worked with at the University of Waterloo. The opportunities I was given to share ideas and technical knowledge were crucial for making the progress and outcomes.

I'd like to thank my Ph.D. examining committee, including Professor Xianguo Li, Professor Aiping Yu, Professor Michael Fowler and Dr. Jun Lu for their time and contributions. In addition, I would also like to thank Professor Luis Ricardez Sandoval for his participation on my comprehensive proposal examining committee.

I had a valuable opportunity through CaRPE-FC network to spend almost a year in Ballard Power Systems, working with the outstanding members in the CCAT and other research teams including Shanna Knights, Dr. Siyu Ye, Dr. Dustin Banham, and Dr. Lijun Yang. I deeply appreciate the mentorship, scientific knowledge and mental support I was given throughout my last two years of Ph.D. studies.

I also like to acknowledge the support from the funding sources, Natural Science and Engineering Research Council of Canada (NSERC), the Waterloo Institute for Nanotechnology (WIN) and CaRPE-FC network.

Finally, I'd like to acknowledge the help and support I received from families. Without their love and care I would have not been able to make it this far.

Dedication

Dedicated to my amazing wife **Jung Hyun**

and our beloved son **Noel**

for supporting me all the way,

and to my parents for making me who I am.

"If I should live forever

and all my dreams come true,

my memories of love will be of you."

John Denver, 'Perhaps Love'

Table of Contents

List of Figures

List of Tables

List of Acronyms

BET	Brunauer Emmett and Teller
DOE	U.S. Department of Energy
EDA	Ethylenediamine
EDX	Energy Dispersive X-Ray
GDE	Gas Diffusion Electrode
MEA	Membrane Electrode Assembly
NPMC	Non-Precious Metal Catalyst
OCV	Open Circuit Voltage
ORR	Oxygen Reduction Reaction
PEM	Polymer Electrolyte Membrane
RDE	Rotating Disc Electrode
RHE	Reversible Hydrogen Electrode
RRDE	Rotating Ring Disc Electrode
SEM	Scanning Electron Microscopy
TEM	Transmission Electron Microscopy
XPS	X-Ray Photoelectron Spectroscopy
XRD	X-Ray Diffraction

Section 1: Introduction

1.1 Problem Statement

With world's rapid increasing demand for energy and rising awareness for environmental issues, the need for sustainable and environmentally benign energy technology is getting urgent on a global level. The world primary energy consumption is expected to grow by more than 30% from 2013 to 2030, and several studies have indicated that the reserve for the crude oil and gas, the main fossil fuel resources for world energy supply, will near an end within the next 50 years[1, 2]. As one of the most promising renewable energy technologies to resolve the global energy issues, fuel cells, particularly proton exchange membrane (PEM) fuel cells are becoming increasingly popular due to its high energy conversion efficiency, high power density, and environmental benignity. PEM fuel cells are regarded as a very important technology possessing a great potential for various applications including transportation power, micropower, stationary power and other generation applications[3]. However, despite the advantages and focus on the technology, system cost of existing PEM fuel cells are still very high; the majority of the cost comes from the catalyst layer, present at each electrode with the purpose of facilitating the necessary electrochemical reactions, which compromises almost 50 % of the total PEMFC stack cost. While economies of scale may significantly reduce the price of manufacturing PEMFCs, the cost of Pt would likely increase as PEMFC technology is scaled up, being one of the major barriers hindering the large-scale commercialization of fuel cells [4].

Of the two half-reactions occur in the process of generating energy in the fuel cell, and it is known that the reaction happening at the cathode side is prone to high overpotential and slow reaction kinetics compared to the other at the anode, thus becoming the rate limiting reaction [5-7]. To compensate the resulting voltage loss, about 5 times as much as platinum is required for the cathode than the anode, and thus research efforts have been focusing on reducing or eliminating the platinum loading on the cathode catalysts. Finally, during operation, the cathode catalyst materials are exposed to harsh, potentiodynamic and oxidizing conditions that lead to physical, structural and chemical degradation over long periods of use. This inevitably results in only short operational lifetimes of PEMFC systems, limiting their attractiveness towards a variety of different applications. Clearly these are inherent challenges facing the development and commercialization of PEMFC systems that cannot be solved with the current state of catalyst technology. Two approaches have widely been proposed to rectify the issue regarding the efficiency and the cost of the cathode catalyst: (1) increase the utilization or effectiveness of platinum catalysts, so less platinum need to be used, or (2) completely replace platinum catalysts with non-precious metal catalysts.

In the long term, it is far more desirable to take the second approach and completely replace platinum with non-precious metal catalysts as the first approach does not address the issue of limited world supply of platinum. Since the evolution of this type of catalyst began in 1964 by Jasinski, several breakthroughs have led to significant advances in the activity of NPMCs, boosting its potential from being a pure scientific curiosity to become a commercially viable option [8, 9]. However, despite the great advancement in the activity, these catalysts have shown remarkably poor stability and durability. Until now, stable

NPMC performance in a membrane electrode assembly (MEA) for hundreds of hours has been considered a major achievement and it is far less from standard operation times of 5,000 hours and 80,000 hours for automotive and stationary applications, respectively [10]. Based on the current state-of-art NPMCs, it is clear that the future work needs to focus more on finding mitigations for the poor stability since their activity is now enough for low power applications such as distributed generation and backup power.

Although it's difficult to identify one single degradation mechanism for all NPMCs due to the variety of synthetic designs and methods, most common causes could be narrowed down to three mechanisms: 1) protonation of the active site, 2) H2O2 attack and 3) leaching of the non-precious metal catalyst. In addition, one of the degradation mechanisms for NPMCs that's widely accepted and has recently been attracting more scientists' interest is the rapid initial stability loss due to the flooding of the micropores where many scientists believe that the most active catalytic sites are hosted within[11]. Despite the effort to identify the issue with the flooding, limited success has been achieved in quantifying the degree of the micropore flooding and relating that to the measured loss.

In this thesis, first two chapters highlight novel synthesis approaches taken to improve the activity and stability of the catalysts with different precursors and support materials. The last chapter includes synthesis of highly active and micropores catalyst and a series of experiments to directly quantify both the degree of micropore flooding and the resulting impact on the stability.

1.2 Operation Principle

Fuel cells refer to devices that directly convert chemical energy in fuels into electrical energy. There are many types of fuel cells that use a wide variety of fuels and oxidants, but the most common type and of most interest are the fuel cells that use hydrogen and oxygen as the reductant and the oxidant, respectively. In a typical hydrogen/oxygen fuel cell including PEM fuel cell, two gases are supplied into the fuel cell's electrodes, where on anode side the hydrogen is catalyzed generating protons and electrons and on the cathode side protons are combined with oxygen to form water, as illustrated in Figure 1.

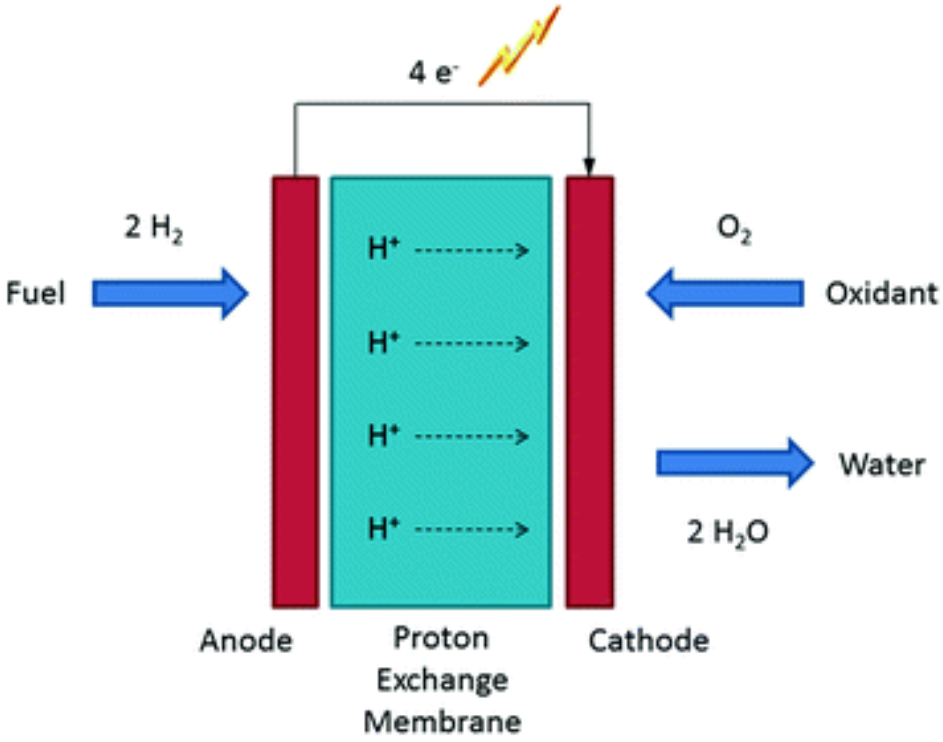

Figure 1: A diagram illustrating the operation principles of a PEM fuel cell device.

Reproduced with permissions from [12]. Copyright © 2010 Springer

The hydrogen gas purged at the anode side undergoes the half-cell reaction described in Equation 1.

$$H_2 \rightarrow 2H^+ + 2e^- \qquad E^0 = 0\ V \qquad (1)$$

Where E^o is the standard half-cell potential based on a reversible hydrogen electrode (RHE). By dissociating a hydrogen gas molecule, two protons and two electrons are generated from this reaction. The electrons travel through the external circuit whereas the protons migrate through the polymer electrolyte membrane inside the cell. Both electrons and protons reach the cathode where they react to combine with the supplied oxygen and form water, following another half-cell reaction as shown in Equation 2 [13].

$$2H^+ + \tfrac{1}{2}O_2 + 2e^- \rightarrow H_2O \qquad E^0 = 1.229\ V \qquad (2)$$

By combining the above two equations together, it gives the overall reaction described in Equation 3:

$$H_2 + \tfrac{1}{2}O_2 \rightarrow H_2O + \text{heat} \qquad E^0 = 1.229\ V \qquad (3)$$

In principle, the only products from this overall fuel cell reaction are water and heat, which makes the fuel cell considered as zero-emission, thus environmentally friendly energy device[13]. Equation 3 can be balanced to show a reaction involving a single oxygen molecule with four protons and four electrons combine to form two water molecules, which is normally referred as 4-electron pathway as described in Equation 4.

$$O_2 + 4H^+ + 4e^- \rightarrow 2H_2O \qquad E^0_{25°C} = 1.229\ V \qquad (4)$$

Ideally, fuel cells can generate power as long as there is continuous supply of each fuel assuming no other side reactions and no catalysts or other components degradation. However, besides the most common and most preferred 4-electron pathway reaction,

another reaction that generates electrons is usually observed simultaneously as shown in Equation 5. This reaction is referred as 2-electron pathway where an oxygen molecule with two protons and two electrons combine to form a hydrogen peroxide.

$$O_2 + 2H^+ + 2e^- \rightarrow H_2O_2 \qquad E^0 = 0.70\ V \qquad (5)$$

The generation of hydrogen peroxide by the 2-electron pathway not only lowers the energy conversion efficiency but also can damage the internal components of the fuel cell by forming harmful radical species[13]. Thus, the degree of the two different pathway reactions should be investigated while evaluating new catalysts and the development of the catalysts should be targeted so that it favors the 4-electron pathway.

Despite boasting a theoretical open circuit voltage of 1.229 V, during actual use, observed voltages are always significantly lower than this value and decreasingly so at higher drawn currents. This is due to a phenomenon referred to as overpotential, or irreversible voltage losses than can be attributed to a variety of different factors. Figure 2 provides an example of a typical PEMFC polarization curve. The first thing that can be noticed from this figure is that the open circuit voltage (no current being drawn) is significantly lower than the theoretical 'No loss' voltage marked by the dashed line. This can be attributed to fuel crossover across the membrane [14], and to some extent, platinum catalyst oxidation.

Moving to the region where current begins to be drawn from the PEMFC, a sharp drop in cell voltage with increasing currents is observed. This region is due to activation overpotential, and is directly related to the slow kinetics of the necessary electrode reactions. This is the most detrimental and important cause of voltage drop in PEMFCs, contributed

primarily by the cathode due to the very sluggish ORR kinetics in comparison to the HOR. Using more effective catalysts with deliberately designed nanostructures can serve to overcome these irreversible voltage losses and is a primary research objective of scientists and engineers.

The region displaying a linear loss of cell voltage with increasing currents in the polarization curve provided in Figure 2 is due to ohmic losses. The sources of resistance in PEMFCs can arise from the polymer electrolyte, the cell connections or the bipolar plates. These issues can be mitigated by appropriate selection of materials, including electrode structures with high conductivity.

Finally, at excessive current densities, the voltage of the PEMFC will drop off dramatically as observed in Figure 2. This is due to the fact that the necessary electrode reactions are proceeding at a rate faster than the reactants can be delivered to the catalyst surface. Using pure reactant feeds, or increased gas pressures can help to mitigate this occurrence, but also using well designed catalyst layer architectures conducive to good reactant flow and accessibility will increase the current densities attainable in a PEMFC system.

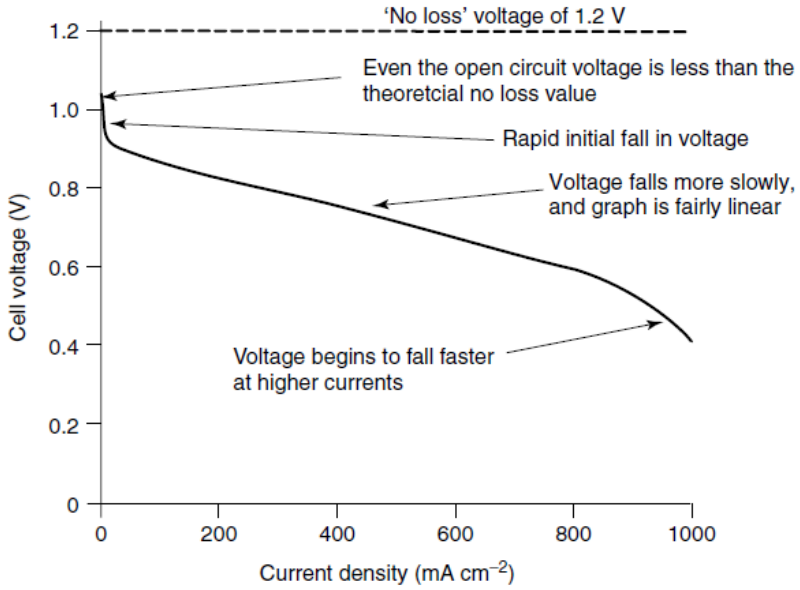

Figure 2: Typical PEMFC polarization curve showing the various regions of overpotential, or irreversible voltage losses. With permission from [14], copyright John Wiley and Sons, 2003.

1.3 Non-precious Metal Catalysts

It was seemed among the scientists that only precious metal catalysts were active for ORR until the early work in 1964 by Jasinski who first discovered that cobalt phthalocyanine was able to reduce oxygen in alkaline media [8, 9]. In 1989, Yeager applied a heat treatment in the presence of nitrogen and transition-metal precursors to achieve a reasonable performance at lower material cost [9]. Since then, the idea of using non-precious metal in the ORR catalyst have drawn a lot of attention in the field of fuel cell catalysts and there has been a significant progress in the performance improvement and understanding of the ORR mechanism on NPMCs.

Despite the ample amount of research being done in the field of NPMCs, it is still unclear as to what kind of active sites exist and of which type is most active. Along with the high temperature heat treatment, it has generally been accepted that a metal precursor is necessary to achieve a reasonable ORR activity. Metal free catalysts for PEM fuel cell application also have been developed in the past, however, the performance achieved is far lower than the ones with metal precursor involved during the synthesis. Some researchers support the idea that the active site exist in the form of Fe-Nx complex, while others claim that the metal precursors only assist in forming the active site but not participate directly in the ORR reaction [15]. Several different types of metals have been studied to work in creating the ORR active catalysts, including Fe [16-23], Co [19-22, 24-28], Ni [20, 24, 27, 29, 30] and Cu [20, 24, 27, 29, 31]. From these findings, the general trend is that Fe tends to show the highest activity among the other non-precious metal precursor. The Co precursor often results in achieving high activity but its durability is poor due to the dissolution in acid media. The optimal loading suggested of these metal precursors is usually very low, ranging from 0.2 to 2 wt.% for the best performance [7]. The metal precursor loading higher than 4 wt.% will most likely lead to forming agglomerates that cause negative outcome upon high-temperature heat treatment as well as can easily dissolve in an ink or electrolyte solution.

Not only the presence of metal precursors but it is also crucial to use nitrogen precursor in synthesizing NPMCs. Many different types of nitrogen precursors have been studied and have been utilized successfully in creating ORR active catalysts. It seems that the more nitrogen content the better the ORR performance it gets, although not many have achieved nitrogen loading over 4 wt.% after high temperature treatment over 700°C. Some

of the popular nitrogen precursors include ethylenediamine [15, 32-36], polyaniline [19, 37, 38], polyacrylonitrile [20, 28, 39-41], acetonitrile [30, 39, 42], and ammonia [43-49].

The carbon support also serves as one of the key factors to influence the overall catalyst performance. Carbon black has been intensively used as a catalyst support due to its low cost, abundance, chemical property, easy-to handle, and electroconductivity. However, with technology development in preparing many novel or low-cost nanostructured materials, many types of carbon supports have also been utilized as support material for the fuel cell catalysts including mesoporous carbons [43, 50-53], carbon nanotubes [54-59], and carbon nanofibres [18, 60-62]. These support materials benefit from having high specific area that are prospective regions for active sites formation and also having high electroconductivity.

In general, the key factors in achieving high ORR activity seem to be choosing the adequate heteroatom precursors and utilizing carbon supports with disordered contents and micropores, while having fairly low amount of Fe or Co precursor and high nitrogen content after synthesis. More detailed information is provided in each chapter in the main section regarding the carbon support materials, types of metal or heteroatom precursors chosen, and synthesis method taken.

1.4 Catalyst Layer Structure and Performance

The current state of electrocatalyst technology consists of uniform sized platinum nanoparticles well dispersed on a high surface area carbon support, commonly abbreviated as Pt/C and illustrated in Figure 3a. The cathode electrode generally consists of a catalyst coated gas diffusion layer (Figure 3b). The gas diffusion layer is a carbon paper or carbon

cloth that serves as the backing for the electrode structure, and also delivers and diffuses the reactant gas over the entirety of the electrode surface.

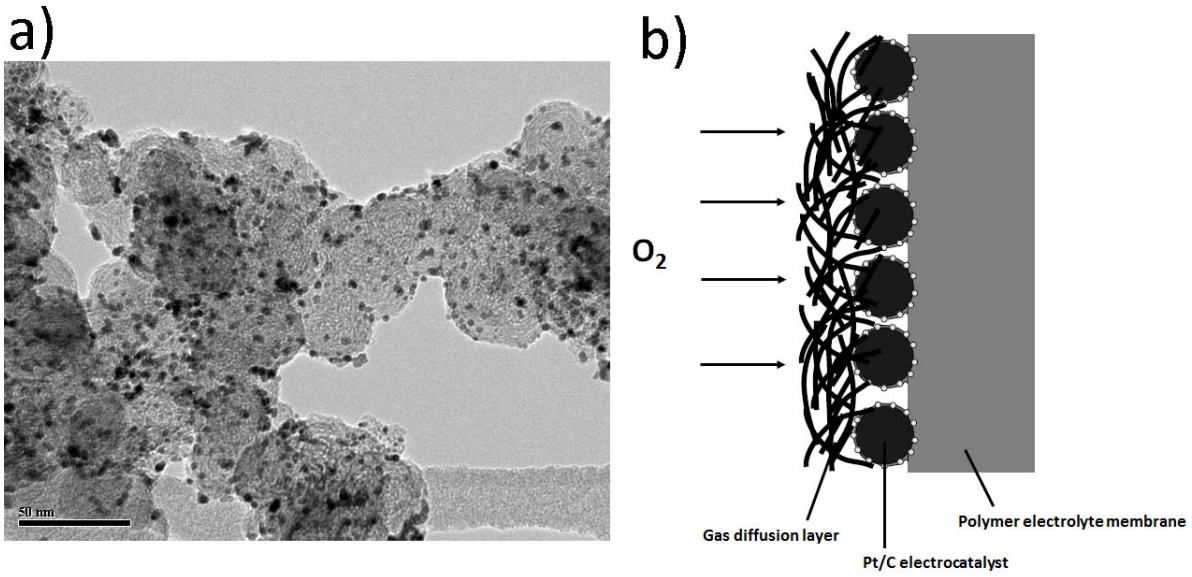

Figure 3: a) Typical image of commercial Pt/C showing platinum nanoparticles (dark spheres) dispersed on a high surface area carbon support. b) Schematic illustration of a cathode catalyst layer in a PEMFC. With permission from [14], copyright John Wiley and Sons, 2003.

As stated previously, the specific type of catalyst utilized will have a direct impact on the activation voltage losses, which have a subsequent impact on the power performance of the devices. Increasing the activity of the electrocatalyst materials towards the ORR will have a marked impact on the overall performance output, effectively reducing the overall platinum requirement, system cost and performance. As a result of activity advances of the NPMCs, recent work has shifted focus towards the optimization of the catalyst layer, as opposed to strictly focussing on ORR activity improvements. This has become a crucial area of work for NPMC researchers, since the much lower ORR activity of NPMCs versus Pt/C has necessitated much thicker cathode catalyst layers (~100 mm for NPMC versus ~12 mm for Pt/C) and it has become widely known that thick catalyst layers result in mass transport

limitations. Thus, it is important to consider that optimizing/controlling the porosity of the catalyst can have a significant impact on the performance of PEMFCs which utilize NPMCs or any novel catalyst at the cathode.

1.5 Electrocatalyst Stability Limitations

During fuel cell operation, the cathode will be exposed to potentiodynamic conditions encountered during drive cycles, through start up and shut down procedures or during periods of fuel starvation. Combined with the acidic nature of the polymeric membrane, humidified conditions and elevated temperature, all of these factors culminate in an environment that is very harsh and electrode materials are very prone to degradation and performance loss over time. As previously discussed, despite the significant advance in the activity, NPMCs suffer from extremely poor stability under these conditions. Although the degradation mechanism for NPMCs is not known with certainty, the main hypotheses are: i) corrosion of the carbon support, ii) oxidative attack by H_2O_2 or the resulting free radicals, iii) dissolution or leaching of the active metal site[63, 64].

Corrosion (or oxidation) of the carbon support has a relatively low reversible equilibrium potential of 0.207 V vs RHE under standard conditions, and is thus thermodynamically favourable at the conditions encountered as the cathode of PEMFCs during operation [65]. Factors including humidity, temperature and the amount of carbon exposure will all play an influential role in carbon corrosion [65, 66], however potential is the primary governing factor. Carbon corrosion is very detrimental to long term fuel cell durability and can be mitigated a variety of different ways. One technique is to use highly graphitized carbon supports, as graphitic carbon is less prone to corrosion than disordered or

amorphous carbon species [67]. This should be considered when designing and synthesizing the NPMCs.

A study was performed in 2003 to investigate the effect of H_2O_2 and the acid treatment on the loss of performance for NPMCs, and the authors were able to demonstrate that exposing their NPMC to a 5 vol % H_2O_2 / 1M H_2SO_4 solution for 5 hours significantly decreased the ORR activity of this catalyst, while exposing it to a 1 M H_2SO_4 solution with no H_2O_2 demonstrated no loss in activity[47]. Based on this research and the fact that many of the NPMCs reported undergo an acid leaching process at temperatures relevant to PEMFCs (80 °C), it is reasonable to conclude that the oxidative attack performs a crucial role in NPMC degradation mechanism than the dissolution / leaching of the active sites and efforts need to be put into minimizing the peroxide and its radicals.

Evidences for the above mentioned degradation mechanisms have been reported and it is likely that all three mechanisms contribute to the stability loss of NPMCs. Recently, a new mechanism regarding flooding of the micropore in the catalysts has been suggested as a major contributor for the rapid initial performance loss seen in many fuel cell tests with high activity NPMCs. However, while some preliminary tests have been done to support this hypothesis, further experiments are needed to accurately measure the degree to which micropore flooding can explain the instability of these NPMCs.

1.6 Organization of Thesis

This thesis explores a several approaches to synthesize non-precious metal fuel cell catalysts for the oxygen reduction reaction (ORR) that are critical for the functionality of a PEM fuel cell, and the breakdown of the projects tasks conducted throughout this thesis is

shown in Figure 4. The thesis is divided into six sections. The first section introduced the reader to the scope and objectives of the work as well as background information in fuel cell catalysis. It contains a literature review on past work done in the field of non-precious catalysts for fuel cells. Section 2 discusses most of the theory and analysis techniques that were utilized in the work included in this thesis. Next two sections focus on novel synthesis approaches to develop NPMCs, first with Fe catalyst with uniformly distributed active sites by employing small nitrogen precursor molecules (Fe-TCNB/C, indicated by red lines in Figure 4), and second with Co with nitrogen doped porous graphene aerogel as a high surface and stable carbon support (Co-N/GA, indicated by yellow lines). The last section includes both synthesis of highly microporous catalyst (Fe-Phen-PANI/C) and investigation on its stability behavior based on the measured degree of micropore flooding, as indicated by green lines in Figure 4. These sections describe the motivation for the work, the experimental procedure, the discussion of the results and the conclusions arrived at. The work described in sections 3 to 5 have been published previously. Section 6 summarizes the important results and some discussion on the future direction that the work may take.

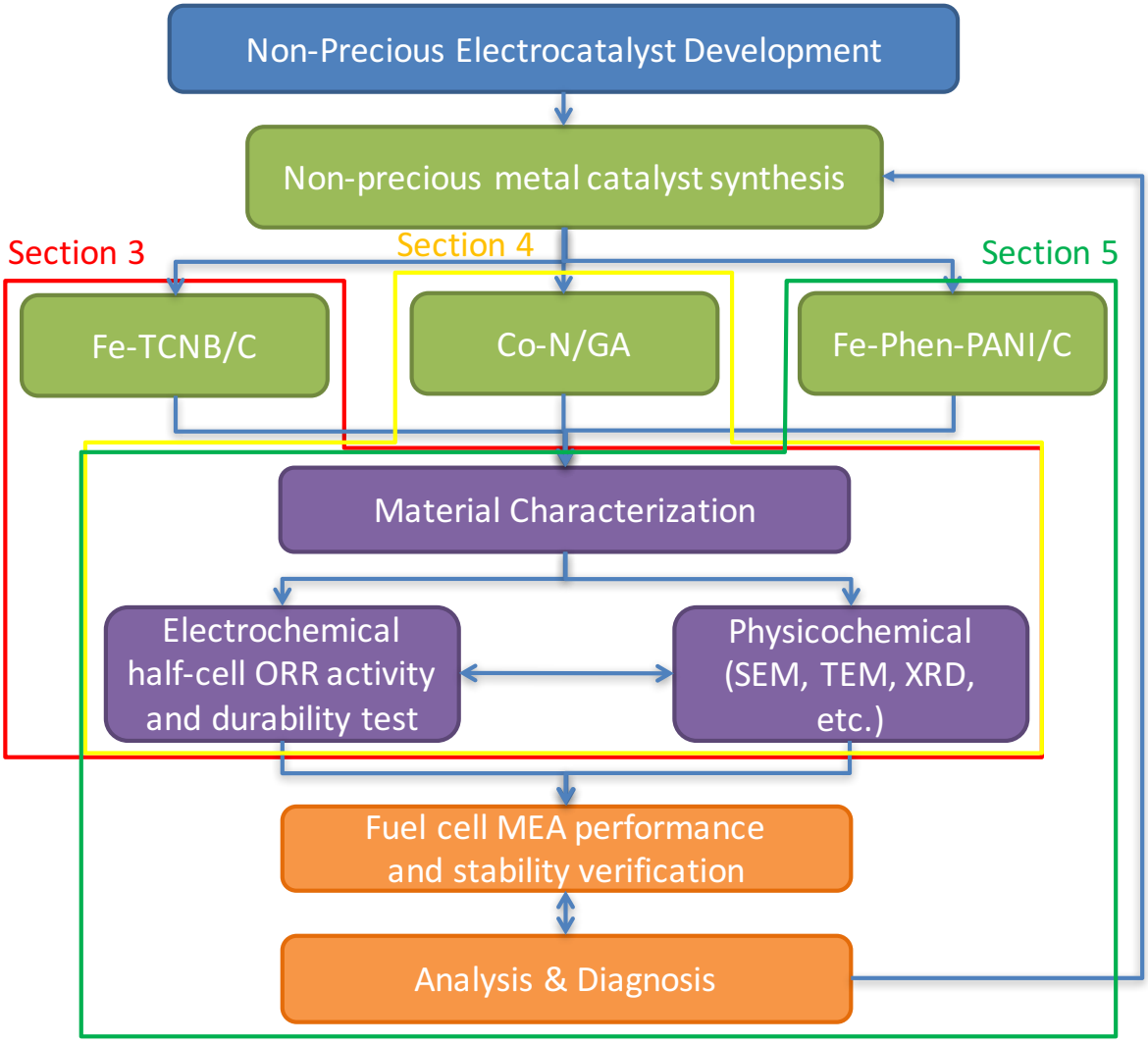

Figure 4: Schematic of the project work flow.

Section 2: Characterization Techniques

Developed electrocatalyst materials will be extensively characterized by a variety of physichochemical and electrochemical techniques with the results correlated to gain insightful feedback. This will allow elucidation of the important factors governing catalytic activity and PEMFC performance, providing fundamental scientific knowledge and aiding in the optimization of developed catalyst materials. This section will illustrate the details regarding several physical and electrochemical characterization techniques that are applied in the research present in this thesis.

2.1 Physical Characterization Techniques

The types of physical characterization techniques discussed in the following sections are scanning electron microscopy (SEM), energy dispersive X-ray (EDX), transmission electron microscopy (TEM), X-ray diffraction (XRD), X-ray photoelectron spectroscopy (XPS), and Brunauer-Emmett-Teller (BET) analysis.

2.1.1 Scanning Electron Microscopy/Energy Dispersive X-Ray

Scanning Electron Microscopy (SEM) is one of the most reliable methods for analyzing solid materials [68]. It is a type of electron microscopy that captures images of the surface of sample by scanning it with high-energy beam of electrons. Since the emitted electrons have smaller wavelength than photons, SEM can achieve higher magnification than optical microscopes and thus very sensitive. Due to this reason the operation requires the sample to be placed under ultra-high vacuum. The emitted electrons hit the atoms of the

sample and their bombardment and interactions with the sample will produce various types of signals, including secondary electrons, back scattered electrons, characteristic X-rays[69]. This happens due to the varying energy levels of the incident electrons. They all contain useful information about the sample's morphology, surface topography, compositions, crystallography and other important physical properties. In the proposed project, SEM will be utilized to investigate the distinct nanostructures of the fabricated electrocatalyst materials. Preparation of samples for SEM imaging involves spreading the powder sample onto carbon tape that is secured to a sample holder stub. This stub can then be placed into the SEM machine, followed by evacuation of the sample chamber and subsequent imaging. The schematic representation of a typical SEM is illustrated in Figure 5.

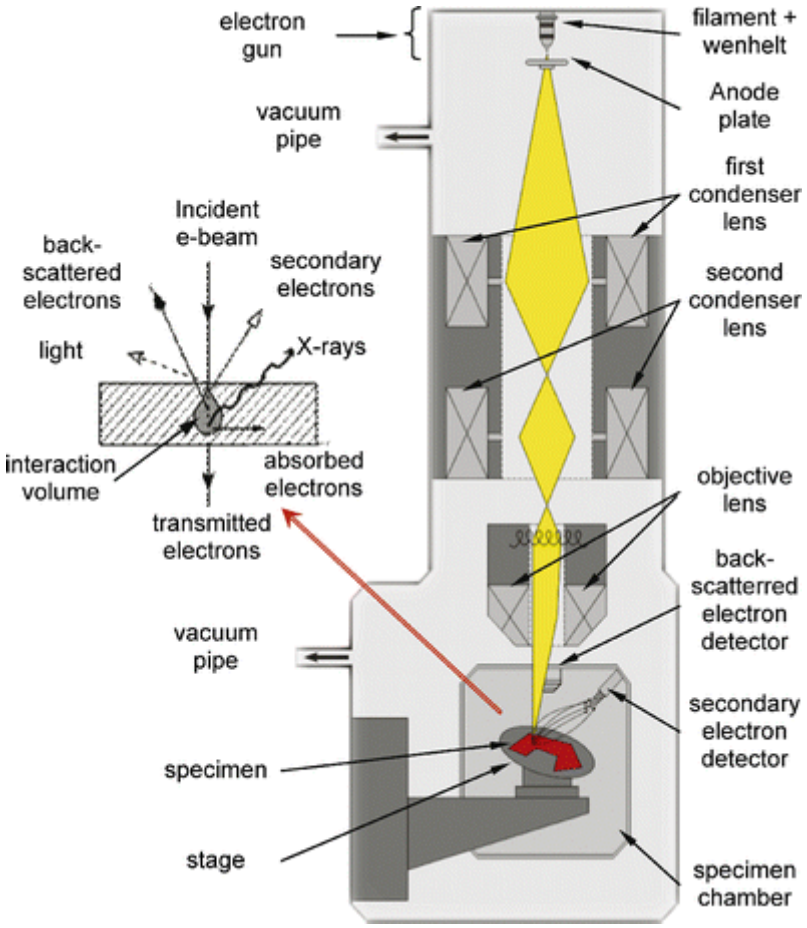

Figure 5: Schematic of a typical scanning electron microscope and imaging process. Reproduced with permissions from [70]. Copyright © 2010 Springer

SEM can be coupled with energy dispersive X-ray (EDX) analysis to determine elemental composition as well as other properties such as electroconductivity of a sample. EDX involves bombardment of electrons onto a materials surface which results in the emission of x-rays collected by a detector. The energy of the emitted x-rays and their corresponding intensity are characteristic of certain elements, allowing their appropriate identification and quantification in the sample being investigated. Elemental mapping is also an interesting technique that can be utilized and involves analyzing the x-rays emitted from localized positions on the sample. For a typical EDX spectrum, it plots the X-ray emission lines of element on the x-axis and the percent composition of those lines on the y-axis.

2.1.2 Transmission Electron Microscopy

Transmission electron microscopy (TEM) is a technique where a beam of electrons is transmitted through and interacts with an ultra-thin specimen [71]. The schematic showing the inner structure of a conventional TEM is shown in Figure 6. The electrons are generated by a process called thermionic emission from a tungsten filament and are aligned and accelerated as they pass through numerous intermediate and projector lenses [72]. An image will be formed from the electrons transmitted through the specimen and it will be magnified and focused by an objective lens. The image produced is the result of beam electrons that are scattered by the specimen versus those that are not.

The main difference between SEM and TEM is the structural information about the sample material they deliver. While SEM is mainly used to visualize the surface topography and morphology of the material sample, TEM is widely used to study the underlying inner structures of the sample material.

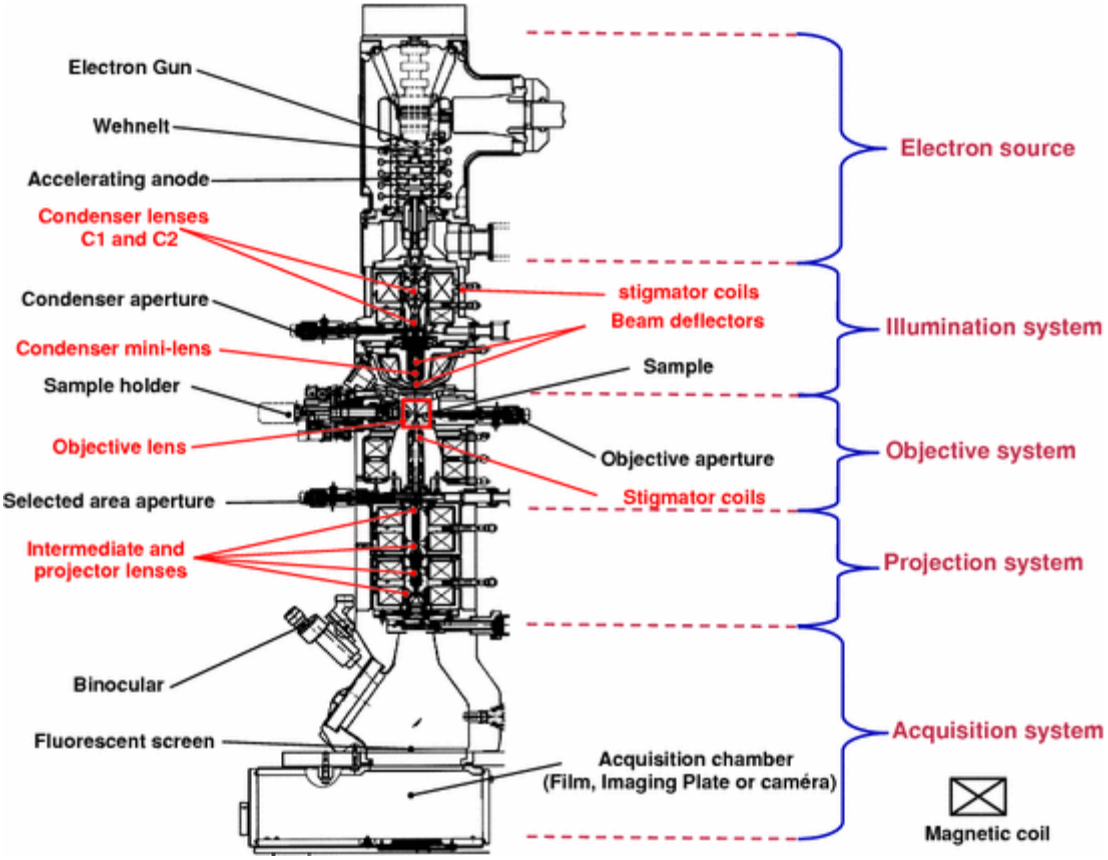

Figure 6: Schematic representation of a column in a transmission electron microscope. Reproduced with permissions from [73]. Copyright © 2010 Springer

TEM is also capable of getting much higher resolution than optical microscopes or SEM due to the small de Broglie wavelength of electrons. The Equation 6 gives the maximum resolution achieved by an optical microscope given the wavelength of a photon.

$$d = \frac{\lambda}{2n \sin \alpha} \tag{6}$$

Where λ is the wavelength of photon, n is a positive integer, and d is the theoretical maximum resolution. If we apply the de Brogile wavelength of electrons, this maximum resolution will increase to a degree that the instrument can distinguish objects in a few nanometer range.

In this study, TEM was utilized to view the surface morphology of the catalyst support materials and to verify the presence of any metal particles.

2.1.3 X-Ray Diffraction

X-ray Diffraction (XRD) is a non-destructive characterization technique that identifies the crystalline phases in materials and measures the structural properties such as chemical composition, grain size, and etc [74]. It also determines the thickness of thin films and atomic arrangements in amorphous materials. There are several types of X-ray diffraction such as single crystal X-ray diffraction, powder diffraction, thin-film diffraction, and high-resolution XRD.

A beam of monochromatic X-rays of known wavelength will be generated by the filament X-ray tubes, by striking an anode (Cu in this case) of a particular metal with high-energy electrons. The incident X-Rays will pass through divergence limiting slit, bombard the sample at a certain angle and reach the detector through a receiving slit. Interaction of X-rays with sample creates secondary diffracted beams of X-rays that are related to interplanar spacings in the powder, according to Bragg's Law (Equation 7):

$$n\lambda = 2d \sin\theta \quad (7)$$

Where n is an integer, λ is wavelength of X-rays, d is the interplanar spacing, and θ is the diffraction angle. The information given by the reflected X-rays is based on the atomic structure of the sample materials which is caused by the elastic scattering of X-rays from the electron clouds of the species within the sample [75].

From XRD spectra, the mean platinum particle size can be easily estimated from Scherrer's equation (Equation 8)

$$d = K\lambda / (B \cos\theta) \quad (8)$$

Where *d* is the particle diameter (nm), *K* is the shape factor, λ is the wavelength of the x-rays (0.154 nm for Cu-Ka), B is the full width at half-maximum (FWHM) of the peak of the interest in radian and θ is the Bragg angle of the peak in degrees. In this study, XRD was applied to obtain the morphology and crystallinity of the carbon materials and to identify the presence and state of metal.

2.1.4 X-Ray Photoelectron Spectroscopy

X-ray photoelectron spectroscopy (XPS) is a quantitative technique that measures elemental composition, chemical states, and electronic states existing in the sample material. The XPS spectra are obtained by irradiating the sample with a beam of X-rays while measuring the number of electrons and the kinetic energy from the material [76].

Conventional XPS instruments utilize a highly focused 20 to 200 μm beams of monochromatic aluminum K-alpha X-rays. Due to the sensitivity of the instrument and to accurately detect the number of electrons, the device must be operated in an ultra-high vacuum to minimize any source of error. XPS can only analyze materials with their atomic numbers equal to or greater than 3 since the orbitals in hydrogen or helium are too small.

This spectroscopy technique is commonly used for materials such ase inorganic compounds, metal alloys, semiconductors, polymers, ceramics, catalysts, and etc [77, 78].

In this work, XPS was utilized to analyze the surface concentrations of various elements including iron, nitrogen and carbon on the catalysts. It was also used to quantify the different types of nitrogen-carbon bonds existing on the catalysts to see which structure is mostly related to the electrocatalytic active sites.

2.1.5 Gas (Nitrogen) Sorption Analysis

Gas sorption analysis utilizes the physical adsorption of gases onto solid materials to measure the specific surface area of the solid. The theory works based on a number of assumptions; adsorption occurs only on well-defined sites of the sample, there is no interaction between the adsorption layers, and the layer number tend to go infinity at the saturation pressure [79]. Gas sorption analysis is very useful for obtaining structural information on the catalyst and its support, especially when the material is porous. The principle of nanotechnology is to increase the reaction sites by increasing the area to volume ratio to achieve superior performance or functionality, thus the specific surface area measured by Brunauer-Emmett-Teller (BET) analysis with the nitrogen adsorption data can possibly become a significant source of evidence. In this work, Gas sorption analysis along with BET measurement was utilized to measure the specific surface areas and pore distributions in the catalysts synthesized in this study.

2.2 Electrochemical Characterization Techniques

To verify the functionality and to investigate the performance of synthesized catalysts, electrochemical measurements are required. The following two sections explain about half-cell measurement and a fuel cell test.

2.2.1 Rotating Disc and Ring Disc Electrode

Both the rotating disc electrode (RDE) experiment and rotating ring disc electrode (RRDE) experiment are one of the most widely used electrochemical characterization technique to test activity of catalysts in the field of fuel cell and other energy technologies. The main difference between the two is that the RRDE has an ability to test hydrogen peroxide generation during the test. The system simulates one of the two electrodes of the fuel cell depending on the supplied gas, but since the cathode catalyst is of the most interest, mainly the cathodic reaction occurs at the tip of the RDE with the supply of oxygen as the fuel. Two other connections, counter electrode and reference electrode are necessary to complete the circuit with the tip of the RDE as the working electrode. All three electrodes are in contact with the electrolyte and a continuous flow of oxygen in the system keeps the electrolyte saturated. The main advantage of using this method over the complete fuel cell test is that it can save cost and time taking to assemble a full cell to test the performance of a newly synthesized catalyst, by evaluating in a simple and easy-to-handle setup.

The schematic illustration for the complete RDE/RRDE system is shown in Figure 7.

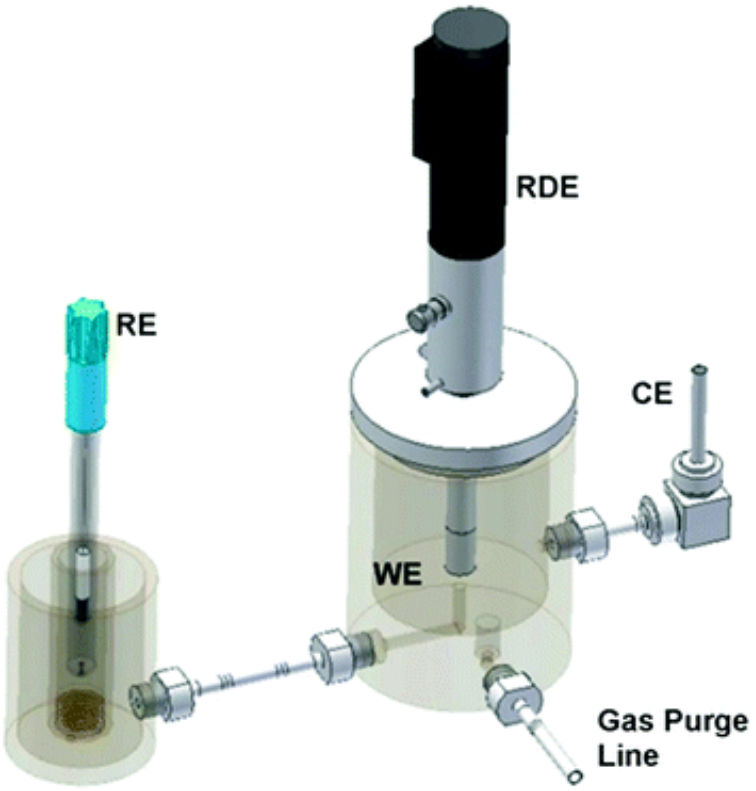

Figure 7: An illustration of an electrochemical half-cell RDE setup. Reproduced with permissions from [12]. Copyright © 2010 Springer

The common type of RDE used in fuel cell catalyst test has a round disc made of glassy carbon, where the sample catalyst ink will be deposited and form a catalyst layer once dried. The rotation feature of this electrode is important since it helps the mass transfer of the oxygen to the electrode surface by creating a laminar flow in the cell. While RDE can carry out most electrochemical measurement on the fuel cell catalyst that are currently being practiced, RRDE adds another ring-type working electrode made of platinum, surrounding the glassy carbon disc. This enables the system to capture a portion of the hydrogen peroxide being generated and give information on the selectivity of the catalyst. The surface schematic of the RRDE is shown in Figure 8.

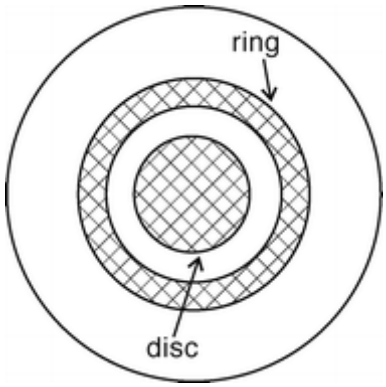

Figure 8: Schematic representation of a RRDE head from a top view. Reproduced with permissions from [80]. Copyright © 2010 Springer

Reduction of oxygen by two different pathways generates H_2O and H_2O_2 simultaneously at the working electrode, and due to the laminar flow all the products are pushed away from the glassy carbon towards the ring. When the ring electrode is held at a certain voltage, it can reduce the H_2O_2 to H_2O and the current change is monitored at the second working electrode. With this information it is possible to analyze the number of electrons transferred during ORR and the percentage of 2-electron pathway reaction over the 4-electron pathway reaction based on the current density difference. This selectivity can be calculated by the following equations [13]:

$$n = 4|I_D|/\left(|I_D| + (|I_R|/N)\right) \quad (9)$$

$$\%H_2O_2 = 100(4 - n)/2 \quad (10)$$

$$\%H_2O = 100 - \%H_2O_2 \quad (11)$$

Where n is the number of electrons transferred, I_D is the current from the disc electrode, I_R is the current from the ring electrode, N is the collection efficiency which is usually indicated by the manufacturer of the instrument, $\%H_2O_2$ is the selectivity of H_2O_2 and $\%H_2O$ is the selectivity of H_2O.

The rate of rotation changes the current of the laminar flow which is correlated to the amount of saturated solution to reach the catalyst surface in a given time. Increase in the rotation speed means higher rate of fuel being supplied at the reaction site. A typical RDE test is done by scanning the potential of the working electrode in a selected range while monitoring the current behavior as plotted in Figure 9. A plot of current density versus potential for a certain range is called ORR curve, and these curves are usually obtained at a set of rotation speeds of 100, 400, 900, 1600 rpm or higher in O_2 saturated acid electrolyte.

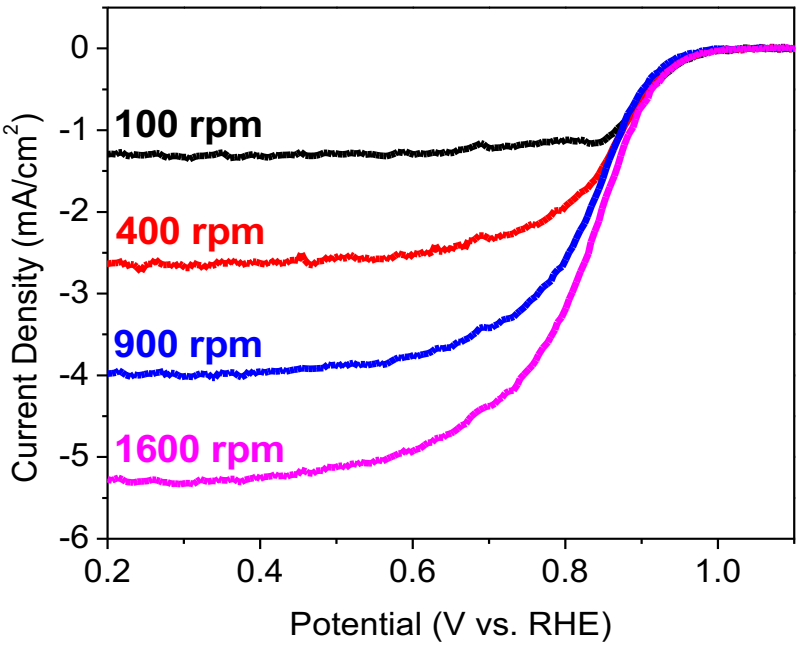

Figure 9: A set of ORR curves with different rotation speeds. Reproduced with permissions from [81]. Copyright © 2012 ECS – The Electrochemical Society

At a point where the oxygen reduction reaction initiates, this potential is called onset potential. From this potential to the point where the overpotential of the reaction does not increase the current density, the reaction is governed by its kinetics [13]. The current density in this kinetic limited region is modeled by Equation 12:

$$|i_k| = nFAk_fC \tag{12}$$

Where i_k is the reaction kinetics controlled current density, n is the number of electrons transferred, F is the Faraday constant, A is the area of the electrode, k_f is a rate constant as a function of the overpotential, and C is the reactant concentration in the bulk solution.

The current obtained at the region in which the current density does not increase upon changing potential is called the limiting current, where the mass transfer is the limiting factor. The model that describes this steady-state diffusion-controlled system is called the Levich equation and is shown in Equation 13.

$$|i_d| = 0.620nFAD^{2/3}\omega^{1/2}\upsilon^{-1/6}C \tag{13}$$

Where i_d is the diffusion controlled current density, n is the number of electrons transferred, F is the Faraday constant, A is the area of the electrode, D is the diffusion coefficient of

reactant in the bulk solution, ω is the angular rate of rotation, ν is the kinematic viscosity, and C is the reactant concentration.

When the catalyst is deposited on the glassy carbon electrode, the ink usually contains Nafion which forms a layer binding the catalyst. The model that describes the diffusion behavior of reactant through the Nafion binding film is shown in Equation 14:

$$\left|i_f\right| = nFAC_f D_f/\delta \tag{14}$$

Where i_f is the diffusion current density of the reactant through the Nafion, n is the number of electrons, F is the Faraday's constant, A is the area of the electrode, C_f is the concentration of reactant in the Nafion film, D_f is the diffusion coefficient of the reactant though the film, and δ is the thickness of the Nafion layer.

The above three equations can be combined to model the overall current density at a specific potential in the diffusion layer near the surface of the electrode. This overall expression for current density is called the Koutecky-Levich equation and is described in Equation 15:

$$\frac{1}{|i|} = \frac{1}{|i_d|} + \frac{1}{|i_k|} + \frac{1}{|i_f|} \tag{15}$$

Where i is the overall or total current density, i_d is the diffusion controlled current density, i_k is the reaction kinetics controlled current density, and i_f is the diffusion current density of the reactant through the Nafion.

The durability of catalysts can be investigated by applying ADT using a half-cell RDE setup. ADT protocols typically involve subjecting catalyst materials to repeated cycles (typically in the range of 1,000-3,000), and then measuring the ORR activity. These transient conditions will induce catalyst deactivation and upon comparison to the initial activities, a gauge of catalyst stability can be provided.

In this work, RDE and RRDE was utilized to characterize the onset potential, half-way potential, limiting current density, and/or H_2O/H_2O_2 selectivity of the synthesized catalysts. RDE was also used to investigate the durability of catalysts by repeated cyclic tests.

2.2.2 Membrane Electrode Assembly Testing

Although the half-cell measurement using the RRDE system is cost and time effective way to test the electrocatalytic activity of catalysts, the information given by the half-cell is limited. The actual fuel cell performance using the catalyst can be quite different than the half-cell test due to many other factors. To verify and see the actual fuel cell performance of the catalyst, membrane electrode assemblies (MEA) can be fabricated and tested in single cell. A MEA consists of a polymer electrolyte membrane contained between an anode and a cathode. The electrode is fabricated by depositing the catalyst onto a GDL, which can be accomplished by a variety of different techniques [82]. Spraying, painting, filtering or electrodepositing the catalyst materials directly onto the GDL several forms of electrode fabrication. The catalyst coated GDLs are then hot pressed together with the electrolyte membrane in order to secure the MEA, ensuring uniform contact and adhesion. Catalysts can also be coated directly onto the electrolyte membrane and secured by hot

pressing. Using different electrode and MEA fabrication techniques will result in variable electrode architectures and resultant performance and durability. The techniques utilized will need to be optimized for the specific catalyst materials under investigation.

After assembling the MEA stack, a polarization curve can be obtained by potential sweep as similar to that of the half-cell test. The performance evaluation will be done by cycling the cell current from open circuit conditions (no current being drawn), to very high current densities. During this testing, the cell voltage is continuously monitored, resulting in a MEA polarization curve similar to the one provided previously in Figure 2. Generally, several cycles will be run before performance evaluation in order to ensure adequate hydration of the electrolytic membrane and activation of the catalyst materials. Many operating parameters can be adjusted including the flow rate for the hydrogen and oxygen, cell temperature, anode temperature, cathode temperature, relative humidity and etc. A typical polarization curve along the power density versus current density plot is shown in Figure 10, using platinum supported on carbon catalyst for both electrodes.

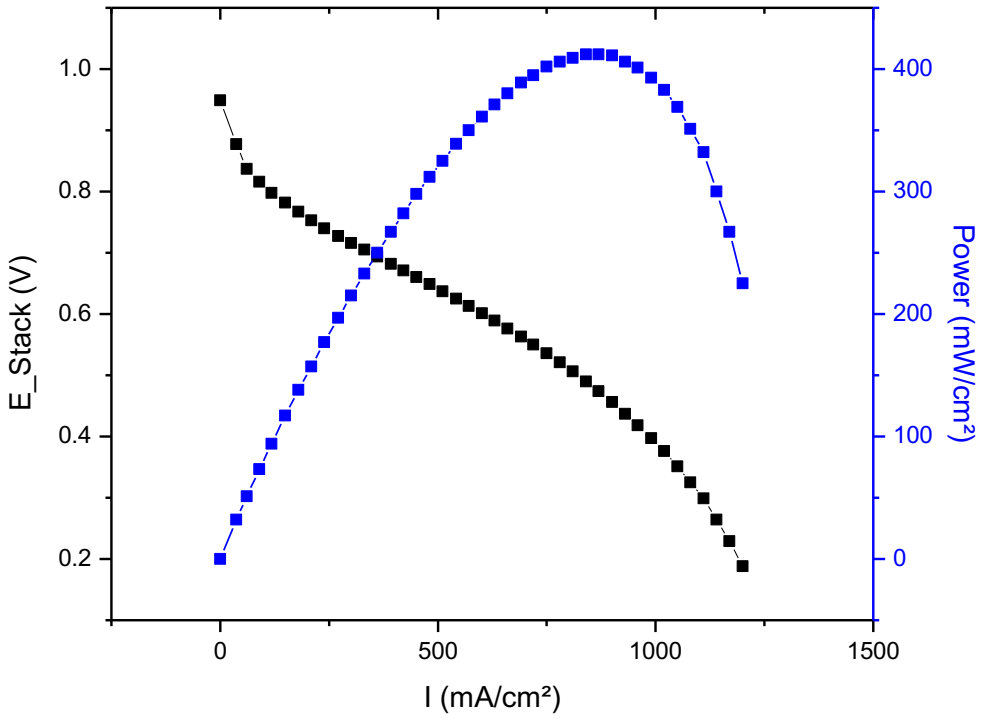

Figure 10: Typical MEA polarization curve with a power density versus current density plot

Section 3: Iron-tetracyanobenzene complex derived non-precious catalyst for oxygen reduction reaction

This chapter is reprinted with permission from Electrochimica Acta.

JY. Choi, D.C. Higgins, G. Jiang, R. Hsu, J. Qiao, and Z. Chen, Iron-tetracyanobenzene complex derived non-precious catalyst for oxygen reduction reaction, Electrochimica Acta, 2015, 162, 224–229

3.1 Introduction

The development of efficient oxygen reduction reaction (ORR) catalysts is essential for the widespread commercialization of polymer electrolyte fuel cells (PEFCs) due to the importance of the reaction kinetics in controlling device performance [83-85]. Platinum and platinum-alloy based catalysts are conventionally used owing to their high intrinsic ORR activity and stability; however the high cost and monopolized global distribution hinders the long term economic feasibility of PEFC systems. This has inspired significant research efforts to the development of low cost, non-precious metal based catalysts to replace platinum-based materials.

Since the initial discovery in 1964 by Jasinski *et al*.[86] that demonstrated cobalt phtalocyanine (CoPc) materials were active for the ORR, significant progress has been made towards the development of transition metal (M = Fe or Co)-nitrogen-carbon complexes, commonly referred to as M-N-C systems. Early investigations illustrated the importance of heat treating transition metal macrocycles at temperatures up to 1000 ºC to realize significant performance and stability gains [87-89]. Years later the discovery was made that

pyrolyzing a mixture of relatively inexpensive transition metal, nitrogen and carbon precursor materials could produce highly active M-N-C catalyst materials [20, 28]. Owing to the heterogeneous complexity of the resulting catalyst structures, there still remains debate in the literature over the exact identity and nature of the catalytically active sites, with contrasting opinions over whether the transition metal species comprises the active site, or merely plays an integral role in active site formation [85]. Regardless, it has been well established that the structure, properties and resulting ORR activity of heat treated M-N-C complexes is directly governed by the particular precursor materials employed and synthetic processes utilized [19, 90-95].

While several catalysts have been prepared by pyrolyzing transition metal-phtalocyanine (i.e. FePc, CoPc) macrocycles absorbed on the surface of carbon supports [96-100], the bulky sheet-like structure of these molecules can arise some challenges including poor dispersion on the carbon support and molecular overlap resulting in iron agglomeration during the heat treatment. Alternatively it is possible to prepare FePc polymer sheets *in situ* from relatively inexpensive iron acetate and 1,2,4,5-tetracyanobenzene (TCNB) [101-103]. By employing these small precusursor molecules, it is expected that more uniform and complete coverage of the carbon support material can be obtained, and by using the *in situ* formation and polymerization of FePc, effective iron-center segregation can be achieved. Herein, we heat treat iron acetate and TCNB adsorbed on the surface of Ketjen black carbon supports at 300 ºC and then subsequently at 400 ºC to promote the formation of polymeric FePc sheets with planar geometry over the carbon support and form strong molecular interactions. After collection, the obtained materials were systematically pyrolyzed at temperatures ranging from 700 to 1000 ºC and then were characterized and investigated for ORR activity in an

acidic electrolyte to determine synthesis-property-performance relationships for this newly developed non-precious catalyst.

3.2 Experimental

3.2.1 Catalyst Synthesis

The Ketjenblack EC-600J (AkzoNobel Corporate) carbon black support was first functionalized by a procedure described in our previous work [104]. Briefly, 5 g of the carbon black was first dissolved into 6 M HCl for 2 hours at room temperature to remove metal impurities. The sample was air filtered and washed with copious amounts of D.I. water. This treatment was followed by refluxing the carbon black in 70% HNO_3 at 80ºC in air for 8 hours before filtering. The precipitate product was washed with copious amounts of D.I. water and dried at 60^{o}C overnight to obtain the functionalized Ketjenblack EC-600J (KJ600).

0.0178 g of TCNB (Sigma Aldrich, 97%) and 0.0174 g of iron(II) acetate (FeAc) (Sigma Aldrich, 95%) were dissolved in 10 mL of quinoline for 30 minutes under N_2 protection and at room temperature. 0.3168 g of KJ600 was added to the mixture and stirred for 30 minutes. Still under N_2 protection, the temperature was raised to 210ºC for 24 hours and continuously refluxed. After cooling, 200 mL of methanol was added to precipitate out the solid, which was then filtered, washed with methanol and dried in an overn at 60ºC overnight. The sample was then heat-treated in a reaction furnace at 300ºC for 1 hour, at 400ºC for 1 hour and finally for 1 hour at a final heat-treatment temperature ranging from 700-1000ºC. N_2 was used to flow through the reaction chamber during pyrolysis. The furnace was allowed to cool before the samples were removed and utilized as the final catalyst product. The catalysts are denoted as Fe-TCNB/C-X where X is the final heat-

treatment temperature. The catalyst obtained without the final heat-treatment is denoted as Fe-TCNB/C-0.

3.2.2 Physicochemical characterization

Catalyst samples were analyzed using TEM through a Philips CM300 operating at 300 kV to observe the surface morphology. A Thermal Scientific K-Alpha XPS spectrometer (150 eV) was used to investigate the relative content of different elements on the surface of the synthesized catalysts. Narrow range XPS scans of the N1s peaks were conducted to determine the relative amounts of each nitrogen species present in the catalysts. TGA was conducted using a TGA Q500 to determine the thermal behaviour of the phthalocyanine polymer formed with TCNB and the thermal stability of each of the catalyst samples. Monochromatic CuKα X-rays were used with an Inel XRG 3000 diffractometer to conduct XRD to observe the crystal structures present in the catalysts. A broad range scan of 2θ from 0.288 – 80.0^{o} was carried out at a rate of 5^{o}min^{-1}. Fourier transform infrared (FTIR) spectra were recorded on a Bruker Tensor 27 FTIR spectrometer in KBr media.

3.2.3 Electrocatalytic Activity Evaluation

Electrocatalytic ORR activity for each synthesized catalyst was evaluated using rotating ring disk electrode (RRDE) voltammetry. The instruments used include a bipotentiostat and a rotation speed controller (Pine Research Instrumentation). The RRDE experiment was carried out in 0.1 M $HClO_4$ electrolyte and using an Ag/AgCl reference electrode. The disk potential was varied from -0.25 to 0.95 V *vs.* Ag/AgCl at a potential sweep rate of 10 mVs^{-1}, and the ring potential was held constant at 1.0 V *vs.* Ag/AgCl. All figures are reported against the reversible hydrogen electrode (V *vs.* RHE).

The catalyst ink deposited on the glassy carbon disk consisted of 4 mg of catalyst suspended in 2 mL of 0.2 wt % Nafion solution. For each RRDE experiment, 40 μL of catalyst ink was deposited onto the glassy carbon electrode with a diameter of 5 mm and allowed to dry. Electrochemical potential sweeps were first conducted with the electrolyte saturated in nitrogen as a background. Bubbling oxygen gas was then used to saturate the electrolyte solution for 30 minutes before potential sweeps were conducted at 1600 rpm to evaluate the ORR activity.

3.3 Results and Discussion

Catalyst morphology and surface structure following synthesis was investigated by TEM with results from Fe-TCNB/C-900 displayed in **Figure 11**. A TEM image of KJ600 pyrolyzed at 900 ^{o}C under N_2 for 1 hour is also obtained and included in Figure 11a to illustrate the morphology change before and after the full synthesis with TCNB. For both KJ600 and Fe-TCNB/C-900, the carbon black support with particle sizes of ca. 30-50 nm in diameter clearly observed, while Fe-TCNB/C-900 catalyst shows a coating layer of less than ca. 10 nm in thickness on the surface. This coating is expected to the residual product remaining after the pyrolysis of the iron and nitrogen precursors that occurs at these elevated temperatures. The coating is relatively uniform over the entire surface of the carbon support materials, indicating that the catalyst synthesis technique utilized was effective in terms of good precursor distribution. The speculated structural transformations occurring between the precursor molecules on the surface of the carbon support are provided in **Figure 12**: (1) nitrogen and iron precursors are first dissolved in quinoline at 210'C to form FePc monomeric units[105], (2) heat-treatment at 300 and 400'C cause the units to polymerize and

adsorb onto the carbon black, and (3) the sheet polymers on carbon support enter a high temperature pyrolysis in N2 which decompose the polymer into active sites of NPMC.

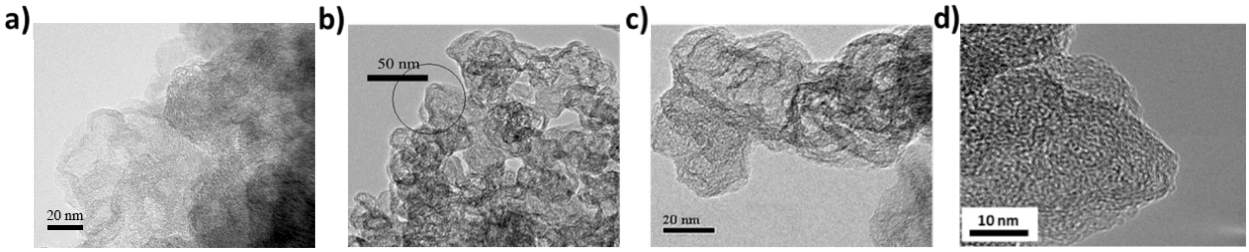

Figure 11. TEM images of (a) KJ600 pyrolyzed at 900 °C and (b) Fe-TCNB/C-900 with area of (c) high resolution TEM image indicated by the black circle.

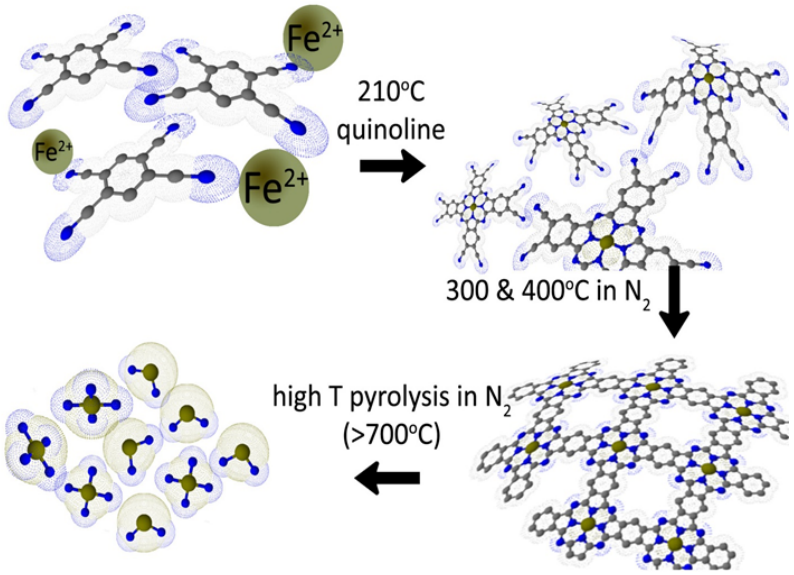

Figure 12. Proposed structural transformations of precursor molecules on the surface of carbon supports during the various stages of catalyst synthesis.

The evidence of metal phthalocyanine structure formation was obtained by using FTIR spectroscopy technique on Fe-TCNB/C-400, a sample undergone a heat-treatment up to 400ºC without any further pyrolysis at higher temperature, and the result is given in

Figure 13. The IR spectrum of Fe-TCNB/C-400 shows strong resemblance to the previously reported metal containing polyphthalocyanines synthesized by using TCNB as the monomer[106]. The peak observed at 911 cm^{-1} is known to be associated with metal ligand vibrations and the wavenumber matches closely with what's previously reported for FePc[107]. The strongest peak oabtained at 1108 cm^{-1} is attributed to C-H bond in plane bending and C_{α}-C_{β} bond stretching in FePc. In addition, a strong peak observed at 1330 cm^{-1} corresponds to C=C or C=N stretching vibrations in the pyrrole ring in the plane of the FePC macrocycle[108-110]. Another strong peak observed at 1517 cm^{-1} contributes to pyrrole rings intense expansion as well as C_{α}-N_c-C_{α} and C-N_m stretching. This provides a strong evidence for a successful formation of FePc structure from TCNB monomers on the carbon support.

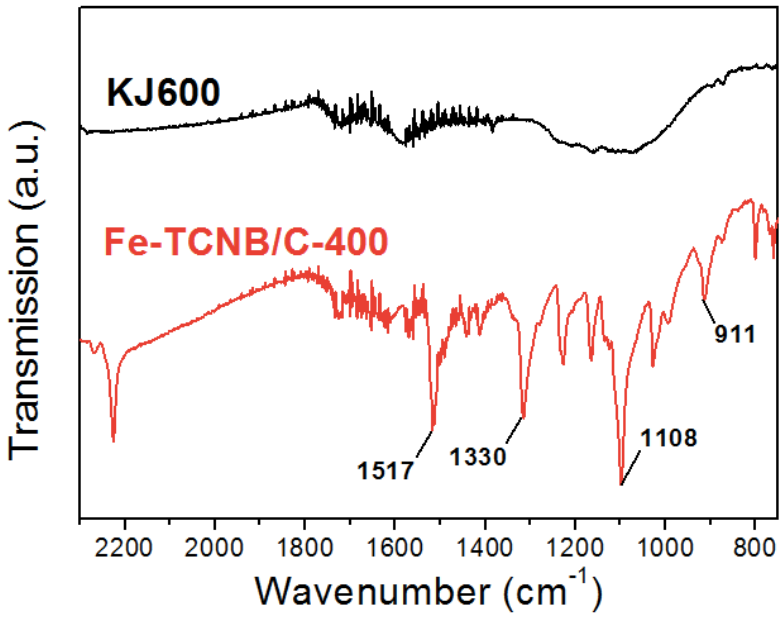

Figure 13. FTIR spectra of KJ600 and Fe-TCNB/C-400 in KBr pellet

XRD was utilized to investigate the crystalline structures existent in the catalyst samples, with patterns shown in **Figure 14** for Fe-TCNB/C-800, Fe-TCNB/C-900 and Fe-TCNB/C-1000. The peak at ca. 25º (denoted with ○) in all the samples is attributed to the

(002) plane reflection of graphitic carbon. The diffraction peaks at 44 and 65º correspond to the (110) plane of α-Fe(denoted with▲) and the (200) plane of α-Fe(denoted with▼), respectively. Fe_3C was also shown to be present in the catalyst structure with characteristic peaks observed at 38, 43 and 78°. The presence of these iron-based crystallites indicate that iron migration and coalescence occurs during the high temperature heat treatment process and is consistent with results of previous reports on M-N-C catalyst development [34, 95, 111].

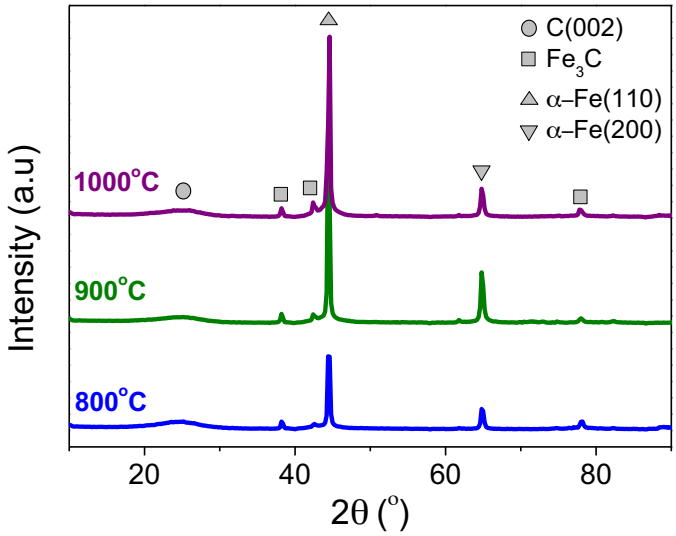

Figure 14. XRD patterns for catalysts synthesized at 800, 900 and 1000 °C.

Elemental surface concentrations for each prepared catalyst material were quantified by XPS and summarized in **Table 1**. All samples displayed similar surface iron contents, which is to be expected owing to the identical nominal iron precursor concentrations used for catalyst preparation. Furthermore, the nominal iron content is more than sufficient to generate good ORR activity (ca. > 0.1 wt. %)[112-114], and should not be a governing factor for the catalysts prepared at different temperatures in this work. It is more likely that the content and identity of the nitrogen dopant species influences ORR activity, an observation that has been reported in several different investigations. At increased heat treatment temperatures

from 700 to 1000 ^{o}C, the nitrogen content was found to decrease from a maximum of 2.79 at. % in Fe-TCNB/C-700, to 1.20 at. % in Fe-TCNB/C-1000. This decrease in nitrogen concentration is a common observation, owing to the instability of some nitrogen species at elevated heat treatment temperatures [33, 115].

Table 1. Surface atomic contents of synthesized catalysts determined by XPS

Catalyst Sample	C	Fe	N	O
	Atomic %			
Fe-TCNB/C-700	94.96	0.06	2.79	2.19
Fe-TCNB/C-800	95.45	0.07	1.94	2.54
Fe-TCNB/C-900	95.18	0.06	1.51	3.25
Fe-TCNB/C-1000	94.70	0.07	1.20	4.03

The high resolution N1s spectra for each sample were de-convoluted into four peaks representing different nitrogen species with results displayed in **Figure 15**. The observed peaks can be attributed to pyridinic (398↔399 eV), pyrrolic (399.9↔400.5 eV), graphitic (401↔402 eV), and oxidized (402↔410 eV) nitrogen species [116-118], with their relative contributions to the N1s peak signal of each sample summarized in **Table 2**. At increased heat treatment temperatures, the relative contents of both pyridinic and pyrrolic nitrogen species decreases, accompanied by a simultaneous increase in the relative content of graphitic nitrogen. This observation is consistent with results from previous reports, and is owing to the increased stability and favourable formation of graphitic nitrogen [119, 120] residing in a six-membered ring formation and residing on the basal plane of graphitic structures.

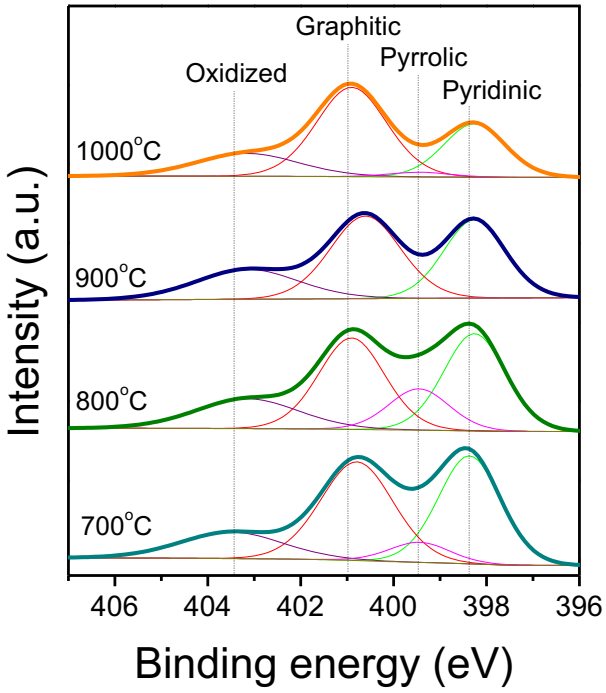

Figure 15. High resolution XPS N1s scans for catalyst materials prepared at various temperatures.

Table 2: Relative nitrogen species contents determined by XPS N1s peak deconvolution

Catalyst Sample	Pyridinic	Graphitic	N-oxide	Pyrrolic
	Atomic % of nitrogen atoms scanned			
Fe-TCNB/C-700	37.69	38.27	15.21	8.82
Fe-TCNB/C-800	34.09	34.29	17.37	14.25
Fe-TCNB/C-900	26.40	45.63	26.29	1.68
Fe-TCNB/C-1000	24.94	51.60	21.10	2.36

To determine and verify the thermal behavior of the proposed polyphthalocyanine structure, TGA under nitrogen was carried out on the pre-pyrolysis material Fe-TCNB/C and

the results are shown in **Figure 16a**. Based on the previously reported thermal decomposition behavior of metal phthalocyanine materials, the weight loss due to the decomposition of the side molecular chains is expected to occur in the range of 220 ~ 500 ‘C and the minor and major decomposition for FePc should occur at 220 and 275 ^{o}C, respectively[121, 122]. For Fe-TCNB/C, it can be observed that the rate of the weight loss increases sharply after initial loss of moisture at 100 ^{o}C and peaks at 240 ~ 260 ^{o}C, which corresponds well to the reported values. This cured Fe-TCNB/C at temperatures around 400 ^{o}C exhibits enhanced thermal stability due to the physical cross-linking points in the polymer matrix and is well maintained until the temperature reaches up to 700 ^{o}C [121, 123]. To evaluate the effect of different pyrolysis temperatures on these structures, TGA under oxygen was carried out on the TCNB-derived catalysts with curves illustrating the percentage weight remaining versus temperature displayed in **Figure 16b**. It can be seen that all TGA curves have a similar shape showing a significant weight loss in the temperature range from 400 to 600 ºC. By investigating the derivative weight change plot shown in **Figure 16c**, four distinct peaks are clearly observed for Fe-TCNB/C-700. The first peak, located at ca. 409 ^{o}C is relatively small and is not observed in the catalyst samples heat-treated at higher temperatures (800 ^{o}C or greater). In nitrogen, it has been shown that iron phthalocyanine macrocycles begin to decompose around ca. 600 ~ 700 ^{o}C [124], thus it hypothesized that the first peak at 409 ^{o}C is due to the combustion of iron phthalocyanine structures which have not been decomposed during the 700 ^{o}C heat-treatment employed during catalyst preparation. Additionally, a small peak at 444 ^{o}C can be seen in the Fe-TCNB/C-700 and Fe-TCNB/C-800 derivative weight change curves, however disappears in the case of Fe-TCNB/C-900 and Fe-TCNB/C-1000. This peak can also be attributed to the

combustion of analogous iron phthalocyanine or intermediate species that remain on the catalyst materials following synthesis. Heat treatments of 900 ^{o}C or above for 1 hour in N_2 was sufficient to fully decompose these species, and hence, this peak is not seen in the samples prepared at these temperatures. The majority of weight loss for all the samples was observed at heat treatment temperatures above ca. 460 ^{o}C. Interestingly the onset of this weight loss is shifted to higher temperatures with the increase of catalyst heat treatment temperature. This indicates that the thermal stability of the catalyst materials are increased under these conditions, most likely arising due to a more graphitic carbon structure formed at higher synthesis temperatures [125].

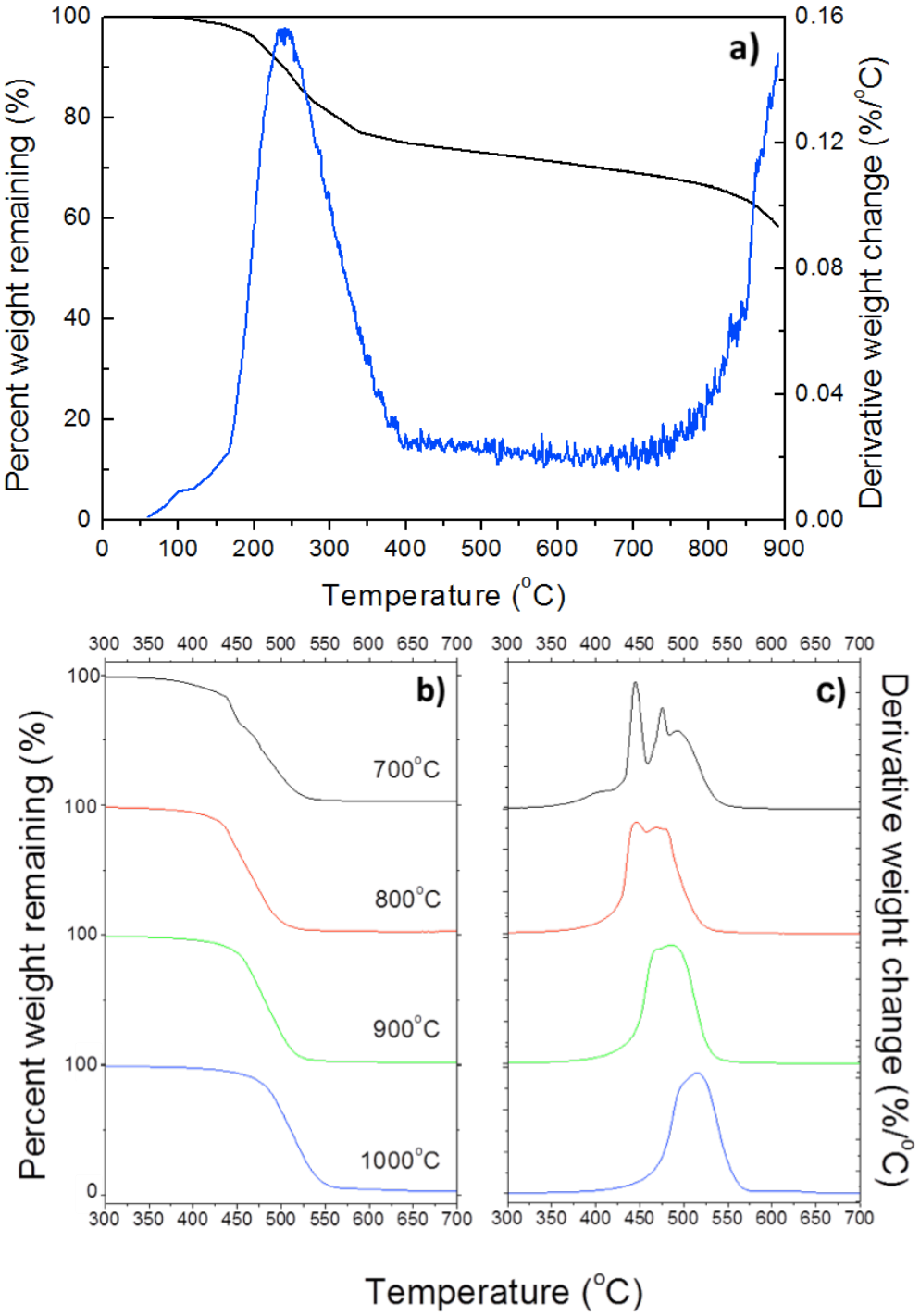

Figure 16. TGA data obtained (a) under nitrogen environment for Fe-TCNB/C (pre-pyrolysis) sample; (b) under oxygen environment for various post pyrolysis samples showing percent weight remaining and (c) derivative weight change versus temperature.

The ORR activity of the prepared catalysts was evaluated by RRDE in 0.1 M $HClO_4$, with results depicted in **Figure 17a**. All ORR curves present in the figure have been corrected by removing the background signals obtained in N_2 saturated electrolyte. For the sample prepared in the absence of a high temperature pyrolysis, negligible ORR activity is observed, highlighting that the high temperature heat treatment is essential for inducing high catalytic activity. For the catalysts heat-treated at increasing temperatures from 700 to 1000 ºC, a clear performance increase is observed in terms of ORR on-set potential and mass transport limited current densities (**Table 3**). By processing ring current data, the selectivity of the prepared catalysts towards the overall 4 electron reduction of oxygen was determined and displayed in **Figure 17b**. Consistent with the trend observed in terms of ORR activity, increased heat treatment temperatures resulting in higher selectivity towards the 4 electron reduction mechanism. Approximately 98.5 % selectivity towards the formation of water is achieved on Fe-TCNB/C-1000 at an electrode potential of 0.4 V *vs.* RHE, a value that is consistent with some of the best non-precious metal catalysts reported to date [19]. The increase in ORR activity observed with increased pyrolysis temperatures can likely be linked to the complete decomposition of the FePc-like structures formed by the processing of iron acetate and TCNB on the surface of the functionalized carbon supports. Interestingly, an increase in ORR activity and selectivity towards the 4 electron ORR mechanism is observed with an increased relative content of graphitic nitrogen present in the materials. This suggests that the formation of graphitic nitrogen may play a possible role towards enhancing ORR activity, however stringent investigations are still required in order to elucidate the exact identity and structure of active site(s) present in M-N-C catalyst materials.

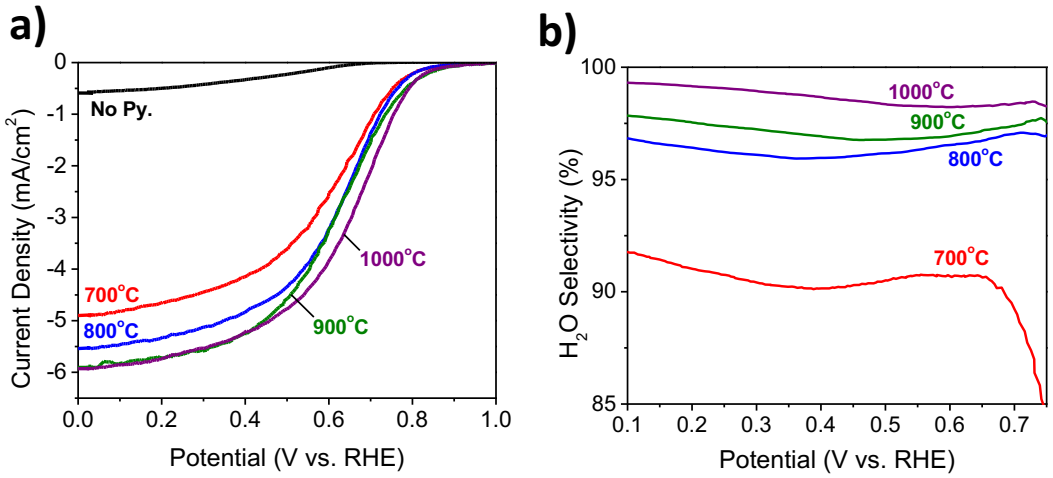

Figure 17. (a) ORR polarization curves and (b) H_2O selectivities for catalysts prepared at various temperatures obtained at 1600 rpm in O_2 saturated 0.1 M $HClO_4$.

Table 3. ORR performance parameters for synthesized catalysts

Catalyst	Current Density at 0.4 V *vs.* RHE ($mAcm^{-2}$)	Onset potential (V *vs.* RHE)	H_2O Selectivity at 0.4 V *vs.* RHE (%)
Fe-TCNB/C-0	0.33	0.60	--
Fe-TCNB/C-700	4.15	0.84	90.2
Fe-TCNB/C-800	4.84	0.84	96.1
Fe-TCNB/C-900	5.25	0.87	97.1
Fe-TCNB/C-1000	5.26	0.88	98.5

3.4 Conclusions

ORR active non-precious metal catalysts were prepared by heat treating a carbon supported iron-TCNB complex at temperatures ranging from 700 to 1000 ºC. The highest ORR activity in 0.1 M $HClO_4$ was observed for Fe-TCNB/C-1000 catalyst, demonstrating an onset potential of ca. 0.88 V *vs.* RHE and a 4 electron reaction selectivity greater than 98 % at all electrode potentials investigated, a value comparable with some of the best non-

precious metal catalysts reported to date. Based on high-resolution TEM imaging, the observed ORR likely arises from a thin (< 10 nm) surface layer formed during the heat treatment of the surface coordinated iron-TCNB complex. Additionally, at higher pyrolysis temperatures, decreased nitrogen contents were observed along with an increase in the relative concentration of graphitic nitrogen species that likely play an important role in the catalytically active site structure(s).

Section 4: Co-N Decorated Hierarchically Porous Graphene Aerogel for Efficient Oxygen Reduction Reaction in Acid

This chapter is reprinted with permission from ACS applied materials & interfaces.
X. Fu, JY. Choi, P. Zamani, G. Jiang, M.A. Hoque, F.M. Hassan, and Z. Chen, Co–N decorated hierarchically porous graphene aerogel for efficient oxygen reduction reaction in acid, ACS applied materials & interfaces, 2016, 8 (10), 6488-6495

4.1 Introduction and Motivation

Currently, the proton exchange membrane (PEM) fuel cell, owing to its high fuel efficiency and zero emissions at the point of operation, represents one of the most promising energy conversion technologies.[126] For widespread commercialization of PEM fuel cell, one crucial factor is reducing the high cost caused by the exclusive use of expensive platinum-based catalysts at the cathode, due to the slow kinetics of the oxygen reduction reaction (ORR).[127-129] Therefore, searching for efficient and less expensive non-platinum catalysts (NPC) for ORR is extremely desirable to commercialize the clean operating, efficient electrochemical devices.[130-134]

Recent intense research efforts towards replacing platinum-based catalysts have shown that nitrogen doped carbon nanomaterials could act as effective ORR catalysts, due to their low cost, excellent electrocatalytic activity, long durability and their environmental friendliness.[135-139] Among them, graphene based carbon materials have attracted great interests for exploring alternative ORR catalyst due to its exceptional chemical and physical properties such as theoretically ultrahigh surface areas, superior conductivity and excellent

mechanical/chemical stability.[140-145] However, most of the nitrogen-doped graphene materials which show promising ORR performance in alkaline electrolyte suffer from relatively low activity in acid medium, making them less competitive than commercial Pt/C catalyst. The introduction of transition metals (e.g. Fe, Co) to the above mentioned graphene matrix results in metal-nitrogen-carbon (M-N-C) based NPC further enhances their ORR activity in acid media.[146, 147] Although the nature of the catalytically active sites in these NPC remains elusive,[148-150] quantum mechanical calculations and experimental investigations have both suggested that M-N moieties, in which metal cations coordinated to pyridinic nitrogen atoms, play a vital role in catalyzing the ORR.[151-154] In addition, according to previous report that one of the limitations for enhancing the catalytic activity of these catalysts is due to low density and utilization of M-N active sites as well as poor mass transport properties.[155] Thus, turning to large surface area and high porosity graphene structures to afford both abundant accessible M-N catalytic sites and suitable channels for mass transport is a potential solution to produce advanced ORR catalysts.[156]

It is well known that, due to the inherent property of 2-dimensional materials, graphene sheets are easily tend to irreversibly planar stacking. This severe agglomeration thereby leads to a drastic loss of the high intrinsic specific surface areas, which results in inaccessibility of electro-active sites for catalysis and inferior mass transfer. To improve the utilization of active sites and facilitate mass transfer through the volumetric entirety of graphene-based catalysts, various strategies have been explored to prevent the stacking between individual graphene sheets. Spacer blocks such as carbon nanotubes,[157] metal nanoparticles and templates were inserted between graphene sheets to prevent their stacking.[158, 159] Different physical and chemical treatments have also been employed to

acquire porous frameworks that suppress their agglomeration.[160-163] However, the use of hazardous reagents or the tedious synthesis procedures result in low production yield and high cost. Besides, the goodish electrochemical performance still needs to be improved. Based on the above considerations, high ORR performance materials are expected for example by designing and constructing interesting graphene framework enveloping a high surface area and suitable porosity as well as more active M-N moieties. It will be certainly great if such a novel graphene structures could be fabricated through a simple but efficient way.

Here, we report a Co-N moieties decorated graphene aerogel (Co-N-GA), which has unique hierarchical pores, large surface area and an abundant of potential Co-N active sites. A combined hydrothermal self-assemble, freeze-drying and pyrolysis process was employed to efficiently prepare this porous graphene framework. Specifically, polyaniline (PANI) is carefully selected as pore-forming agent to aid in the self-assembly of graphene oxide (GO) species into a highly porous hydrogel structure, while also being an effective nitrogen precursor due to its unique chemical structure.[164-166] The as-fabricated graphene aerogel was used as a catalyst to achieve several merits, including: 1) to maximize the Co-N active sites density; 2) to maximize the utilization of active sites; 3) to facilitate good transfer of reactant and product. Benefiting from these excellent structural properties, the Co-N-GA exhibits impressive electrochemical performance in acid medium.

4.2 Experimental

4.2.1 Synthesis of Graphene Oxide (GO)

GO was prepared from graphite powder using an improved method reported previously by Marcano et al.[1] Briefly, 2 g of graphite powder was added to 400 mL of a 9:1 volumetric mixture of concentrated H_2SO_4/H_3PO_4 in an ice bath. 18 g of KMnO4 was then added slowly and the reaction was heated to 50 °C and held for 12 hours. Deionized (DI) water (400 mL) then was slowly added to the mixture. Lastly, 15 mL of H_2O_2 (30%) was added in order to complete the oxidation reaction, and the final mixture was centrifuged to separate out the solids which were washed thoroughly with water, ethanol and HCl (30 %); followed by lyophilization.

4.2.2 Synthesis of Co-N-GA

In a typical experiment, a 30 mL of GO (2 mg mL^{-1}) aqueous solution containing $Co(NO_3)_2 \cdot 6H_2O$ (15 mg) and PANI (80 mg) was sonicated for 1 h to form a stable complex solution. Subsequently, the stable suspension was sealed in a Teflon-lined autoclave and hydrothermally treated at 180 °C for 12 h. After that, a columnar hydrogel was lyophilized to prevent the agglomeration of graphene sheets during the drying process. The maintained monolithic architecture was then heated at 900 °C for 1 h under Ar. The heat-treated sample was then pre-leached in 2 M H_2SO_4 at 80 °C for 24 h to remove unstable and inactive species from the catalyst, and thoroughly washed in de-ionized water. Finally, the catalyst was heat-treated again in Ar at 900 °C for 3 h referred to as "Co-N-GA" catalysts. For comparison, the Co-N modified graphene sheets (Co-N-GS) catalyst was prepared with a slightly modified approach. In the case of Co-N-GS, a 120 mL of dilute

d GO (0.5 mg mL^{-1},) aqueous dispersion with cobalt salt (15 mg) and PANI (80 mg) was prepared, and then followed the same synthetic procedures. Due to the relative low concentration of GO solution, an amorphous precipitation instead of a hydrogel is formed during the hydrothermal treatment. N-GA was prepared with the same procedures as Co-N-GA but without cobalt salt. GA was also prepared with the same procedures as Co-N-GA but without PANI and cobalt precursors.

4.2.3 Electrochemical Measurements

Surface morphologies of samples were investigated using SEM (LEO FESEM 1530) and TEM (TEM, JEOL 2010F). X-ray diffraction (XRD) measurements were recorded with Bunker AXS D8 Advance. Surface area and pore size were determined by a surface area and porosity analyzer (Micromeritics Instrument Corp. ASAP2020). XPS spectra were collected using a Thermal Scientific K-Alpha XPS spectrometer. Raman spectroscopy was carried out on a Bruker Senterra Raman Microscope operating with a wavelength of 532 nm.

4.2.4 Electrochemical Measurements

Electrochemical experiments were conducted on a workstation (Pine Instrument Co., AFCBP-1) assembled with a rotation speed controller (Pine Instrument Co., AFMSRCE) using a conventional three compartment electrochemical cell. Ag/AgCl electrode (3 M KCl) and graphitic electrode were used as reference and counter electrode, respectively. All potentials in this study were converted to RHE scale. A rotating ring-disk electrode (RRDE) with a Pt ring (5.52 mm inner-diameter and 7.16 mm outer-diameter) served as the working electrode. The catalyst ink was prepared by dispersion the catalyst powder (10 mg) with 1 mL 1-Propanol in an ultrasonic bath for 2h. Then 12μL of the catalyst ink was pipetted onto

the glass carbon surface and dried thoroughly in air, after that 3μL of 0.05wt% Nafion solution was dropped onto the catalyst layer, leading to a catalyst loading of approximately 0.6 mg cm^{-2}. The ORR activities were measured in O_2 saturated 0.5 M H_2SO_4 and 0.1 M KOH from 1.0 V to 0.0 V with a scan rate of 10 mV s^{-1}. For detecting H_2O_2 formed at the disc electrode, the ring potential in the RRDE system was set to 1.20 V (*vs* RHE). Commercial Pt/C (TKK, 28.2 wt. % Pt) with a Pt loading of 20 μg cm^{-2} was measured in 0.1 M $HClO_4$ and 0.1 M KOH electrolyte for comparison. Accelerated degradation testing (ADT) was carried out by cycling the electrode potential 5000 times under nitrogen saturated electrolyte between 0.6 V and 1.0 V *vs* RHE at a scan rate of 50 mV S^{-1}.

4.3 Results and Discussion

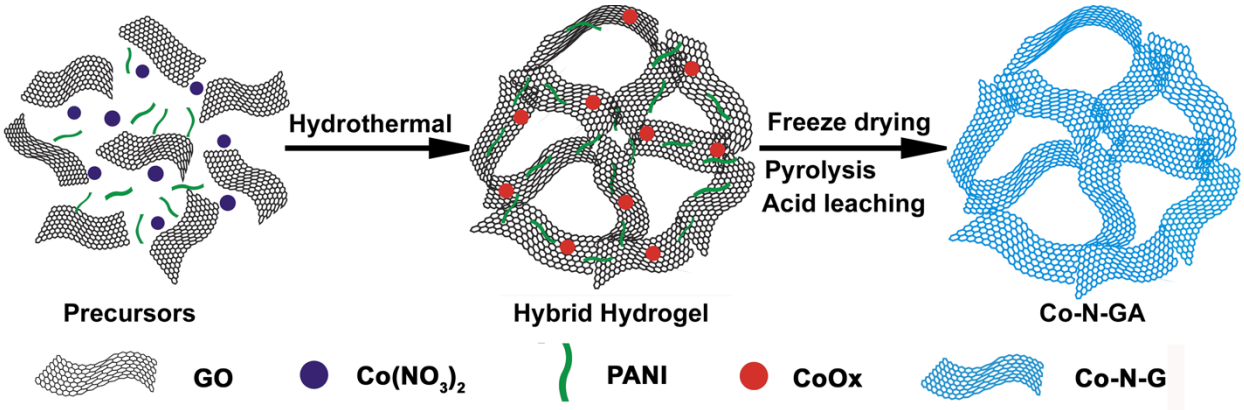

Figure 18. Illustration of the synthetic route for the Co-N-GA catalyst.

The fabrication process for Co-N-GA is demonstrated in Figure 18. In the first step, a stable aqueous suspension containing graphene oxide (GO), $Co(NO_3)_2 \cdot 6H_2O$ and PANI (Figure 19a) was hydrothermally treated to synthesize a graphene-based hybrid hydrogel (Figure 19b). Subsequently, a freeze drying and pyrolysis process was applied to obtain the aerogel with a monolithic architecture (Figure 19c). Finally, the as-prepared aerogel was pre-leached in 2 M H_2SO_4 to remove unstable and inactive species from the catalyst, and

then pyrolyzed again to yield the Co-N-GA. Here, the PANI serves two important functions in preparing the Co-N-GA catalyst. First of all, it helps with the assembly of graphene to form a spongy hydrogel, owing to the hydrogen bonding and π-π interactions with GO during the hydrothermal treatment which can prevent the restacking of GO so as to form a hierarchical porous structure. Otherwise, in the absence of PANI, a much smaller and compact GO hydrogel was formed due to the aggregation of GO sheets (Figure 19d). Second, it acts as an efficient nitrogen doping agent, owing to its high N/C atomic ratio (0.17) and unique aromatic structure which can facilitate the incorporation of nitrogen-containing active sites into the graphene matrix.[167] Meanwhile, along with the decomposition of PANI during the pyrolysis process, a large amount of nitrogen containing gas was released, which could further expand the graphene sheets to have fewer-layer and increased porosity.

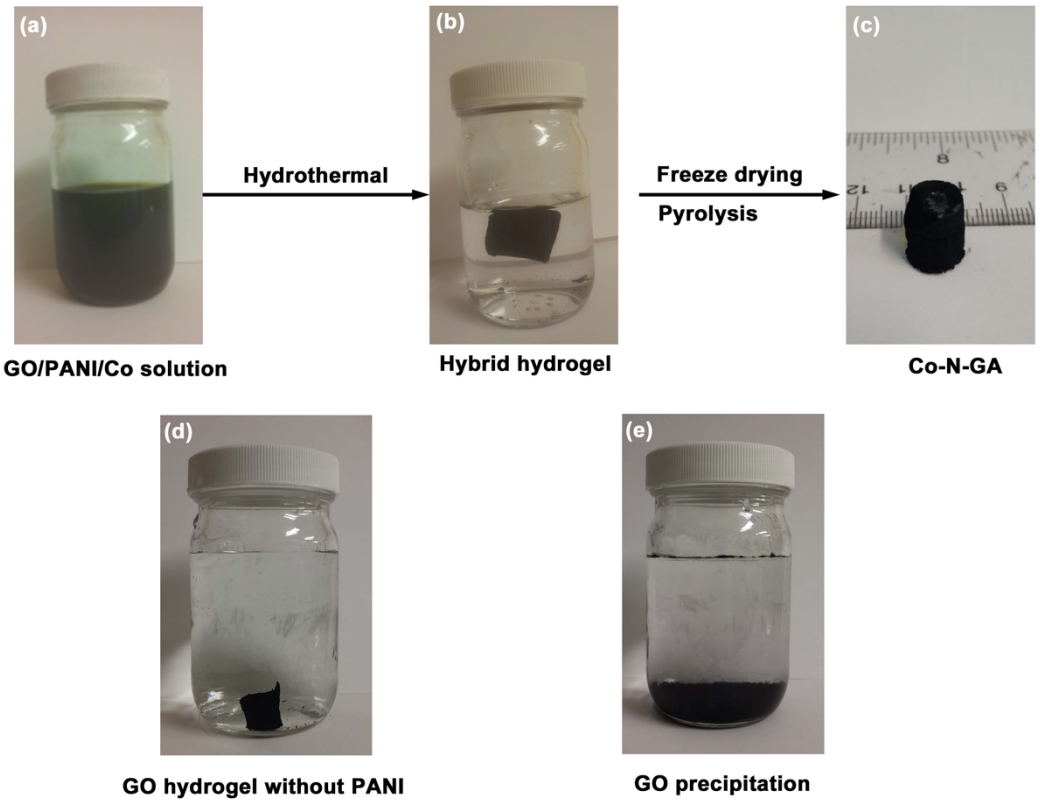

Figure 19. (a), (b) and (c): fabrication process for the porous Co-N-GA catalyst; (d): the GO hydrogel prepared in the absence of PANI and cobalt salt; (e): GO based precipitation.

The morphology and microstructures of Co-N-GA were first investigated by scanning electron microscopy (SEM) and transmission electron microscopy (TEM). SEM imaging reveals large amount of open-pore structures that continue through the graphene framework (Figure 20a). Meanwhile, the magnified SEM image indicates the existence of numerous smaller pores contiguous with large pores (Figure 20b). These SEM results definitely certify that the Co-N-GA with an interconnected porous network was successfully prepared. This morphology is beneficial for a catalyst. Such a porous graphene skeleton could maximize the exposure of active sites to participate in the ORR process. Meanwhile, during the ORR process, these robust interconnected pores could function as arteries that shorten the diffusion length of reactant and product.[168] To investigate the utilization of the pore structures, graphene-sheet-based Co-N-GS catalyst was also prepared. In contrast to Co-N-GA with loose porous networks, Co-N-GS exhibits a relatively agglomerated structure, which is disadvantageous for the contact of oxygen, electrolyte and active sites (Figure 21). TEM characterization of Co-N-GA reveals almost transparent wrinkled surface characteristic of graphene, while some composite carbon structures which result from the carbonization of PANI and cobalt are also observed (Figure 20c). The high resolution TEM (HRTEM) image of Co-N-GA further indicates the presence of graphitic carbon shells which are commonly observed from acid leached M-N-C catalysts (Figure 20d).[169, 170] The graphitic carbon shell structures are likely to result in improved ORR performance due to the increased exposure of sites responsible for oxygen adsorption and fast electron transport.[159]

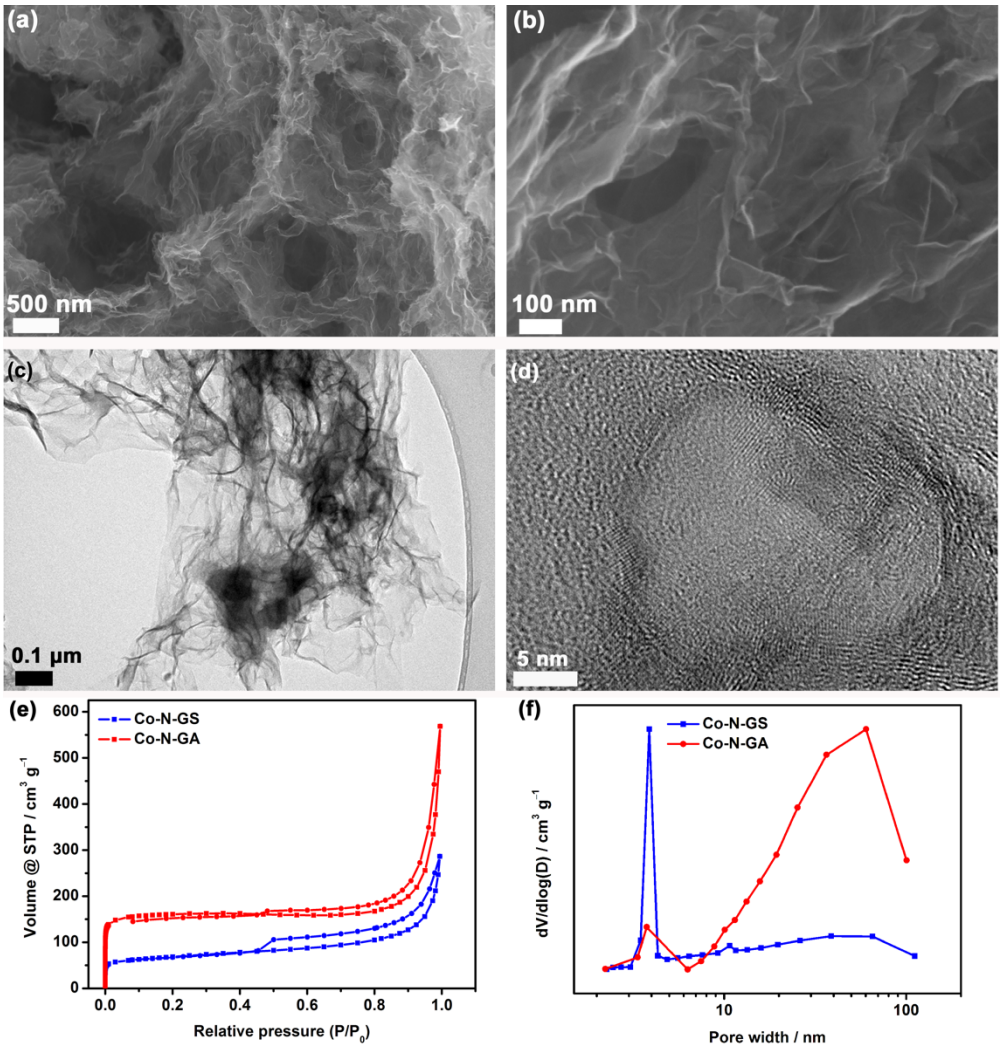

Figure 20. (a), (b) SEM and (c), (d) TEM images of as-obtained Co-N-GA. (e) N_2 sorption isotherms of Co-N-GS and Co-N-GA catalysts, and (f) the pore size distribution from the BJH method of corresponding samples.

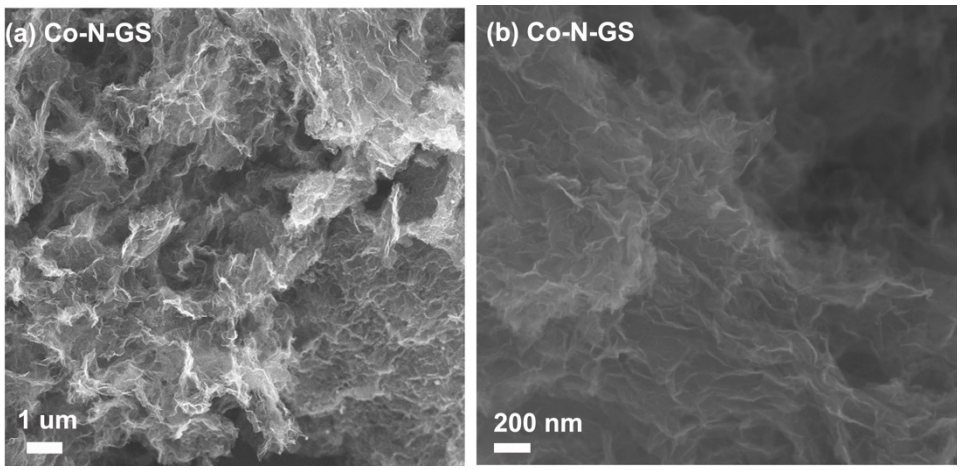

Figure 21. (a), (b) SEM images of Co-N-GS

The Brunauer−Emmmett−Teller (BET) analysis of nitrogen adsorption−desorption isotherms reveal that both the plots of Co-N-GS and Co-N-GA show close to a type IV patterns with a H3 hysteresis loop according to IUPAC classification (Figure 20e). The absence of saturation at a relatively high pressure indicates the presence of macro-pores and the rapid rise at low pressure region also indicates the presence of micro-pores. Meanwhile, the hysteresis in the middle pressure range suggests the existence of slit-type meso-pores structure typically formed by aggregates of lamellar graphene sheets. The detailed pore structure parameters of Co-N-GS and Co-N-GA are summarized in Table 1. Remarkably, the specific surface area of Co-N-GA is approximately 485 $m^2 g^{-1}$, which is about two times higher than that of Co-N-GS (222 $m^2 g^{-1}$). Such high surface area graphene structure could achieve high volumetric surface area therefor maximize the active site density to improve ORR performance. The pore size distribution (calculated by Barrett–Joiner–Halenda method) clearly shows the presence of multiple porosities ranging from a few nanometers to the near micrometer scale (Figure 20f). It is worth noting that the Co-N-GA shows predominantly

macro-pores (53%), while in Co-N-GS the macro-pores account for only 29% of the overall pores volume (Table 4). It is reported that the macro-pores could shorten the diffusion length of reactive molecules thus improve the ORR performance.[171] It is therefore expected that the presence of numerous large pores could provide superior electrochemical performance for Co-N-GA.

Table 4. Pore structure parameters of Co-N-GS and Co-N-GAa

Samples	S_{BET}	V_{total}	V_1	V_2	V_3
	$m^2\ g^{-1}$	$cm^3\ g^{-1}$	$cm^3\ g^{-1}$	$cm^3\ g^{-1}$	$cm^3\ g^{-1}$
Co-N-GS	222	0.41	0.11	0.18	0.12
Co-N-GA	485	0.71	0.05	0.29	0.37

[a]S_{BET}: the BET specific surface area; V_{total}: the total pore volume; V_1: the volume of micro-pores (< 2 nm); V_2: the volume of meso-pores (2–50 nm); V_3: the volume of macro-pores (50–100 nm).

Raman spectroscopic and X-ray diffraction (XRD) measurements were employed to characterize the physical structures of the graphene based samples. As can be seen in Figure 22a, two peaks at around 1350 and 1580 cm^{-1} corresponding to the well-defined D band and G band,[172] respectively, were obtained. In comparison to GO, the increased I_D/I_G intensity ratio of N-GA, Co-N-GS and Co-N-GA illustrates their increased disordered feature that caused by nitrogen-doping effect. X-ray diffraction (XRD) pattern in Figure 22b only show broadened peak around at 23°, corresponding to the (002) planes of carbon materials. No obvious diffraction peak of Co phases or its oxides can be observed. This shows that the majority of large inorganic cobalt particles were most likely removed during the acid leaching step, and any particles that may remain or too small or present in amounts too low to be detected.

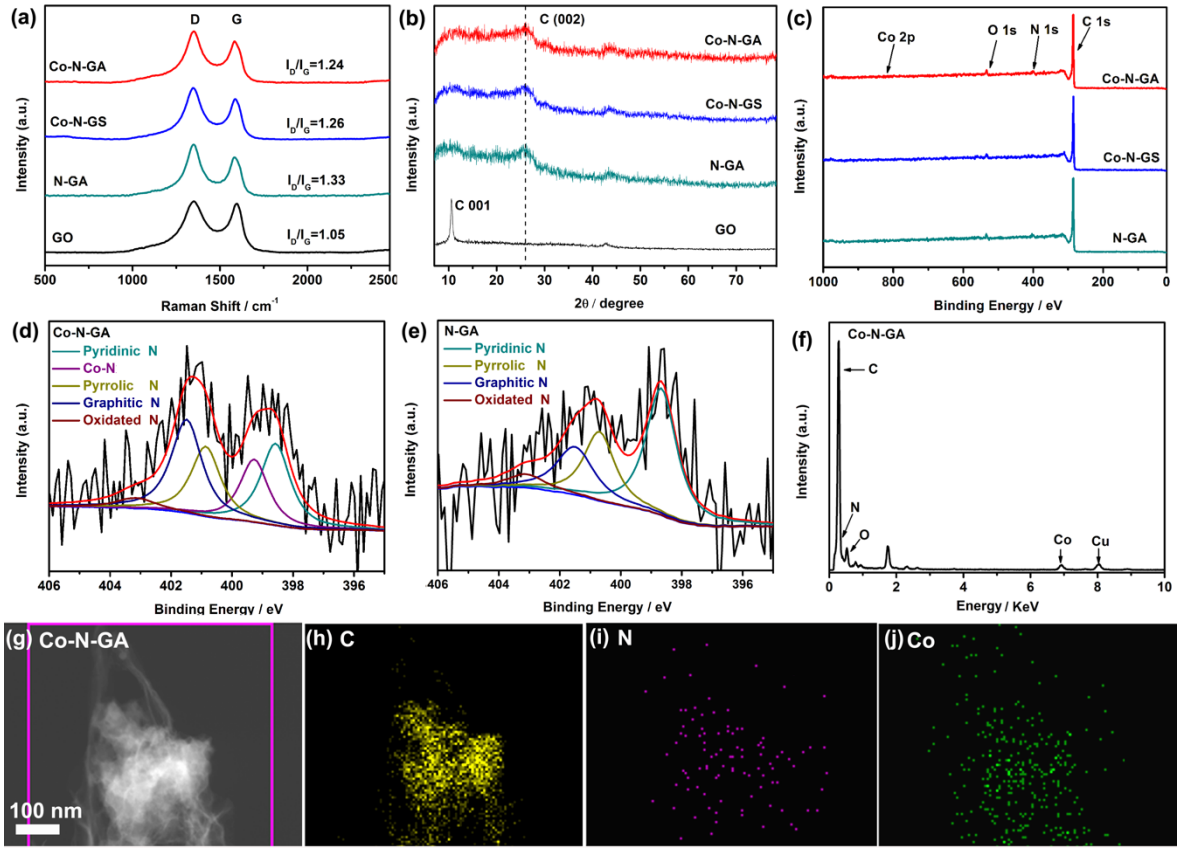

Figure 22. Raman spectra (a) and XRD patterns (b) of GO, N-GA, Co-N-GS and Co-N-GA; (c) XPS survey of N-GA, Co-N-GS and Co-N-GA; (d) and (e) High resolution N 1s peak of the resulting Co-N-GA and N-GA; (f) EDX spectra of Co-N-GA; (g) STEM image of Co-N-GA and corresponding elemental mapping images of (h) C, (i) N and (j) Co.

X-ray photoelectron spectroscopy (XPS) measurements were further carried out to probe the chemical compositions and contents of the materials. The measured survey spectra of Co-N-GA and Co-N-GS clearly reveal the presence of C, O, N and Co peaks (Figure 22c, Figure 23). Table 5 outlines the atomic surface concentrations with only small differences observed between the two catalysts. The high resolution N 1s spectra of the two Co-N modified catalysts were deconvoluted into five different peaks with binding energies of 398.6, 399.3, 400.9 401.5 and 403.2 eV, corresponding to pyridinic N, Co-N, pyrrolic N,

graphitic N and oxidated N, respectively (Figure 22d, Figure 23a, Table 6).[173, 174] Here, the assignment to the Co-N type of N species is based on previous investigations of pyrolyzed metal-containing macrocycles.[175] Specifically, Co-N moieties are proposed as a complex in which a cobalt cation is coordinated to two or four pyridinic-type nitrogen atoms that are doped in carbon matrix.[176, 177] Moreover, in the Co 2p range (Figure 23b−c), a peak centered at 781.8 eV could be related to Co-N structures due to cobalt cation associated with N atoms,[53] which goes well with the corresponding peak detected in the N 1s spectrum due to Co-N species. For comparison, the N 1s of nitrogen doped graphene aerogel (N-GA) was peak-fitted with four peaks, due to the absence of no meaningful Co-N species at ~399 eV because this catalyst was prepared without cobalt precursor (Figure 22e, Table 5).[178] The detailed peak-fitting results of the N 1s were listed in Table 6, and such different N-bonding configuration should exert a significant influence on their catalytic performances. In particular the Co-N functionalities, which are proposed as the most likely active sites play an important role for the ORR activity in acidic medium.

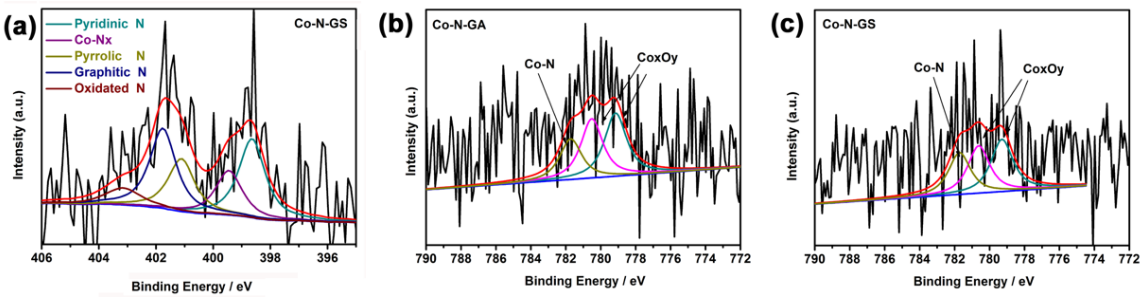

Figure 23. High resolution N 1s peak of the (a) Co-N-GS; (b) and (c): High resolution Co 2p peak of the Co-N-GA and Co-N-GS.

Table 5. Elemental composition of the samples obtained from XPS results.

Samples	C (at.%)	N (at.%)	O (at.%)	Co (at.%)
N-GA	93.80	2.86	3.34	---
Co-N-GS	94.63	2.57	2.52	0.29
Co-N-GA	94.54	2.10	3.12	0.24

Table 6. Atomic concentrations (at.%) of heterocyclic N components of samples in the N 1s binding energy region (398 ~ 405 eV).

	Pyridinic N	Co-N	Pyrrolic N	Graphitic N	Oxidated N
	~398 eV	~399 eV	~400 eV	~401 eV	~402−404 eV
N-GA	43.75%	---	25.2%	24.5%	6.5%
Co-N-GS	26.3%	17.9%	18.9%	28.6%	8.2%
Co-N-GA	25.8%	18.7%	21.4%	29.8%	4.2%

Energy-dispersive X-ray spectroscopy (EDX) was also employed to further probe the elements and their locations in Co-N-GA. First, EDX pattern in Figure 22f confirmed the presence of elemental C, N, O and Co in Co-N-GA, in agreement with the XPS results. The EDX elemental mapping was performed to further identify the distribution of elements in this catalyst. Unexpectedly, Co species were detected along with C, N and O elements all uniformly distributed throughout the graphene structure (Figure 22h−j). Such finely dispersed Co species could possibly coordinate with the N atoms to form Co-N moieties which are suggested to be highly active sites for ORR. All in all, the well distributed Co-N sites along with the porous structure are highly beneficial for the ORR performance.

The catalytic performance of the prepared materials towards the ORR was evaluated in 0.5 M oxygen saturated H_2SO_4 solutions by the rotating ring disk electrode (RRDE) method. At beginning, the catalysts pyrolyzed at various temperatures were assessed to optimize the catalysts' ORR activity. It was found that 900 °C is the optimized temperature

(Figure 24), and all the physical characterization results and the electroactivity investigation were based on the best optimized materials.

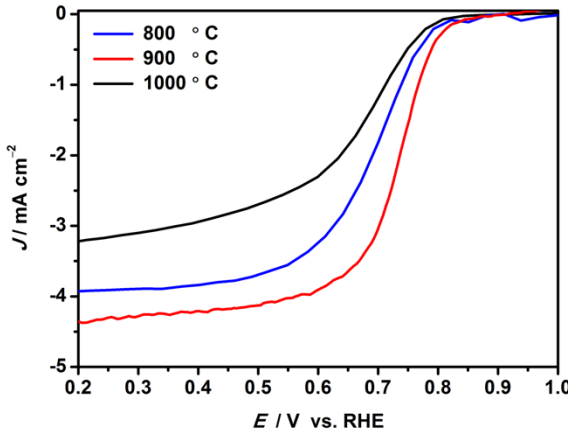

Figure 24. Polarization curves of the Co-N-GA catalysts pyrolyzed at 800 °C, 900 °C and 1000 °C. Test conditions: 0.5 M H_2SO_4 solution, 10 mV s^{-1} scan rate and 900 rpm rotate rate.

For comparison, pure GA, N-GA, Co-N-GS and commercial Pt/C (TKK, 28.2 wt.% Pt) were also investigated. As shown in Figure 25a, Co-N moieties modified graphene materials (Co-N-GA and Co-N-GS) exhibit much more positive onset potential (E_o) and half-wave potential ($E_{1/2}$) than that of N-GA and GA. This indicates the ability of Co-N moieties modified graphene materials to efficiently catalyze the ORR in acid medium. This result is corresponding to the previous report that a transition metal is necessary for nitrogen-doped carbons to be highly active catalysts, due to the formation Co-N coordination structures.[156] Moreover, the E_o and $E_{1/2}$ of Co-N-GA (E_o = 0.88 V, $E_{1/2}$ = 0.73 V) are more positive than that of Co-N-GS (E_o = 0.84 V, $E_{1/2}$ = 0.68 V), which is approaching the commercial Pt/C catalyst (E_o= 1.0 V, $E_{1/2}$ = 0.86 V, Table 7). Additionally, Co-N-GA also shows a slightly higher diffusion limiting current density than that of Co-N-GS at 0.4 V (Figure 25a). The peroxide yield and electron transfer number (n) of the

prepared catalysts and Pt/C were further studied using the RRDE analysis. The measured H_2O_2 yield on the Co-N-GA electrodes is 7%−13% from 0.2 V−0.7V, which is slightly superior to that of Co-N-GS (10%−15%, Figure 25b, Table 7). On the basis of the ring and disk currents, the *n* values for Co-N-GA were 3.75−3.85 over the potential range from 0.20−0.70 V, similar to that of Co-N-GS (3.71−3.80, Figure 25b, Table 7), approaching that of Pt/C catalysts, indicating that both of the two Co-N modified samples proceed mainly via a four-electron mechanism. In view of the above analysis, the enhanced ORR activity of Co-N-GA could mainly originate from its unique hierarchically porous structure and more active Co-N moieties. On one hand, the abundant hierarchical pores could sharply enhance the surface area of the catalyst, which could provide sufficient active sites to participate in the ORR process. Meanwhile, the hierarchical pores are favorable for mass transport and electrolyte accessibility. On the other hand, the potential Co-N moieties could function as more active sites for catalyst, which could further improve the ORR performance. All of these merits could contribute to the final excellent ORR performance.

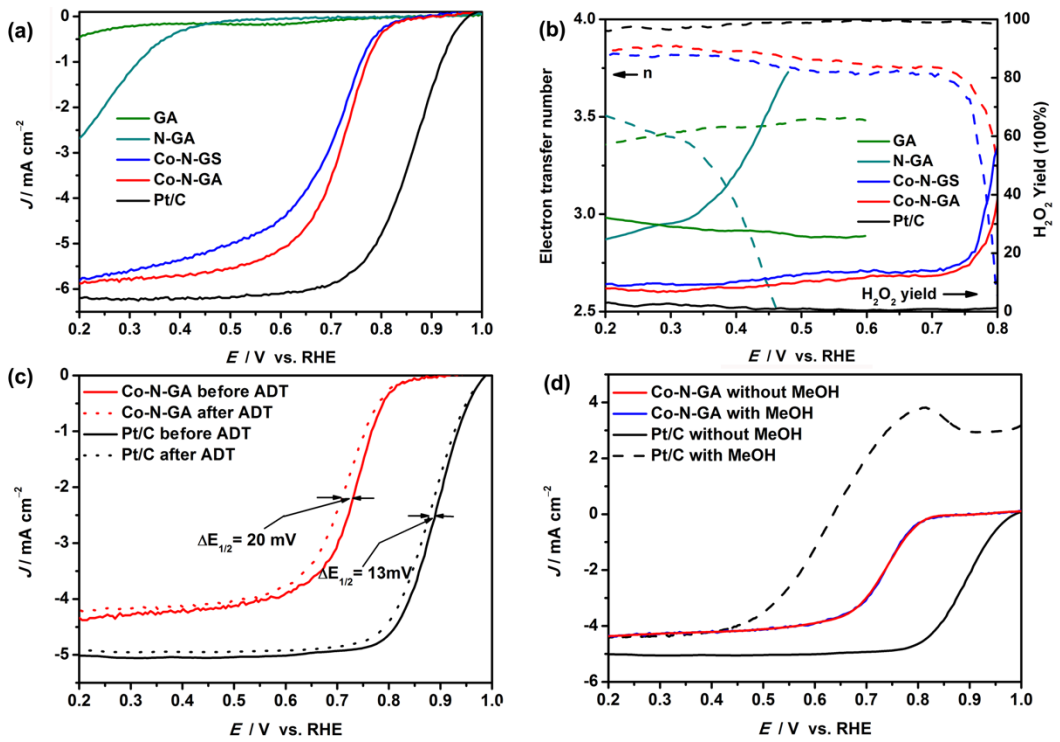

Figure 25. (a) RRDE polarization curves of the GA, N-GA, Co-N-GS, Co-N-GA and Pt/C in 0.5 M H_2SO_4 at a scan rate of 10 mV s^{-1} and 1600 rpm; (b) electron-transfer number and H_2O_2 yield of the catalysts; (c) ORR polarization plots of Co-N-GA and Pt/C before and after 5000 potential cycles in N_2 saturated 0.5 M H_2SO_4 at a scan rate of 10 mV s^{-1} and 900 rpm. The potential was cycled between 0.6 and 1.0 V at a rate of 50 mV s^{-1}; (d) ORR polarization curves of Co-N-GA and Pt/C in O_2 saturated 0.5 M H_2SO_4 with or without methanol at a scan rate of 10 mV s^{-1} and 900 rpm.

Table 7. ORR electrocatalytic performance of the samples[a].

Samples	Medium	E_o	$E_{1/2}$	$\Delta E_{1/2}$	n	Maximum
		V	V	mV		H_2O_2 (%)
N-GA	Acid	–	–	–	–	–
	Alkaline	0.85	0.68	190		38

					3.2~3.6	
Co-N-GS	Acid	0.84	0.68	180	3.71~3.80	15
	Alkaline	0.92	0.81	60	3.94~3.96	2.43
Co-N-GA	Acid	0.88	0.73	130	3.75~3.85	13
	Alkaline	0.99	0.85	20	3.94~3.97	2.26

[a]Acid: 0.5 M H_2SO_4; Alkaline: 0.1 M KOH; E_o: onset potential; $E_{1/2}$: half-wave potential; $\Delta E_{1/2}$: half-wave potential difference between Pt/C and prepared samples; n: electron transfer numbers; "–": The activity is too low to be detected.

Apart from the ORR activity, stability is another important aspect of fuel cell catalysts that needs considering. The durability of the Co-N-GA catalyst was assessed using an ADT by potential cycling between 0.6 V and 1.0 V at 50 mV s^{-1} under N_2 saturated solution. After 5000 continuous cycles, a small negative shift of $E_{1/2}$ (ca. 21 mv) was exhibited for Co-N-GA, which is similar to the ca. 15 mV negative shift observed for Pt/C (Figure 25c). This suggests comparable durability of Co-N-GA in acidic electrolyte, a feature rarely seen for NPMCs. The high electrochemical stability of this Co-N-GA catalyst could be ascribed to the high degree of graphitization of carbon support and the lower H_2O_2 production.[179, 180] Furthermore, the methanol crossover effect of Co-N-GA and Pt/C was investigated by measuring the RDE polarization curves for the ORR in 0.5 M methanol-containing acid solution. As shown in Figure 20d, the Co-N-GA catalyst shows almost identical ORR polarization curves in the acid electrolyte with and without methanol, indicating excellent methanol tolerance. In contrast, a drastic decrease in the current density

was observed for the Pt/C, indicating oxidation of methanol due to high anodic activity of Pt/C.

In addition, the ORR performance of abovementioned materials in alkaline electrolyte was also investigated. As shown in Figure 26, the electrocatalytic performance in alkaline follows the same trend with observations in acid media. The cobalt contained catalysts (Co-N-GS and Co-N-GA) show higher E_o and $E_{1/2}$ than that of N-GA catalyst (Table 7). Still, the Co-N-GA catalyst with high surface area and hierarchically porous skeleton exhibits the highest ORR catalytic activity in alkaline media with $E_{1/2}$ = 0.85 V *vs* RHE, which is very close to that of Pt/C catalyst ($E_{1/2}$ = 0.87 V). What's more, the higher *n* value (n> 3.94) and low H_2O_2 yield (< 3%) for Co-N-GS and Co-N-GA further indicates their promising activity in alkaline medium. Through above analysis, it is obvious that the activity gap between Co-N-GA and Pt/C catalyst, expressed as a difference of half-wave potential ($\Delta E_{1/2}$) in RRDE testing, in acid medium is much greater than that in alkaline(130 *vs* 20 mV, Table 7). This is probably because: 1) most of the incorporated nitrogen groups (not involved in metal coordination) which contribute to ORR activity in alkaline medium are prone to protonate in acid electrolyte thus results in decreased activity for ORR;[181] 2) only the acid-resistant Co-N moieties play a vital role in catalyzing ORR in acid medium.[182] Hence, in ordered to diminish the influence of protonation it is necessary to increase the number of Co-N active sites per unit volume to sustain a high ORR activity in acid medium. Ascribed to the unique hierarchically porous architecture of Co-N-GA, many acid-resistant Co-N sites that secluded inside the aggregated graphene sheets could be exposed at the top layer of Co-N-GA catalyst and the reactant could also be transferred more efficiently, all of these facts make the Co-N-GA materials as promising ORR catalyst in acid medium.

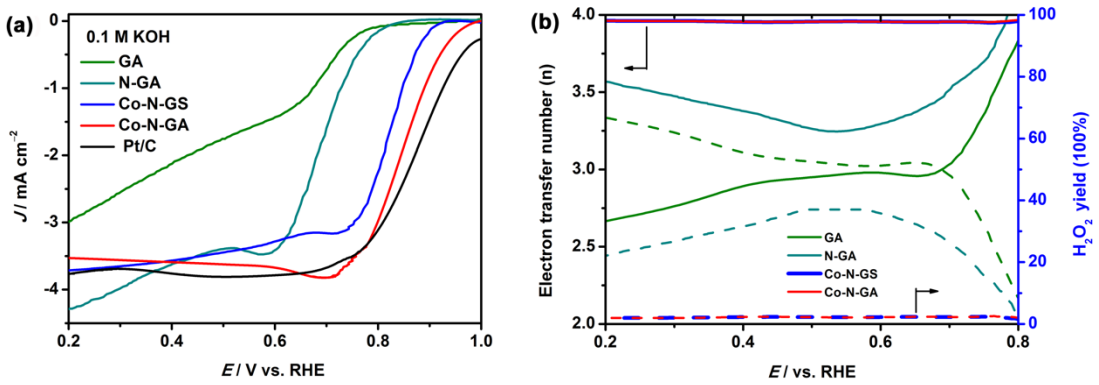

Figure 26. (a) RRDE polarization curves of the GA, N-GA, Co-N-GS, Co-N-GA and Pt/C in 0.1 M KOH at a scan rate of 10 mV s^{-1} and 900 rpm; (b) electron-transfer number and H_2O_2 yield of the catalysts.

4.4 Conclusions

In summary, a Co-N decorated graphene aerogel has been successfully fabricated via a simple approach. The introduction of PANI, which acts as a hydrogel forming agent and nitrogen precursor, can efficiently prevent graphene sheets restacking and promote nitrogen doping. The resulting Co-N-GA framework possesses a high BET surface area and hierarchically porous skeleton as well as homogeneous distribution of potential Co-N active sites, which can not only expose more active site to electrochemical interface but also facilitate the mass transport to improve the ORR performance. Based on these characteristics, the resultant Co-N-GA exhibits high ORR activity ($E_{1/2}$ = 0.73 V), high electron transfer selectivity (n >3.75), excellent electrochemical durability and high methanol tolerance in acidic solution. The outstanding electrochemical performance makes the Co-N-GA a promising NPC for PEM fuel cell.

Section 5: Is the rapid initial performance loss of Fe/N/C non precious metal catalysts due to micropore flooding?

This chapter is reprinted from the following two publications, with permission from both journals.

JY. Choi, L. Yang, T. Kishimoto, X. Fu, S. Ye, Z. Chen, and D. Banham, Is the rapid initial performance loss of Fe/N/C non-precious metal catalysts due to micropore flooding?, Energy & Environmental Science, 2016, In press (DOI: 10.1039/C6EE03005J)

X. Fu, P. Zamani, J. Y. Choi, F. Hassan, G. Jiang, D. C. Higgins, Y. Zhang and Z. Chen, In situ polymer graphenization ingrained with nanoporosity in a nitrogenous electrocatalyst boosting the performance of polymer-electrolyte-membrane fuel cells, Advanced Materials, 2016, In press (DOI: 10.1002/adma.201604456)

5.1 Introduction

Over the past 5 years, proton exchange membrane fuel cells (PEMFCs) have begun to make real and measured progress towards commercial viability in markets such as backup power and materials handling. While these markets are certainly growing, and represent an excellent commercial opportunity for PEMFCs, ultimately the biggest market will be automotive. In 2015, Toyota and Hyundai both launched small scale PEMFC automotive fleets, with plans from many other automotive OEMs to do the same by 2020. This exciting result is due to the great achievements made over the past decades on reducing cost and improving the durability of PEMFCs.

However, despite the unquestionably impressive advances in PEMFC technology, the wide-spread adoption of PEMFCs for automotive applications will require further reductions in cost. In particular, a reduction in the total platinum group metals (PGMs) currently used to catalyze the hydrogen oxidation reaction (HOR) at the anode, and the oxygen reduction reaction (ORR) at the cathode, is required for PEMFCs to become cost competitive in the long term. The largest opportunity for reducing PGM loading is currently at the cathode, which typically contains ~ 80 % of the total PGM loading in the membrane electrode assembly (MEA) due to the sluggish kinetics of this reaction (10^5 slower than the HOR[183]).

One approach to reducing PGM loadings has been to develop non-precious metal catalysts (NPMCs). Of the NPMCs that have been developed, the most promising to date appear to be the M/N/C (M=Fe, Co, Mn) class[19, 93, 184-186]. In fact, the significant improvement in activity/performance of these catalysts that have been demonstrated in recent years has advanced these catalysts to a stage at which they can start to be considered as viable alternatives to Pt/C for certain PEMFC applications. While this is very encouraging, it has been recognized that the durability/stability of these catalysts must be further improved before they can truly compete under the harsh operating conditions of PEMFCs[187].

Certainly over the past several decades, the primary research focus in the NPMC field has been to improve performance/activity. Thus, it is no surprise that the research community mostly agrees upon the main active sites/design parameters required to achieve high performance as a result of many detailed studies aimed at characterizing and understanding the active sites in these catalysts[188-192]. However, the same cannot be said for

stability/durability limitations, which have only recently become a higher priority within the research community. To aid in this discussion, our group recently wrote a review paper in which we clearly defined and separated 'durability' and 'stability' in the context of PEFMC testing[187]. Durability was defined as performance loss following voltage cycling, and stability was defined as performance loss following constant voltage/constant current experiments. Certainly the majority of work in the literature has focused on stability, with only limited studies on voltage cycling durability[15, 31, 94, 193, 194]. This is likely due to the fact that only recently have NPMCs demonstrated sufficient performance to warrant durability/voltage cycling experiments. However, the stability of the catalyst is inevitably tested during routine performance measurements, and thus significantly more data has been obtained for this mode of degradation. Using the extensive data set available in the literature, it quickly becomes clear that there are two distinct time-frames involved in stability loss during MEA testing: 1) a rapid initial loss in the first few hours, and 2) a more gradual but persistent loss with continued testing[187]. Due to the rapid nature and magnitude of the initial performance loss, understanding and mitigating this problem is of critical importance.

A survey of the literature[187] shows that stability losses of NPMCs have largely be attributed to one of three mechanisms: 1) leaching of the nonprecious metal catalyst[63, 195-198], 2) attack by H_2O_2[11, 199] (and/or free radicals)[47], 3) protonation of the active site[200], or protonation of a N species neighbouring the active site, followed by anion adsorption[201]. Evidence for each one of these mechanisms has been reported, and it is possible (likely) that all three mechanisms impact the stability of NPMCs. Recently, a new mechanism concerning micropore flooding has been suggested as an explanation for the rapid initial performance loss[202-205].

Extensive work by Dodelet's group over the past decade has provided convincing evidence that the most active catalytic sites are hosted within micropores[206-208]. Thus, it is reasonable to conclude that flooding of micropores would negatively impact performance by causing additional mass transport losses to the active sites hosted within these pores. Recent work by Dodelet's group has shown that this mechanism of instability does appear to explain several previously observed results including 1) the stability of NPMC has a negative correlation with the percentage of micropores, 2) the stability observed in rotating disk electrode (RDE) experiments do not match that observed in an MEA, which the authors suggest is because the micropores in RDE tests should already be flooded[202]. While some preliminary tests have been performed to help support this hypothesis, further experiments are required to confirm the degree to which micropore flooding can explain the instability of most NPMCs. Fortunately, of all hypotheses for NPMC instability that have been proposed, flooding of micropores should be relatively straight forward to test experimentally.

Before proposing how to experimentally test this hypothesis, it is important to first clarify the difference between standard catalyst layer flooding and the mechanism of seemingly irreversible micropore flooding that has been proposed[203, 204]. Catalyst layer flooding is a well-known phenomenon that can occur at high relative humidities/current densities and leads to performance loss due to mass transport limitations. In fact, preventing catalyst layer flooding is a strong consideration when designing any MEA, and many mitigation strategies have been developed at all levels (catalyst layer, MEA, stack, and system) of PEMFC products. This mode of flooding is not specific to micropores within the catalyst, but extends to the entire hierarchy of pore sizes within the catalyst layer and GDL. However, a key aspect of this type of cathode catalyst layer (CCL) flooding is that it is

reversible, and performance can be recovered by changing the operating conditions. This is contrary to (and a key distinction from) the proposed mechanism of micropore flooding in NPMCs. In the most comprehensive study on this topic yet published[202], it is stated that the micropores in NPMCs initially are hydrophobic, and thus do not contain any water. During operation, carbon oxidation is said to lead to the micropores becoming hydrophilic, at which point they fill with water. Since this surface oxidation cannot be reversed by simply returning to dry conditions, the performance loss is irreversible (unlike conventional catalyst layer flooding). It is also stated that this surface oxidation leads not only to a mass transport loss (from micropore flooding) but also to a kinetic loss due to either oxidation of active sites or a loss in electronic conductivity through the catalyst[202]. Several studies have provided indirect support for this mechanism[203, 204], or worked to eliminate competing hypotheses[202]. However, to date there has been no clear study to directly measure the degree of micropore flooding and its possible effect on the stability of NPMCs.

Thus, the goal of the present study was to devise a series of experiments to directly quantify both the degree of micropore flooding that may occur, and the resulting impact on NPMC stability. This was achieved through comparing air/O_2 polarization curves at various relative humidities, as well as evaluating changes in the double layer capacitance (obtained by cyclic voltammetry) before and after stability testing. In devising the experiments in this study, two separate cases of micropore flooding were considered: 1) The micropores are initially not wetted, but fill over time resulting in mass transport limitations, 2) Micropores are initially partially wetted, but then completely fill when current is generated in the catalyst layer. There is of course a third case where the micropores could be fully filled at beginning of life (BOL). However, this possibility clearly could not lead to additional

transport losses during operation of the fuel cell as no additional flooding of the micropores would be possible. Since the goal of the present work is to develop a method for studying micropore flooding, and to utilize this method to study one particular NPMC, the case of fully filled micropores at BOL has been omitted since no additional transport losses from micropore flooding would be expected.

5.2 Experimental

5.2.1 Background information on the catalyst

Among the NPMCs developed up to date, complexes of transition metals (M = Fe, Co, etc.), nitrogen and carbon precursors (M-N-C) which undergo high temperature pyrolysis, represent the most promising alternatives to potentially replace Pt-based catalysts in PEMFCs.[186, 209-218] Dodelet's et al., pioneers of this research area, utilized filler materials and ball-milling approach to improving the ORR performance of the Fe-N-C catalysts.[93, 219] Also, Zelenay's research team in Los Alamos National Lab developed a new class of heteroatom polymer derived catalysts with improved activity and durability in half cell and fuel cell tests.[19, 220, 221] Despite these sign of progresses, the current state-of-the-art M-N-C catalysts still suffer from moderate activity and mass-transport properties and therefore they could not yet reach the fuel cell performance of Pt/C based catalysts.[222] In order to address these remaining challenges, it is necessary to maximize the electrochemical surface area of the catalyst, which is capable of hosting a large number of active sites towards ORR and hence boosting the activity of M-N-C catalysts.[223]

To further boost the activity, we developed an efficient strategy to synthesize Fe-N-C catalyst with *in-situ* formed 3-dimensional (3D) nanoporous graphene-like structures by

using dual nitrogen sources, e.g., phenanthroline (Phen) and polyaniline (PANI). This was achieved via introducing Phen into the pores of carbon support by ball-milling, which was then covered with PANI shell through polymerization of aniline, followed by several subsequent pyrolysis and acid leaching steps leading to the formation of *in-situ* 3D porous graphene-like morphologies with multiple types of pores. Here, Phen acts as a pore-forming agent that is capable of expanding the external PANI shell during the decomposition. Simultaneously, PANI shell converted to graphene-like structures through graphenization in the presence of iron species during pyrolysis processes.[224, 225] Therefore, the obtained graphene-like morphology can serve as high surface area carbon matrix hosting active sites to catalyze ORR.[19] Such utilization of dual nitrogen sources leads to unique graphene-based nitrogenous electrocatalyst with nanoporosity, which significantly boost the fuel cell performance. Among the NPMCs developed in our group, Fe-N-C-Phen-PANI dual nitrogen catalyst has been selected due to its high activity and high microporosity to study the micropore flooding behavior.

5.2.2 Catalyst Synthesis

For the synthesis of Fe-N-C-Phen-PANI, modifications to a previously reported synthesis procedure from the literature by Wu et al[19] was taken. Typically, Phen (1,10-Phenanthroline, 500 mg), $Fe(Ac)_2$ (30 mg) and commercial carbon KJ600 (Ketjenblack EC 600J, 500 mg) were first dispersed in ethanol (100 mL) and the mixture was stirred at 80 °C until the aqueous solution was completely evaporated followed by a ball-milling process for 3 hours. The ball-milled powder mixture (400 mg) was dispersed in 0.5 M HCl and aniline (1.5 mL), $FeCl_3$ (5.0 g) and ammonium peroxidisulfate (2.5 g) were added consecutively. After 48 hours of vigorous stirring, the liquid from the suspension was removed via

evaporation overnight. The collected solid materials were then pyrolyzed at 900 °C in argon (Ar) for 1 hour. The resulting powders were subsequently leached in 0.5 M H_2SO_4 for 8 hours followed by thorough washing with deionized water. Finally, the catalysts were heat-treated again in Ar for 3 hours and then in NH_3 for 15 mins at the same temperature as the first heat treatment.

5.2.3 Physicochemical characterization

Porous structure and surface properties of the catalyst was analyzed by nitrogen adsorption technique using Micromeritics ASAP 2020 surface area and porosimetry system. From the obtained isotherm, Brunauer-Emmett-Teller (BET) surface area was calculated and the microporous surface area was obtained by the t-plot method. Transmission electron microscopy (TEM) was utilized to investigate the morphology of the catalyst, and scanning electron microscopy (SEM) was used to observe the cross-sectional image of the cathode catalyst layer in the MEA. The elemental composition of the catalyst was determined by energy dispersive X-ray (EDX) analysis.

5.2.4 Half-cell electrochemical test

All the ORR half-cell measurements were conducted using Pine Electrochemical Station (Model AFCBP-1) with a conventional three-electrode method. Ag/AgCl (filled with 3M KCl) and graphitic electrodes were used as reference and counter electrodes, respectively. All potentials were afterward converted to reversible hydrogen electrode (RHE) scale for the ease of comparison.

5.2.5 MEA Preparation

To prepare catalyst ink, 40 mg of Fe-N-C-Phen-PANI catalyst was mixed with deionized water, isopropanol and 5% Nafion dispersion to achieve the ionomer to catalyst (I/C) ratio of 0.54 corresponding to 35 wt.% Nafion. The homogenized catalyst ink was deposited onto Nafion 211 membrane in 5 cm^2 square area and the catalyst loading was determined by comparing the weight before and after the catalyst layer coating. The catalyst coated membrane along with the gas diffusion layer (SGL 29 BC) on the cathode side and a gas diffusion electrode with 0.2 mg cm^{-2} Pt loading as anode were pressed together at 130 °C for 5 minutes, using a pressure of 1000 psi.

5.2.6 MEA Testing Protocol

The MEA was evaluated in a single cell using a Scribner 850e fuel cell test station. A series of experiments was performed in a sequence of conditions as illustrated in Fig. 27, namely 60% RH, 100% RH, a stability test, 100% RH, 60% RH, an extreme dry-out protocol and 60% RH, consecutively. For both the 60% and 100% RH test cases, cyclic voltammetry (CV) was conducted before and after taking polarization in air and oxygen, in an order of CV, air polarization, oxygen polarization and CV in the voltage range from 0.1 to 0.8 V at 20 mV/s scan rate with N_2 purge in cathode and H_2 in anode. The cell temperature was kept at 80 °C while anode and cathode gases were humidified at different temperatures to obtain the desired relative humidity values. The stability test was performed at 100% RH in air by keeping the voltage at 0.4 V for 4 hours while monitoring the current. For the dry-out step, the cell temperature was maintained at 80 °C for 5 hours while nitrogen was purged in both anode and cathode at room temperature to remove moisture and residual reactants in the MEA. The flow rates for air, O_2, H_2 and N_2 were all kept at 200 sccm

throughout the experiments and the backpressure for both electrodes were maintained at 15 psig.

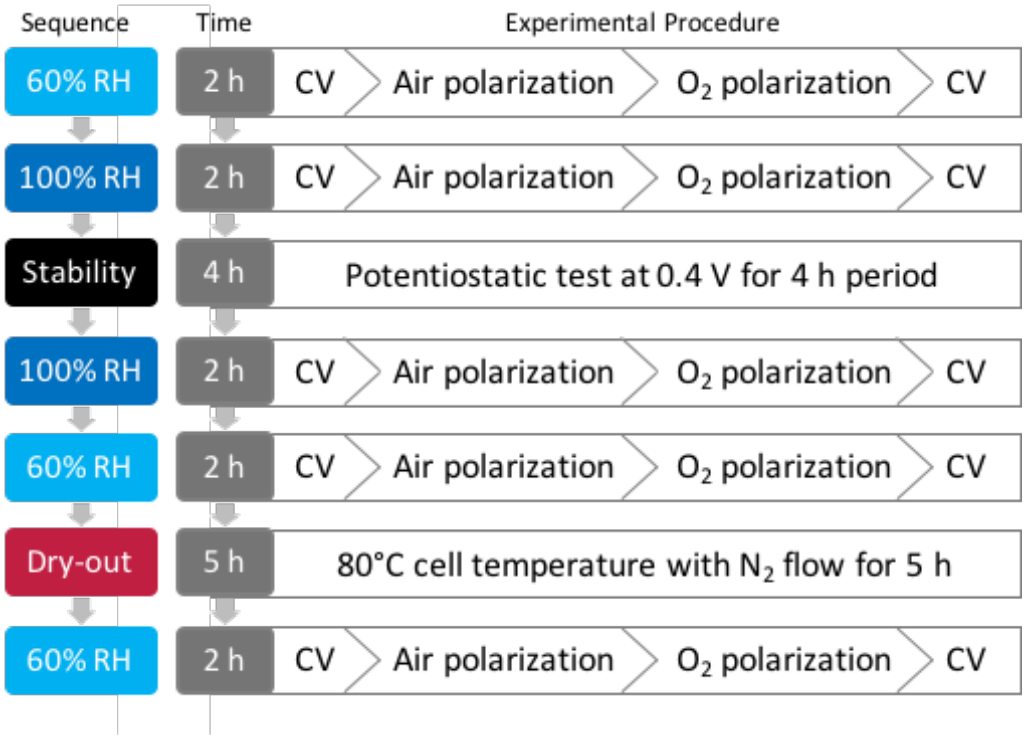

Figure. 27. Diagram outlining the experimental sequence for MEA test and the corresponding procedure for each step

5.3 Results and Discussion

5.3.1 Defining and Characterizing Case 1 and Case 2

Figure 28 highlights the differences in the water distribution in the catalyst for both Case 1 (micropores initially not wetted) and Case 2 (micropores only partially wetted). In both cases, it is assumed that the ionomer cannot penetrate into the micropores (d < 2 nm). This assumption is based on the fact that Nafion micelles range in size from 1-5 nm [226, 227], making it extremely challenging for Nafion to penetrate into pores < 2 nm in diameter. This

is supported by previous work in the literature which has also indicated that Nafion penetration into pores < 2 nm is extremely unlikely to occur[228-230]. Aside from this point, there is a key difference between these two cases that must be highlighted.

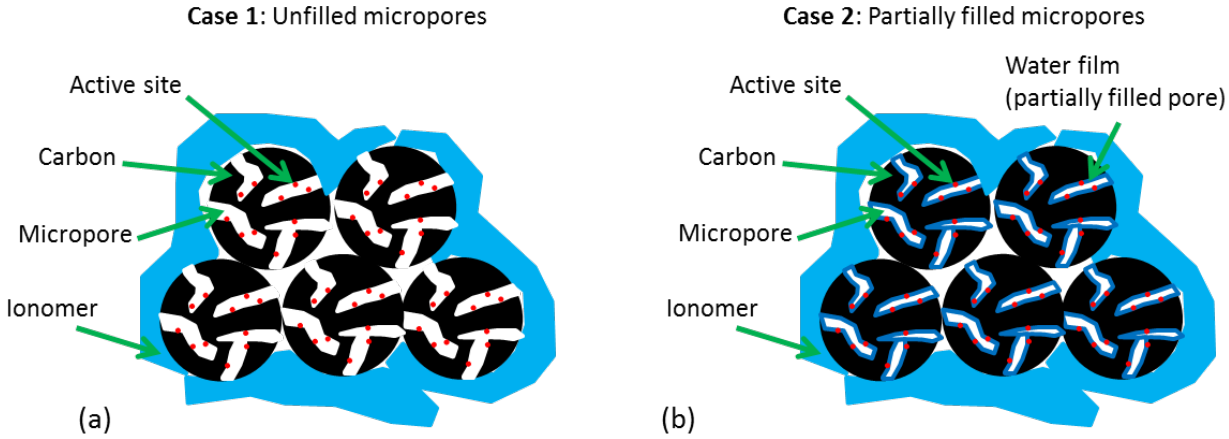

Figure. 28 Schematic representation of the two possible cases: (a) Case 1: Micropores are unfilled at BOL, (b) Case 2: Micropores are partially filled at BOL.

In Case 1, it is assumed that the pores are initially not wetted. This initially appears to be in line with the recent work published on the impact of micropore flooding on apparent stability, where it is stated that at beginning of life (BOL) the catalyst is hydrophobic and thus any water in the catalyst layer is not trapped in the micropores[202]. However, when bearing in mind that the majority of the active sites are believed to reside inside micropores[206-208], it quickly becomes apparent that this case is extremely unlikely. Without ionomer inside the micropores, the only possibility for proton transport to the active sites (required for the ORR to occur) would be through water. Without water already present in the pores, these sites would be inactive and the NPMC would show very poor BOL activity (low BOL activity is not generally observed). Additionally, no water would be formed in these pores during operation of the fuel cell as there would be no opportunity for the ORR to

occur. Furthermore, it is suggested that during operation of the fuel cell, the carbon becomes oxidized resulting in carbon functionalities that render the carbon surface hydrophilic and thus allow water to become trapped in the micropores. Since the electrochemical oxidation of carbon (Eq. 1) also requires the presence of water, any 'water-free' micropores would suffer no oxidation and thus should remain hydrophobic during operation of the fuel cell.

Equation 1: $C+2H_2O \rightarrow CO_2 + 4H^+ + 4e^-$

Thus, it quickly becomes apparent that not only is Case 1 quite unlikely, but even if it were to occur, no additional mass transport losses from micropore flooding would be expected as these pores would remain inactive.

Fortunately, cyclic voltammetry provides a simple and reliable approach for evaluating whether or not Case 1 does occur. Specifically, the double layer capacitance of the electrode is directly proportional to the electrochemically accessible surface area of the conductive catalyst particles[231] (Eq. 2).

Equation 2: $$C = \frac{\varepsilon \varepsilon_0 A}{d}$$

Where C is the capacitance, e is the dielectric constant of the medium, ε_0 is the permittivity of free space, A is the electrochemically accessible surface area and d is the thickness of the double layer. If we assume that the micropores are initially not wetted, and then gradually wet during operation of the fuel cell, the double layer charging current would be expected to increase as the electrochemical surface area gradually increases. In fact, since these catalysts are highly microporous, the growth in double layer charging current would be expected to be

quite large as 'flooding' of these pores occurred. This should be clearly observable by comparing in-situ cathode CVs obtained throughout the stability test.

The key difference with Case 2 is that a thin water film is already present in the pores. This significantly changes the argument, as now it is conceivable that additional water could be generated in these pores during operation of the fuel cell leading to flooding. Also, the surface of the pores could now be oxidized through Eq. 1 leading to an increase in hydrophilicity which in turn would further enhance micropore flooding. However, if a thin water film does indeed cover the surface of the micropores, this would render the walls hydrophilic, and due to the high energetics of micropore adsorption[232], the pores would be immediately filled at even moderate relative humidities. Nonetheless, overlooking this admittedly concerning problem with the hypothesis, Case 2 at least provides the possibility for flooding to occur in the micropores, and thus could lead to additional mass transport losses.

Characterizing Case 2 purely through observing changes in the double layer charging current is not as simple as in Case 1. If the micropores are partially/fully wetted by a thin water film at the beginning of the test, then little to no change in double layer charging current would be expected during operation of the fuel cell as little/no change in the electrochemical surface area would be observed. However, it should be emphasized again that *if* no change in double layer charging current is observed, this would suggest that the pores are in fact fully wetted by a thin water film at BOL, and it would thus be highly surprising if water did not immediately condense into these pores due to the highly favourable energetics of micropore filling[232]. If some unknown mechanism did somehow prevent this from occurring, another diagnostic tool would be required to evaluate whether

micropore flooding did indeed occur over the duration of the stability test. Fortunately, it is already known that comparing polarization curves obtained under air and O_2 can greatly aid in diagnosing mass transport limitations. Specifically, mass transport limitations will occur at much earlier current densities under air than under O_2 due to the ~ 5x lower oxygen concentration in air vs. pure O_2. Thus, if the active sites remain stable, but become less accessible due to flooding of the micropores, then polarization curves under air will show significantly more 'loss' than polarization curves under O_2. However, if the active sites are actually degrading with time, then a kinetic loss (parallel shift to lower voltages at every current density) would be observed when comparing subsequent O_2 polarization curves obtained at different times during the stability test.

Overall, by utilizing in-situ CVs and air/O_2 polarization curves, it should be straightforward to 1) differentiate between Case 1 and Case 2, and 2) determine whether either of these cases is actually responsible for the loss in performance that is observed during the stability testing. The protocol described in section 2.4 was specifically designed to answer these questions, and could be used as a diagnostic protocol by other researchers in this field to help address the impact of micropore flooding in their specific catalyst.

5.3.2 Characterization of NPMCs

Nitrogen sorption was used to evaluate the surface area and pore characteristics of the Fe-N-C catalyst used in this study as outlined in Table 8. The catalyst exhibits a BET surface area of 1244 m^2/g and a very high micropore area of 1149 m^2/g obtained by t-plot analysis, showing that over 92% of the total surface area of the catalyst is due to micropores. The large amount of micropores can be attributed to the presence of micropores within the carbon structures as well as inter-particle porosity. Since our aim is to examine the

correlation between the micropore flooding and the resulting impact on the stability, the high microporosity of this Fe-N-C catalyst makes it an excellent candidate to be used in this study.

Table 8. Surface and porosity analysis of the Fe-N-C catalyst

	Fe-N-C-Phen-PANI
BET Surface Area	1244 m^2/g
t-Plot Micropore Area	1149m^2/g
t-Plot External Surface Area	94 m^2/g

The TEM images (Fig. 29) illustrate the porous nature of the catalyst, showing an agglomerate of small carbon particles and porous graphite/graphene structures. Larger (10-20 nm) interparticle pores can also be observed (Fig. 29b), which could be beneficial for mass transport at high current densities when operating in an MEA[193].

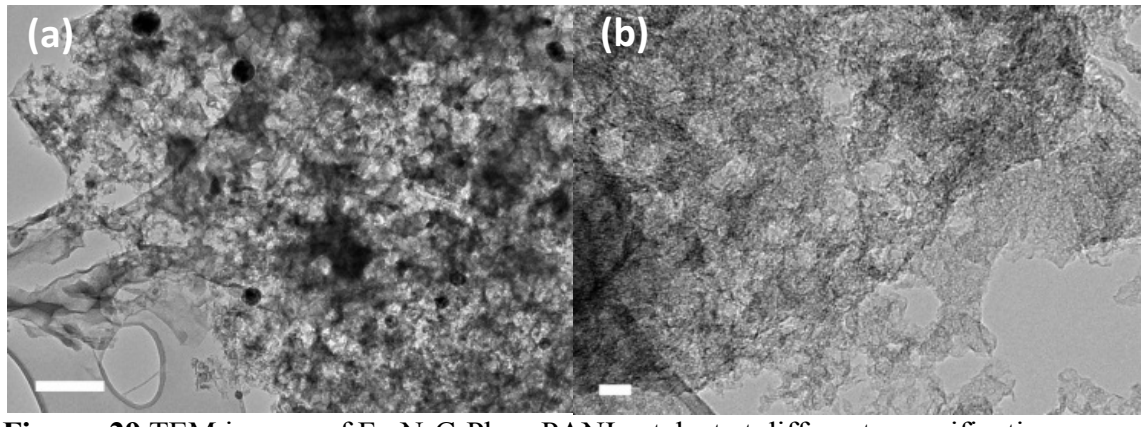

Figure. 29 TEM images of Fe-N-C-Phen-PANI catalyst at different magnifications

The elemental composition of the catalyst obtained by EDX is outlined in Table 9, and the catalyst loading in the MEA used in this study was measured to be 3.8 mg cm^{-2}. The cathode catalyst layer thickness measurement was done and the thickness of the layer turned out to be around 95 μm, which is in agreement with reported thicknesses for NPMC CCLs having a loading of ~ 0.4 mg cm^{-3} [184, 233].

Table 9: Elemental composition of the Fe-N-C-Phen-PANI catalyst obtained by EDX

	C (Wt. %)	N (Wt. %)	O (Wt. %)	S (Wt. %)	Fe (Wt. %)
Fe-N-C-Phen-PANI	89.41	4.45	4.31	0.12	1.71

The ORR activities of the as-fabricated Fe-N-C catalysts were first evaluated using rotating disk electrode (RDE) in 0.5 M H_2SO_4 electrolyte. The steady-state ORR polarization curves indicated the dual nitrogen sources derived Fe-N-C-Phen-PANI catalyst exhibits superior activity regarding half-wave potential ($E_{1/2}$ = 0.80V) compare with individual nitrogen source obtained catalyst Fe-N-C-PANI ($E_{1/2}$ = 0.79V) and Fe-N-C-Phen ($E_{1/2}$ = 0.67V) (**Figure 30a**). Additionally, rotating ring-disk electrode (RRDE) study was further performed to investigate the selectivity of these Fe-N-C catalysts towards the four-electron reduction of oxygen. Notably, the H_2O_2 yield of Fe-N-C-Phen-PANI catalyst remains below 2.5 % in potential ranges from 0.80 V to 0.20 V, which is lower than that of 3.0 %−5.0 % and 3.0 %−10.0 % for Fe-N-C-PANI and Fe-N-C-Phen catalysts, respectively (**Figure 30b**). The electron transfer number of Fe-N-C-Phen-PANI catalyst is above 3.95 (**Figure 30b**), which is superior to that of 3.91 and 3.82 for Fe-N-C-PANI and Fe-N-C-Phen catalysts, respectively, indicating a high selectivity towards four electron reaction. These electrochemical results clearly showed that dual nitrogen sources-derived catalyst exhibited

a better ORR activity than that of individual nitrogen source-derived catalysts, making it more ideal for the flooding investigation.

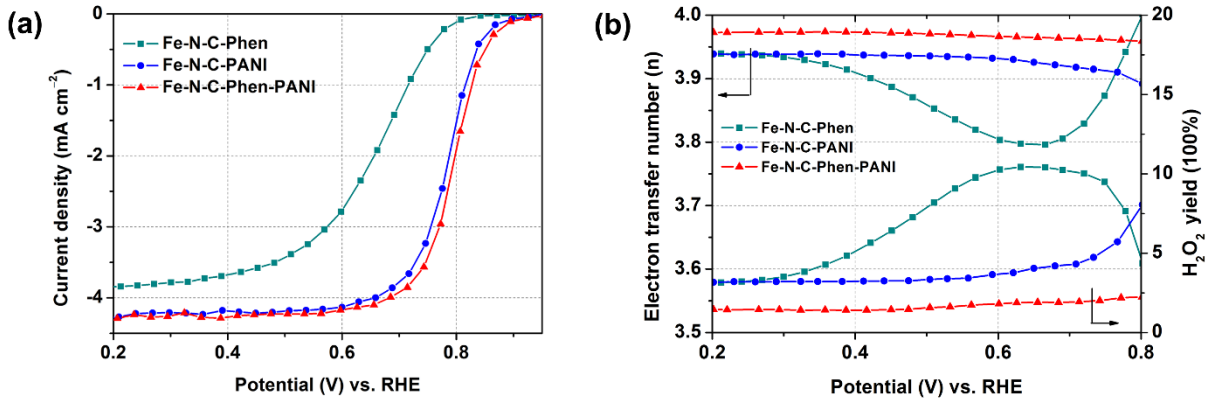

Figure. 30. (a) Steady-state ORR polarization plots of prepared catalysts; (b) Electron transfer number and H_2O_2 yield of prepared catalysts; All the RDE/RRDE test conditions: 0.5 M H_2SO_4 saturated with O_2, 900 RPM, 10 mV s^{-1}, catalyst loading of 0.6 mg cm^{-2}.

5.3.3 In-situ Evaluation

Relative humidities of 60 and 100% were evaluated to probe the impact of RH on micropore flooding. In each case, a CV was obtained before and after performing air and O_2 polarization curves. If micropore flooding occurred during the stability test, an increase in capacitance would be expected, as explained in section 3.1. However, as shown in Fig. 31, there is no clear change in the double layer charging current between the CVs obtained at 60 or 100% RH, before or after the polarization curves. This indicates that the micropores are already partially filled (Case 2) or fully filled, and that this process occurs immediately. Another possibility is that any micropores which are not initially filled do not flood during the polarization curves.

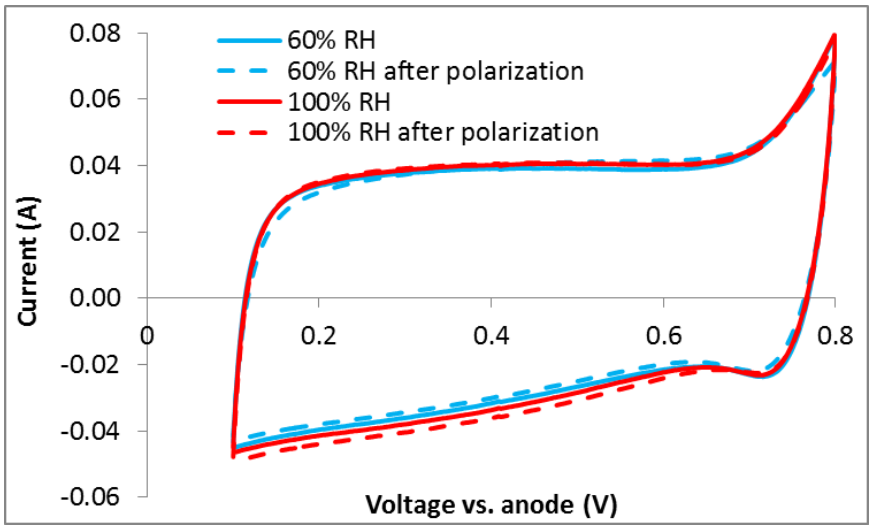

Figure. 31 CVs at BOL obtained at 60% RH and 100% RH

While the overlapping CVs in Fig. 31 clearly indicate that no additional wetting of the carbon surface occurs due to water being generated during polarization, it is not initially obvious what fraction of the total carbon surface is wetted (i.e. are the micropores fully wetted at this early stage of the analysis). Fortunately, an estimate can be made by examining the area specific capacitance (F/m^2) of the carbon catalyst obtained by the CVs.

Equation 3: $$\frac{F}{m^2} = \frac{\text{Capacitance (F)}}{Loading(g/cm^2{}_{MEA}) \cdot Area(cm^2{}_{MEA}) \cdot \text{Carbon area } (m^2/g)}$$

Clearly the area specific capacitance of a carbon material will be greatly impacted by the density of electroactive pseudocapacitive groups on its surface. However, it is known that for a wide range of carbons, this value falls between 0.05 F/m^2 (highly graphitic carbons) to 0.15 F/m^2 (highly functionalized carbons)[234]. As the carbon catalysts used in this work are relatively amorphous, and do not appear to have a high density of pseudocapacitive groups (Fig. 31), it would be reasonable to expect a specific capacitance value of ~ 0.1 F/m^2. This is in fact what is observed, with a specific capacitance of ~ 0.09 F/m^2 calculated from the CVs in Fig. 31. The only way to achieve this is if the majority of the surface area is fully

accessed/wetted at BOL, and contributing to the double layer. This is an important finding when keeping in mind that the catalysts are ~ 90% microporous (Table 8), and clearly indicates that even at BOL, the micropores are easily wetted. Thus, even at this early stage of the analysis, it seems likely that Case 1 is improbable, and if any micropore flooding is occurring, it must be starting with Case 2. However, due to the uncertainties in this estimate, no firm conclusions can be made at this stage of the analysis.

To evaluate whether traditional catalyst layer flooding was occurring in these CCLs at BOL, polarization curves were obtained under air and O_2 at both 60 and 100% RH (Fig. 32).

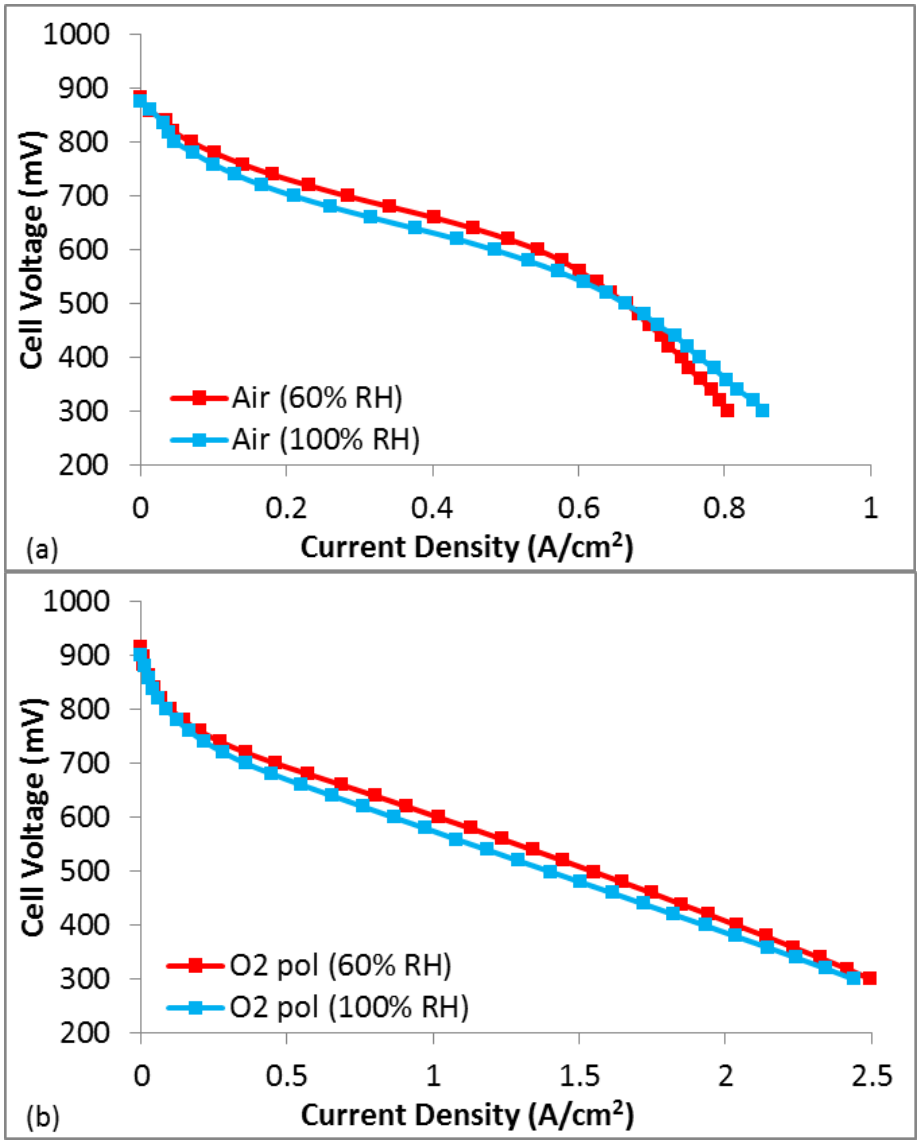

Figure. 32. Polarization curves at 60% and 100% RH under (a) air and (b) O_2.

The BOL high current density performance at 100% RH was not found to be significantly lower than at 60% RH, indicating that catalyst layer flooding was not occurring in this MEA. In fact, under air, the performance at 60% RH is slightly higher than that under 100% RH until a current density of ~0.6 A/cm^2, at which point the performance at 60% RH becomes mass transport limited. Clearly this mass transport limitation is not due to catalyst

layer flooding, which would actually be worse at 100% RH vs. 60% RH. Thus, it is likely that the mass transport limitations observed at 60% RH are due to drying of the CCL, leading to increased resistance to proton transport within the CCL. Unlike proton transport resistance in the membrane which are manifested as an Ohmic loss, proton transport limitations in the CCL lead to distributed potentials which are distinctly non-linear performance losses. When examining the O_2 polarization curve at 60 % RH (Fig. 32 (b)), the mass transport losses that were observed under air at 60% RH are absent, likely due to the significantly higher [O_2], which pushes the reaction boundary much closer to the membrane thus minimizing any proton transport losses in the CCL[235]. In this case with O_2, it is clear that the 60% RH data is slightly higher than the 100% RH data, and that this shift is mostly kinetic. As this small performance difference is clearly a kinetic loss, it is hypothesized that some of the active sites were degraded during the 60% RH testing, leading to lower performance when tested under 100% RH. In fact, it is well known that NPMC instability is most rapid during the first few hours of testing[93, 236, 237], so it would not be surprising if some activity was already lost following the several hours required for the diagnostics at 60% RH.

To evaluate stability, a potentiostatic experiment was performed by keeping the MEA at 0.4 V while monitoring the current that was generated (Fig. 33). As is clearly observed, the performance is significantly decreased over a 4 h period. This is not an uncommon finding, with many researchers showing significant performance loss within the first few hours of operation [93, 236, 237], which is often attributed to any of the previously mentioned mechanisms. However, the primary question being addressed in the present work is not about understanding exactly what mechanism is causing this loss, but rather, whether or not it is in fact due to micropore flooding. Fortunately, by previously obtaining the BOL

CVs, air polarization curves, and O_2 polarization curves, this question should be relatively easy to answer.

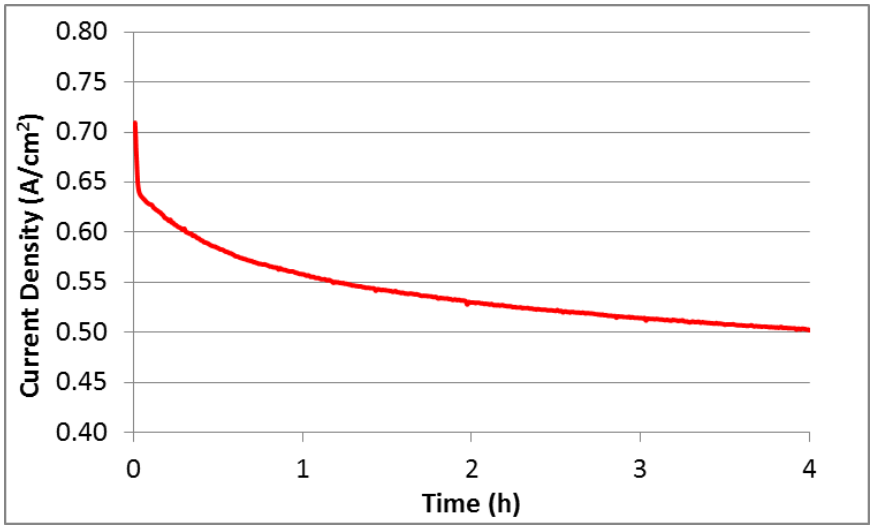

Figure. 33. Stability test for 4 hours under a constant voltage of 0.4 V at 100% RH. Cell temperature: 80°C; H_2/air flow rate: 200 sccm

Immediately following the stability test, a CV was obtained at 100% RH. In Fig. 34 (a), this CV is overlaid on top of the CV obtained at 100%RH prior to the stability test. It is clear that following the stability test, a small (~8%) increase in the double layer charging current is observed (a similar increase was observed at 60% RH). While no distinct pseudocapacitive peaks are observed, it is still possible that some surface oxidation occurred leading to either/or: 1) Pseudocapacitive groups forming over a range of potentials or 2) An increase in surface area due to loss of carbon. Alternatively (and possibly due to surface oxidation leading to increased hydrophilicity), it is possible that this increase is due to increased catalyst layer wetting. If this is true, then the question is whether this is simply CCL wetting in the traditional sense (i.e. wetting of a higher percentage of the total catalyst

layer and not just micropores), or whether this is evidence for the irreversible 'micropore flooding' mechanism purportedly responsible for the low stability of NPMCs.

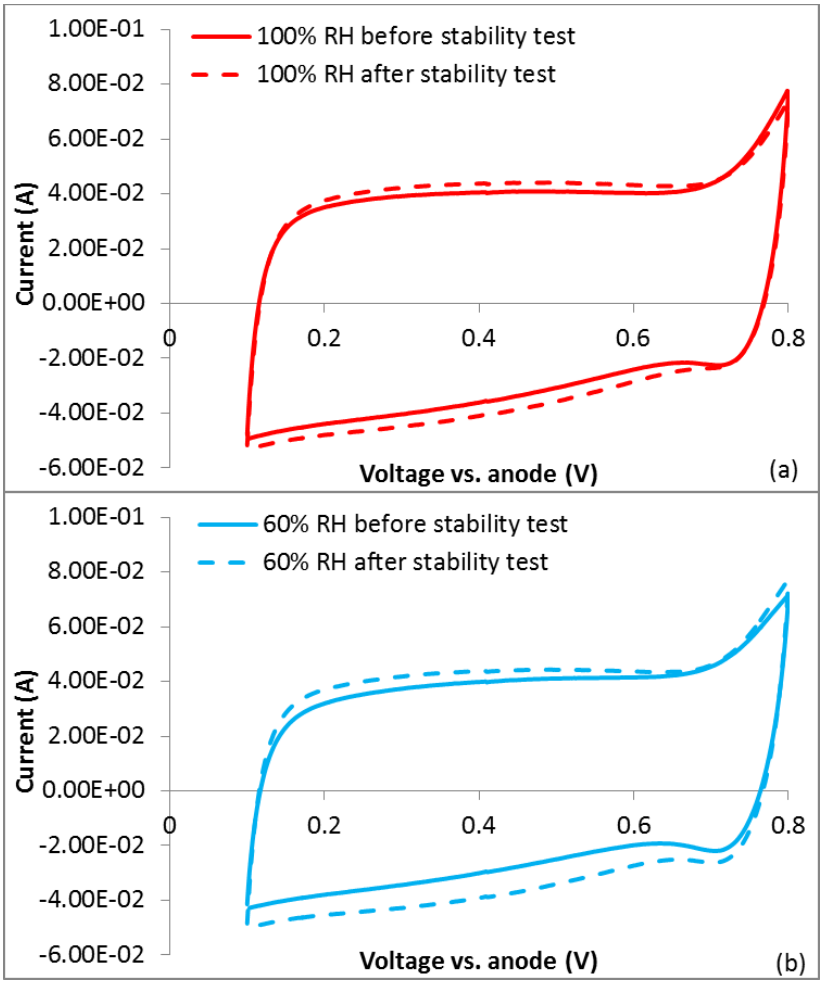

Figure. 34 CVs after the stability test obtained at (a) 100 %RH and (b) 60% RH

Based on the specific capacitance calculation performed previously, the majority of the micropores were already wetted at BOL. However, as discussed previously, the double layer charge can only be used to examine surface wetting, and it could still be possible that the partially filled micropores (Case 2, Section 3.1) have fully filled with water, and that this has led to the observed decrease in performance.

To examine this possibility, polarization curves under both air and O_2 were obtained (Fig 35). The goal of this experiment was to help understand whether actual kinetic losses (loss and/or deactivation of active sites) had occurred or if the losses could be explained due to reduced mass transport in the now flooded micropores. If the active sites were actually destroyed/de-activated during the stability test, a purely kinetic loss would be expected. However, if the loss in performance was due to micropore flooding, no change in the low current density performance would be expected, but significantly higher mass transport losses would be present even for the O_2 polarization curve, as O_2 would be forced to transport through the liquid water to the active sites as opposed to through the open micropores.

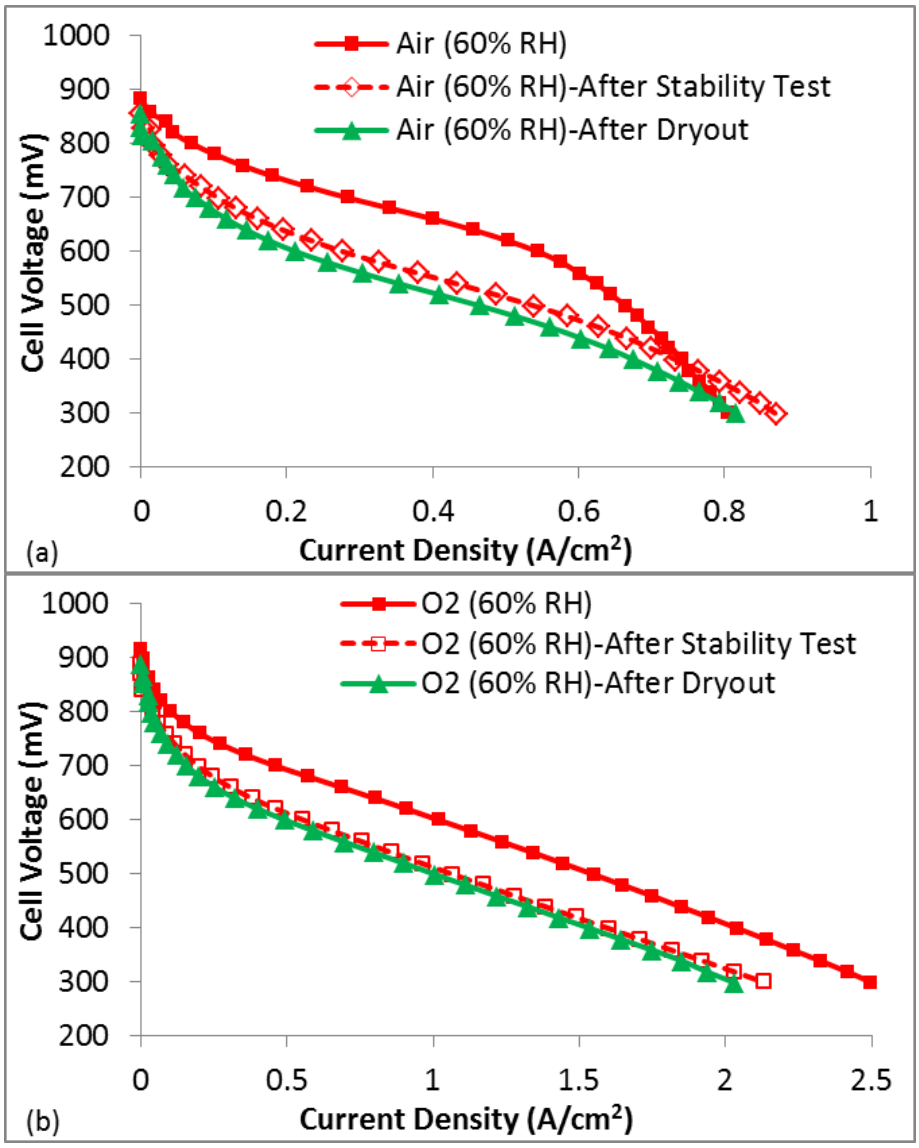

Figure. 35. Polarization curves (after performing the stability test) at 60% RH under (a) air and (b) O_2. The polarization curves following the extreme dry-out are shown in green triangles.

Looking first at the results under air at 60%RH, it is clear that significant decrease in performance has occurred following only 4 h at 0.4 V. The losses appear largely kinetic, but it is also clear that the polarization curve obtained after the stability test does not suffer as

severely from mass transport losses. In fact, at current densities >0.8 A/cm^2, the polarization curve obtained after the stability test actually shows higher performance than that obtained before the stability test. The reason for this is not entirely certain, but could be due to conditioning of the membrane/ionomer during the stability test. Importantly, this result does not show higher mass transport losses following the stability test, as would be expected if micropore flooding was indeed responsible for the low performance. This is further confirmed by analyzing the O_2 polarization curves, which show a kinetic loss following the stability test. This is a very different result than what would be expected if micropore flooding were the primary factor in reducing performance, and provides strong evidence that active site loss/de-activation has occurred. In fact, based on the change in the performance under O_2, the fraction of active site loss can be estimated using Equation 4:

Equation 4: $$\Delta\eta = \frac{RT}{\alpha F}\ln\left(\frac{\text{active sites at BOL}}{\text{active sites after stability test}}\right)$$

In Eq. 4, $\Delta\eta$ is the difference in voltage at a given current density in the performance plots shown in Fig. 35 (b). This equation relates the difference in performance to the total activity of the catalyst layer (assuming Butler Volmer kinetics). The results in Fig. 35 (b) show an approximately 60 mV loss in performance, which would suggest a 10x reduction in activity (loss of, or de-activation of, 90% of the active sites) of the catalyst layer following the stability test. This is a significant loss, and does not appear to be simply a mass transport limitation due to flooded micropores.

While the data shown in the manuscript provides convincing evidence that the instability of this NPMC cannot be attributed to micropore flooding, and additional

experiment was performed to rule out conventional catalyst layer flooding. Specifically, an extreme dry-out protocol was performed following the stability testing, which was designed to remove any water filling the macropores of the catalyst layer. This consisted of holding the cell temperature at 80°C while purging nitrogen gas in anode and cathode for 5-hour period. Despite this fairly aggressive dry-out, no performance gain was achieved. In fact, slightly lower performance was observed following the dry-out, which clearly appears to be a kinetic loss (Fig. 35). It is believed this is due to even further degradation of the active sites during the 5 h over which the dry-out occurred. While this does not itself prove that micropore flooding did not occur (for reasons clearly outlined in recent work[202]), when combined with the complete data set from this study, it does cast doubt on the micropore flooding mechanism for this particular catalyst.

Finally, it should be noted that this test protocol was designed specifically to look at the role of micropore flooding (assumed to occur steadily within the first few hours of operation). Longer term testing would almost certainly reveal additional performance loss mechanisms (e.g. oxidation from H_2O_2), but as this was not the focus of the present work, the stability test was relatively short (4h).

5.3.3 Most likely cause(s) of rapid degradation

The goal of this work was to determine whether or not micropore flooding[202-205] could be responsible for the observed instability of NPMCs (particularly within the first several hours), and in that respect, it was successful with the 'micropore flooding' mechanism found to be very unlikely. However, this only leads to a more urgent question: If not micropore flooding, then what mechanism is responsible for the significant loss in performance that was observed? While answering this question lies beyond the scope of this

work, these findings would nevertheless feel incomplete without some commentary on likely mechanisms for instability.

As mentioned in the introduction, several of the co-authors have already written a comprehensive review on the stability and durability of NPMCs[187]. In that work, three main mechanisms for NPMC instability were identified. Since this time, the 'micropore flooding' mechanism has emerged, giving us four possible degradation mechanisms: 1) demetalation of the NPMC[63, 195-198], 2) attack by H_2O_2[11, 199] (and/or free radicals)[47], 3) protonation of the active site[200], or protonation of a N species neighbouring the active site, followed by anion adsorption[201], 4) micropore flooding[202-205]. However, it should be stated that, based on the findings from the present work, it appears likely that the first three mechanisms remain the most likely, with 'micropore flooding' having a minor contribution, if at all, to NPMC stability.

In the present work, the observed kinetic losses were attributed to '***loss'*** and/or '***deactivation'*** of active sites. Clearly these terms will have different meanings, which must now be clarified. ***Loss*** of an active site would most likely come about from ***irreversible*** oxidation of the active site. This is the type of degradation predicted by Mechanisms 1 and 2. ***Deactivation*** is associated with a change in the chemical nature of (including change in oxidation state of pseudocapacitive groups), or inaccessibility of reactants to, the active site. In either case, it is more likely to be ***reversible***. With this in mind, Mechanisms 1 and 2 would lead to 'loss', whereas Mechanism 3 and 4 would lead to 'deactivation'.

While it is very difficult to rule out Mechanism 3, it is the authors' opinion that active site loss as opposed to deactivation, is the most likely reason for NPMC instability. This is based on our own observations that these performance losses are irreversible. This

leaves either demetalation (Mechanism 1) or attack by H_2O_2/radicals (Mechanism 2) as the most likely causes. Recently, operando spectroscopy has been used to directly characterize demetalation during operation of NPMC-based MEAs[196, 198]. Through this important work, it was determined that while demetalation will occur, it is not responsible for the rapid performance loss that is typically observed with the first several hours. This is in agreement with previous work by Zelenay et al. who also reached the conclusion that demetalation will occur, but that it is not strongly correlated with performance loss[238].

This leaves oxidation of the carbon/active sites as the most likely cause. At potentials relevant for most stability tests (< 0.6 V)[31, 47, 111, 238, 239], it is unlikely that carbon corrosion is occurring electrochemically at a significant rate. Thus, attack of the carbon/active sites by H_2O_2/radicals currently is our leading hypothesis for the rapid performance decay observed in most NPMCs. In fact, direct evidence for this mechanism has previously been demonstrated[199, 239].

Unfortunately, this mechanism is far more difficult to characterize through conventional electrochemical methods than the micropore flooding mechanism studied in the present manuscript. While growth the carbon double layer charge under N_2 would occur with oxidation of the carbon surface, it is not clear how oxidation of active sites would impact the CV response, nor is it clear what the relationship would be between growth of the carbon double layer and observed performance loss. It is our opinion that characterizing, understanding, and overcoming this problem should be a large focus in the coming years within the NPMC community.

5.4 Conclusions

A systematic study was designed and performed to investigate the emerging hypothesis that the largest contribution to the instability of NPMCs is from the flooding of micropores. This was achieved by comparing the degree of micropore flooding in-situ with the observed instability of a NPMC-based MEA. As a means to evaluate the degree of micropore flooding, the changes in the double layer capacitance following cyclic voltammetry were monitored throughout the test protocol and compared to the changes in air/O_2 polarization curves at various conditions. The CVs and specific capacitance calculation clearly show that the majority of the micropores are wetted at BOL, and although some degree of additional catalyst layer wetting occurs during the stability test, such a small increase cannot explain the significant performance loss that is observed. In addition, the loss in performance appears primarily kinetic and the mass transport loss due to flooded micropores appears relatively insignificant. Overall, the findings in the present study do not support micropore flooding as being the major contributor to the stability loss, at least for the family of NPMCs evaluated in this work. Importantly, the protocol outlined here can be utilized by other researchers in the NPMC community as a simple but highly effective method to diagnose micropore flooding in NPMCs and its impact on the stability of their catalysts. This should help guide researchers as they strive to develop more stable NPMCs which will be required for commercialization.

Section 6: Conclusions and Future Work

6.1 Summary and conclusions

To develop non-precious metal catalysts with high ORR activity and stability that can deliver sufficient MEA performance and durability in the PEM fuel cell applications, various experiments were carried out to synthesize three different NPMCs for ORR and investigate the performance and behaviors in the fuel cell applications. The first two studies focused on developing active NPMCs with uniformly distributed Fe-Nx active sites on carbon support and Co-N decorated porous graphene aerogel catalyst which have been successfully carried out along with in depth analysis on the nitrogen groups related to their performances. The last study was done to investigate the correlation between the micropore flooding and rapid initial performance loss that researchers in NPMC communities often report for the family of Fe/N/C catalysts.

In Section 3, non-precious metal oxygen reduction reaction (ORR) catalysts were prepared by heat treating a carbon supported iron-TCNB complex at temperatures ranging from 700 to 1000 ºC. By employing these small precusursor molecules, it is expected that more uniform and complete coverage of the carbon support material can be obtained, and by using the *in situ* formation and polymerization of FePc, effective iron-center segregation can be achieved. The highest ORR activity in 0.1 M $HClO_4$ was observed for Fe-TCNB/C-1000 catalyst, demonstrating an onset potential of ca. 0.88 V *vs.* RHE and a 4 electron reaction selectivity greater than 98 % at all electrode potentials investigated, a value comparable with some of the best non-precious metal catalysts reported to date. Based on high-resolution

TEM imaging, the observed ORR likely arises from a thin (< 10 nm) surface layer formed during the heat treatment of the surface coordinated iron-TCNB complex. Additionally, at higher pyrolysis temperatures, decreased nitrogen contents were observed along with an increase in the relative concentration of graphitic nitrogen species that likely play an important role in the catalytically active site structure(s). The results suggest that this type of catalyst has some potential to be used as a non-precious PEM fuel cell catalyst, however, the activity should be further improved and the stability issue related to the corrosion of the carbon black support should eventually be avoided to be practical for any applications.

In order to utilize many intriguing characteristics of graphene including high corrosion resistance to enhance the ORR activity and stability, a method to synthesize a Co-N decorated graphene aerogel based catalyst was developed in Section 4. The introduction of PANI, which acts as a hydrogel forming agent and nitrogen precursor, can efficiently prevent graphene sheets restacking and promote nitrogen doping. The resulting Co-N-GA framework possesses a high BET surface area and hierarchically porous skeleton as well as homogeneous distribution of potential Co-N active sites, which can not only expose more active site to electrochemical interface but also facilitate the mass transport to improve the ORR performance. Based on these characteristics, the resultant Co-N-GA exhibits high ORR activity ($E_{1/2}$ = 0.73 V), high electron transfer selectivity (n >3.75), excellent electrochemical durability in acidic medium. The outstanding electrochemical performance makes the Co-N-GA a promising NPC for PEM fuel cell.

In Section 5, to further enhance the activity of NPMC catalyst by greatly improving the surface area and microporosity of the catalyst, Fe-N-C-Phen-PANI dual nitrogen catalyst was developed and chosen for a systematic study in MEA to investigate micropore flooding

in-situ before and after stability testing. Recently, it has been proposed in the non-precious catalyst community that the largest contribution to the instability of NPMCs is from flooding of micropores within the catalyst particles leading to significant mass transport limitations. While indirect evidence has been obtained that appears to support this hypothesis, no study has yet been performed to directly target micropore flooding. This investigation was achieved by comparing the degree of micropore flooding in-situ with the observed instability of a NPMC-based MEA. As a means to evaluate the degree of micropore flooding, the changes in the double layer capacitance following cyclic voltammetry were monitored throughout the test protocol and compared to the changes in air/O_2 polarization curves at various conditions. The CVs and specific capacitance calculation clearly show that the majority of the micropores are wetted at BOL, and although some degree of additional catalyst layer wetting occurs during the stability test, such a small increase cannot explain the significant performance loss that is observed. In addition, the loss in performance appears primarily kinetic and the mass transport loss due to flooded micropores appears relatively insignificant. The results do not support micropore flooding as being a large contributor to instability, at least for the family of NPMCs evaluated in this work. The protocol outlined here can be used by other researchers in the NPMC community to diagnose micropore flooding in their own respective catalysts.

6.2 Proposed future work

Based on the findings of these studies, some future directions for the catalysts research can be suggested:

1. High activity catalyst development

   Synthesis of NPMCs with different nitrogen precursors based on the high surface area carbon support such as graphene are encouraged. For TCNB or similar type precursors could be coupled with other high surface area support materials than mesoporous carbon particles to further confirm its ability to create well distributed active sites. For the graphene aerogel based catalysts, since not much research has been done on NPMCs with this type of support, various combinations of the currently known heteroatom or metal precursors will likely lead to a improvement of its activity. However, the activity and especially stability measured in RDE experiments may not reflect as well in the actual fuel cell test thus it should be tested in MEA as well.

2. With the protocol introduced in the last chapter, more investigation on different MEA compositions (varying amount of catalyst to nafion) or other types of catalysts can be done to get more insights. Carrying out the similar test with micro/mesoporous, mesoporous, and macroporous dominating catalysts while monitoring CVs will give more idea about the wetting and its relation to the stability. In addition, catalysts with more or less hydrophobic support would likely behave differently in this protocol, and along with amorphous or crystalline catalyst support (more or less prone to carbon oxidation) investigation could possibly give more information on the correlation between the stability loss and the carbon oxidation.

3. Pt and NPMCs hybrid catalysts

Although it's difficult to identify one single degradation mechanism for all NPMCs due to the variety of synthetic designs and methods, one of the degradation mechanisms for NPMCs that's widely accepted other than the micropore flooding is the losses due to oxidative attack by H_2O_2 and its radicals. Despite the effort, much more limited success has been achieved in mitigating the loss and no clear strategies have yet been discussed to address this challenge through a synthetic approach. Interestingly, among the materials that can catalyze the hydrogen peroxide, platinum is known to be an effective catalyst to facilitate peroxide decomposition with a minimal formation of hydroxyl radicals and may potentially assist in preventing the degradation of the NPMCs when used together with NPMC as a hybrid ORR catalyst. Hence, by combining platinum and NPMCs while achieving the optimal ratio and structural formation, a novel hybrid catalyst could be synthesized with its ORR activity supported by both NPMC active sites and low-loading platinum nanostructure, and with enhanced NPMC support durability by effective peroxide decomposition.

References

1. B. Thinnes, *Hydrocarb Process*, 2012, **91**, 17-19.
2. S. Shafiee and E. Topal, *Energ Policy*, 2009, **37**, 181-189.
3. F. C. Handbook, *Inc. November*, 2004.
4. J. Sinha, S. Lasher, Y. Yang and P. Kopf, *Fuel Cell Tech Team Review*, 2008.
5. J. Wu, X. Z. Yuan, J. J. Martin, H. Wang, J. Zhang, J. Shen, S. Wu and W. Merida, *J Power Sources*, 2008, **184**, 104-119.
6. L. Zhang, J. Zhang, D. P. Wilkinson and H. Wang, *J Power Sources*, 2006, **156**, 171-182.
7. C. W. B. Bezerra, L. Zhang, K. Lee, H. Liu, A. L. B. Marques, E. P. Marques, H. Wang and J. Zhang, *Electrochim Acta*, 2008, **53**, 4937-4951.
8. R. Jasinski, 1964.
9. M. Lefèvre, E. Proietti, F. Jaouen and J.-P. Dodelet, *Science (New York, N.Y.)*, 2009, **324**, 71-74.
10. DOE, Technical Plan - Fuel Cells, http://www1.eere.energy.gov/hydrogenandfuelcells/mypp/pdfs/fuel_cells.pdf.
11. H. Schulenburg, S. Stankov, V. Schünemann, J. Radnik, I. Dorbandt, S. Fiechter, P. Bogdanoff and H. Tributsch, *The Journal of Physical Chemistry B*, 2003, **107**, 9034-9041.
12. S. J. Ashton, in *Design, Construction and Research Application of a Differential Electrochemical Mass Spectrometer (DEMS)*, Springer Berlin Heidelberg, 2012, vol. 8, ch. 1, pp. 1-8.
13. J. Zhang, *PEM fuel cell electrocatalysts and catalyst layers: fundamentals and applications*, Springer, 2008.
14. J. Larminie, A. Dicks and Knovel, *Fuel cell systems explained, Second Edition*, John Wiley & Sons Ltd, West Sussex, England, 2003.

15. X. Li, G. Liu and B. N. Popov, *J Power Sources*, 2010, **195**, 6373-6378.

16. H. Meng, N. Larouche, M. Lefevre, F. Jaouen, B. Stansfield and J. P. Dodelet, *Electrochim Acta*, 2010, **55**, 6450-6461.

17. W. M. Li, A. P. Yu, D. C. Higgins, B. G. Llanos and Z. W. Chen, *J Am Chem Soc*, 2010, **132**, 17056-17058.

18. T. Palaniselvam, R. Kannan and S. Kurungot, *Chem Commun*, 2011, **47**, 2910-2912.

19. G. Wu, K. L. More, C. M. Johnston and P. Zelenay, *Science*, 2011, **332**, 443-447.

20. D. Ohms, S. Herzog, R. Franke, V. Neumann, K. Wiesener, S. Gamburcev, A. Kaisheva and I. Iliev, *J Power Sources*, 1992, **38**, 327-334.

21. A. Widelöv and R. Larsson, *Electrochim Acta*, 1992, **37**, 187-197.

22. R. Jiang and D. Chu, *J Electrochem Soc*, 2000, **147**, 4605-4609.

23. J. Maruyama and I. Abe, *J Electrochem Soc*, 2007, **154**, B297-B304.

24. D. Chu and R. Jiang, *Solid State Ionics*, 2002, **148**, 591-599.

25. K. Lee, L. Zhang, H. Lui, R. Hui, Z. Shi and J. Zhang, *Electrochim Acta*, 2009, **54**, 4704-4711.

26. M. Manzoli, R. D. Monte, F. Boccuzzi, S. Coluccia and J. Kašpar, *Applied Catalysis B: Environmental*, 2005, **61**, 192-205.

27. P. He, M. Lefevre, G. Faubert and J. Dodelet, *Journal of new materials for electrochemical systems*, 1999, **2**, 243-252.

28. S. Gupta, D. Tryk, I. Bae, W. Aldred and E. Yeager, *J. Appl. Electrochem.*, 1989, **19**, 19-27.

29. K. Sawai and N. Suzuki, *J Electrochem Soc*, 2004, **151**, A682-A688.

30. P. H. Matter, L. Zhang and U. S. Ozkan, *J Catal*, 2006, **239**, 83-96.

31. R. Bashyam and P. Zelenay, *Nature*, 2006, **443**, 63-66.

32. J. Y. Choi, R. S. Hsu and Z. W. Chen, *J Phys Chem C*, 2010, **114**, 8048-8053.

33. G. Liu, X. Li, P. Ganesan and B. N. Popov, *Electrochim. Acta*, 2010, **55**, 2853-2858.

34. V. Nallathambi, J.-W. Lee, S. P. Kumaraguru, G. Wu and B. N. Popov, *J Power Sources*, 2008, **183**, 34-42.

35. N. P. Subramanian, S. P. Kumaraguru, H. Colon-Mercado, H. Kim, B. N. Popov, T. Black and D. A. Chen, *J Power Sources*, 2006, **157**, 56-63.

36. B. N. Popov, X. Li, G. Liu and J.-W. Lee, *Int J Hydrogen Energ*, 2011, **36**, 1794-1802.

37. T. E. Wood, Z. Tan, A. K. Schmoeckel, D. O'Neill and R. Atanasoski, *J Power Sources*, 2008, **178**, 510-516.

38. G. Wu, C. M. Johnston, N. H. Mack, K. Artyushkova, M. Ferrandon, M. Nelson, J. S. Lezama-Pacheco, S. D. Conradson, K. L. More, D. J. Myers and P. Zelenay, *J Mater Chem*, 2011.

39. R. Cote, G. Lalande, G. Faubert, D. Guay, J. Dodelet and G. Denes, *Journal of new materials for electrochemical systems*, 1998, **1**, 7-16.

40. M. M. Alves, J. Dodelet, D. Guay, M. Ladouceur and G. Tourillon, *The Journal of Physical Chemistry*, 1992, **96**, 10898-10905.

41. A. Bouwkamp-Wijnoltz, W. Visscher, J. Van Veen and S. Tang, *Electrochim Acta*, 1999, **45**, 379-386.

42. G. Faubert, R. Cote, D. Guay, J. Dodelet, G. Denes and P. Bertrandc, *Electrochim Acta*, 1998, **43**, 341-353.

43. X. Wang, J. S. Lee, Q. Zhu, J. Liu, Y. Wang and S. Dai, *Chemistry of Materials*, 2010, **22**, 2178-2180.

44. M. Bron, S. Fiechter, M. Hilgendorff and P. Bogdanoff, *Journal of applied electrochemistry*, 2002, **32**, 211-216.

45. F. Jaouen, S. Marcotte, J.-P. Dodelet and G. Lindbergh, *The Journal of Physical Chemistry B*, 2003, **107**, 1376-1386.

46. M. Lefevre, J. Dodelet and P. Bertrand, *The Journal of Physical Chemistry B*, 2005, **109**, 16718-16724.

47. M. Lefèvre and J.-P. Dodelet, *Electrochimica Acta*, 2003, **48**, 2749-2760.

48. C. Medard, M. Lefevre, J. Dodelet, F. Jaouen and G. Lindbergh, *Electrochim Acta*, 2006, **51**, 3202-3213.

49. F. Charreteur, F. Jaouen and J.-P. Dodelet, *Electrochim Acta*, 2009, **54**, 6622-6630.

50. Z. Wen, J. Liu and J. Li, *Advanced Materials*, 2008, **20**, 743-747.

51. S. H. Joo, C. Pak, D. J. You, S.-A. Lee, H. I. Lee, J. M. Kim, H. Chang and D. Seung, *Electrochim Acta*, 2006, **52**, 1618-1626.

52. E. P. Ambrosio, C. Francia, M. Manzoli, N. Penazzi and P. Spinelli, *Int J Hydrogen Energ*, 2008, **33**, 3142-3145.

53. J. B. Joo, P. Kim, W. Kim, J. Kim and J. Yi, *Catalysis Today*, 2006, **111**, 171-175.

54. Z. Chen, D. Higgins, H. Tao, R. S. Hsu and Z. Chen, *The Journal of Physical Chemistry C*, 2009, **113**, 21008-21013.

55. K. Gong, F. Du, Z. Xia, M. Durstock and L. Dai, *Science*, 2009, **323**, 760-764.

56. D. C. Higgins, D. Meza and Z. W. Chen, *J Phys Chem C*, 2010, **114**, 21982-21988.

57. W. Li, C. Liang, W. Zhou, J. Qiu, Zhou, G. Sun and Q. Xin, *The Journal of Physical Chemistry B*, 2003, **107**, 6292-6299.

58. Y. Lin, X. Cui, C. Yen and C. M. Wai, *The Journal of Physical Chemistry B*, 2005, **109**, 14410-14415.

59. W. Zhang, P. Sherrell, A. I. Minett, J. M. Razal and J. Chen, *Energ Environ Sci*, 2010, **3**, 1286-1293.

60. J. Guo, G. Sun, Q. Wang, G. Wang, Z. Zhou, S. Tang, L. Jiang, B. Zhou and Q. Xin, *Carbon*, 2006, **44**, 152-157.

61. S. Maldonado and K. J. Stevenson, *The Journal of Physical Chemistry B*, 2005, **109**, 4707-4716.

62. K. Lee, J. Zhang, H. Wang and D. P. Wilkinson, *Journal of applied electrochemistry*, 2006, **36**, 507-522.

63. D. Deng, L. Yu, X. Chen, G. Wang, L. Jin, X. Pan, J. Deng, G. Sun and X. Bao, *Angewandte Chemie International Edition*, 2013, **52**, 371-375.

64. A. J. A. Wang and K. Qian, in *Component-Oriented Programming*, John Wiley & Sons, Inc., 2005, pp. 1-15.

65. Y. Shao, G. Yin and Y. Gao, *Journal of Power Sources*, 2007, **171**, 558-566.

66. R. Borup, J. Meyers, B. Pivovar, Y. Kim, R. Mukundan, N. Garland, D. Myers, M. Wilson, F. Garzon and D. Wood, *Chemical Reviews*, 2007, **107**, 3904-3951.

67. F. Jaouen and J.-P. Dodelet, *The Journal of Physical Chemistry C*, 2007, **111**, 5963-5970.

68. J. Goldstein, D. E. Newbury, D. C. Joy, C. E. Lyman, P. Echlin, E. Lifshin, L. Sawyer and J. R. Michael, *Scanning electron microscopy and X-ray microanalysis*, Springer, 2003.

69. H. Seiler, *J Appl Phys*, 1983, **54**, R1-R18.

70. M. A. Sutton, N. Li, D. C. Joy, A. P. Reynolds and X. Li, *Exp Mech*, 2007, **47**, 775-787.

71. D. B. Williams and C. B. Carter, *The Transmission Electron Microscope*, Springer, 1996.

72. D. B. Williams and C. B. Carter, in *Transmission Electron Microscopy*, Springer, 2009, pp. 3-22.

73. D. Alloyeau, in *Nanoalloys*, eds. D. Alloyeau, C. Mottet and C. Ricolleau, Springer London, 2012, ch. 4, pp. 113-157.

74. B. E. Warren, *X-ray Diffraction*, Courier Dover Publications, 1969.

75. L. V. Azároff, R. Kaplow, N. Kato, R. J. Weiss, A. Wilson and R. Young, *X-ray Diffraction*, McGraw-Hill New York, 1974.

76. C. Fadley and S. Davison, *Vol. 16Pergamon, New York*, 1984, 275.

77. C. Fadley, R. Baird, W. Siekhaus, T. Novakov and S. Bergström, *Journal of Electron Spectroscopy and Related Phenomena*, 1974, **4**, 93-137.

78. D. W. Turner and M. A. Jobory, *The Journal of Chemical Physics*, 1962, **37**, 3007-3008.

79. S. Brunauer, P. H. Emmett and E. Teller, *J Am Chem Soc*, 1938, **60**, 309-319.

80. W. Schmickler and E. Santos, in *Interfacial Electrochemistry*, Springer Berlin Heidelberg, 2010, ch. 20, pp. 259-267.

81. J.-Y. Choi, D. U. Lee and Z. Chen, *Ecs Transactions*, 2013, **50**, 1815-1822.

82. J. W. Weidner, V. A. Sethuraman and J. W. Van Zee, *Electrochemical Society Interface*, 2003, 41-47.

83. Z. Chen, D. Higgins, A. Yu, L. Zhang and J. Zhang, *Energy Environ. Sci.*, 2011, **4**, 3167-3192.

84. F. Jaouen, E. Proietti, M. Lefevre, R. Chenitz, J.-P. Dodelet, G. Wu, H. T. Chung, C. M. Johnston and P. Zelenay, *Energy Environ. Sci.*, 2011, **4**, 114-130.

85. D. C. Higgins and Z. Chen, *Canadian J. Chem. Eng.*, 2013, **91**, 1881-1895.

86. R. Jasinski, *Nature*, 1964, **201**, 1212-1213.

87. R. Franke, D. Ohms and K. Wiesener, *J. Electroanal. Chem. Inter. Electrochem.*, 1989, **260**, 63-73.

88. J. A. R. van Veen, H. A. Colijn and J. F. van Baar, *Electrochim. Acta*, 1988, **33**, 801-804.

89. K. Wiesener, *Electrochim. Acta*, 1986, **31**, 1073-1078.

90. G. Wu and P. Zelenay, *Acc. Chem. Res.*, 2013, **46**, 1878-1889.

91. H. T. Chung, C. M. Johnston, K. Artyushkova, M. Ferrandon, D. J. Myers and P. Zelenay, *Electrochem. Commun.*, 2010, **12**, 1792-1795.

92. E. Proietti, F. Jaouen, M. Lefèvre, N. Larouche, J. Tian, J. Herranz and J.-P. Dodelet, *Nat. Commun.*, 2011, **2**, 416.

93. M. Lefèvre, E. Proietti, F. Jaouen and J.-P. Dodelet, *Science*, 2009, **324**, 71-74.

94. J.-Y. Choi, D. Higgins and Z. Chen, *J. Electrochem. Soc.*, 2011, **159**, B86-B89.

95. J. Wu, W. Li, D. Higgins and Z. Chen, *The Journal of Physical Chemistry C*, 2011, **115**, 18856-18862.

96. M. Ladouceur, G. Lalande, D. Guay, J. P. Dodelet, L. Dignard-Bailey, M. L. Trudeau and R. Schulz, *J. Electrochem. Soc.*, 1993, **140**, 1974-1981.

97. L. Dignard-Bailey, M. L. Trudeau, R. S. A. Joly, G. Lalande, D. Guay and J. P. Dodelet, *J. Mater. Res*, 1994, 3203-3209.

98. L. T. Weng, P. Bertrand, G. Lalande, D. Guay and J. P. Dodelet, *Appl. Surf. Sci*, 1995, **84**, 9-21.

99. G. Lalande, G. Faubert, R. Cote, D. Guay, J. P. Dodelet, L. T. Weng and P. Bertrand, *J. Power Sources*, 1996, **61**, 227-237.

100. G. Lalande, R. Côté, G. Tamizhmani, D. Guay, J. P. Dodelet, L. Dignard-Bailey, L. T. Weng and P. Bertrand, *Electrochim. Acta*, 1995, **40**, 2635-2646.

101. M. Abel, S. Clair, O. Ourdjini, M. Mossoyan and L. Porte, *J. Am. Chem. Soc.*, 2010, **133**, 1203-1205.

102. W. He and M. Lieberman, *J. Porphyrins Phthalocyanines*, 2011, **15**, 277-292.

103. D. R. Boston and J. C. Bailar, *Inorg. Chem.*, 1972, **11**, 1578-1583.

104. J. Choi, R. Hsu and Z. Chen, *The Journal of Physical Chemistry C*, 2010, **114**, 8048-8053.

105. D. Lelievre, L. Bosio, J. Simon, J. J. Andre and F. Bensebaa, *Journal of the American Chemical Society*, 1992, **114**, 4475-4479.

106. R. Bannehr, G. Meyer and D. Wöhrle, *Polymer Bulletin*, 1980, **2**, 841-846.

107. Z. Liu, X. Zhang, Y. Zhang and J. Jiang, *Spectrochimica Acta Part A: Molecular and Biomolecular Spectroscopy*, 2007, **67**, 1232-1246.

108. R. Aroca and A. Thedchanamoorthy, *Chemistry of Materials*, 1995, **7**, 69-74.

109. L. Gaffo, C. Constantino, W. Moreira, R. Aroca and O. Oliveira, *Journal of Raman Spectroscopy*, 2002, **33**, 833-837.

110. D. R. Tackley, G. Dent and W. E. Smith, *Physical Chemistry Chemical Physics*, 2001, **3**, 1419-1426.

111. G. Faubert, G. Lalande, R. Côté, D. Guay, J. P. Dodelet, L. T. Weng, P. Bertrand and G. Dénès, *Electrochim. Acta*, 1996, **41**, 1689-1701.

112. F. Jaouen, F. Charreteur and J. P. Dodelet, *J. Electrochem. Soc.*, 2006, **153**, A689-A698.

113. M. Lefèvre and J. P. Dodelet, *Electrochim. Acta*, 2003, **48**, 2749-2760.

114. M. Lefèvre and J. P. Dodelet, *Electrochim. Acta*, 2008, **53**, 8269-8276.

115. E. B. Easton, A. Bonakdarpour and J. R. Dahn, *Electrochem. Solid-State Lett.*, 2006, **9**, A463-A467.

116. D. Higgins, Z. Chen and Z. Chen, *Electrochim. Acta*, 2011, **56**, 1570-1575.

117. D. C. Higgins, J. Wu, W. Li and Z. Chen, *Electrochim. Acta*, 2012, **59**, 8-13.

118. Z. Chen, D. Higgins and Z. Chen, *Carbon*, 2010, **48**, 3057-3065.

119. R. Liu, D. Wu, X. Feng and K. Müllen, *Angew. Chem.*, 2010, **122**, 2619-2623.

120. X. Li, H. Wang, J. T. Robinson, H. Sanchez, G. Diankov and H. Dai, *J. Am. Chem. Soc.*, 2009, **131**, 15939-15944.

121. K. Jia, R. Zhao, J. Zhong and X. Liu, *Journal of Materials Science: Materials in Electronics*, 2010, **21**, 708-712.

122. R. Seoudi, G. El-Bahy and Z. El Sayed, *Journal of Molecular Structure*, 2005, **753**, 119-126.

123. W. Lu, B. Zhao, N. Li, Y. Yao and W. Chen, *Reactive and Functional Polymers*, 2010, **70**, 135-141.

124. C. Zhang, R. Hao, H. Yin, F. Liu and Y. Hou, *Nanoscale*, 2012, **4**, 7326-7329.

125. E. Charon, J. N. Rouzaud and J. Aléon, *Carbon*, 2014, **66**, 178-190.

126. R. Jasinski, *Nature*, 1964, **201**, 1212.

127. N. Cheng, M. N. Banis, J. Liu, A. Riese, X. Li, R. Li, S. Ye, S. Knights and X. Sun, *Adv. Mater.*, 2015, **27**, 277.

128. D. Higgins, M. A. Hoque, M. H. Seo, R. Wang, F. Hassan, J. Y. Choi, M. Pritzker, A. Yu, J. Zhang and Z. Chen, *Adv. Funct. Mater.*, 2014, **24**, 4325.

129. B. Y. Xia, H. B. Wu, N. Li, Y. Yan, X. W. Lou and X. Wang, *Angew. Chem., Int. Ed.*, 2015, **54**, 3797.

130. X. Fu, J. Jin, Y. Liu, Z. Wei, F. Pan and J. Zhang, *ACS Appl. Mater. Interfaces*, 2014, **6**, 3930.

131. W. Li, A. Yu, D. C. Higgins, B. G. Llanos and Z. Chen, *J. Am. Chem. Soc.*, 2010, **132**, 17056.

132. A. Serov, M. H. Robson, B. Halevi, K. Artyushkova and P. Atanassov, *Electrochem. Commun.*, 2012, **22**, 53.

133. D. S. Su and G. Sun, *Angew. Chem., Int. Ed.*, 2011, **50**, 11570.

134. G. Wu and P. Zelenay, *Acc. Chem. Res.*, 2013, **46**, 1878.

135. H. R. Byon, J. Suntivich and Y. Shao-Horn, *Chem. Mater.*, 2011, **23**, 3421.

136. D. Geng, Y. Chen, Y. Li, R. Li, X. Sun, S. Ye and S. Knights, *Energy Environ. Sci.*, 2011, **4**, 760.

137. K. Gong, F. Du, Z. Xia, M. Durstock and L. Dai, *Science*, 2009, **323**, 760.

138. S. Li, D. Wu, H. Liang, J. Wang, X. Zhuang, Y. Mai, Y. Su and X. Feng, *ChemSusChem*, 2014, **7**, 3002.

139. R. Liu, D. Wu, X. Feng and K. Müllen, *Angew. Chem., Int. Ed.*, 2010, **49**, 2565.

140. D. Higgins, P. Zamani, A. Yu and Z. Chen, *Energy Environ. Sci.*, 2016, **9**, 357.

141. S. Jiang, C. Zhu and S. Dong, *J. Mater. Chem. A*, 2013, **1**, 3593.

142. M. Liu, R. Zhang and W. Chen, *Chem. Rev.*, 2014, **114**, 5117.

143. F. Pan, J. Jin, X. Fu, Q. Liu and J. Zhang, *ACS Appl. Mater. Interfaces*, 2013, **5**, 11108.

144. Y. Shao, S. Zhang, M. H. Engelhard, G. Li, G. Shao, Y. Wang, J. Liu, I. A. Aksay and Y. Lin, *J. Mater. Chem.*, 2010, **20**, 7491.

145. H. Wang, T. Maiyalagan and X. Wang, *ACS Catal.*, 2012, **2**, 781.

146. C. W. B. Bezerra, L. Zhang, K. Lee, H. Liu, A. L. B. Marques, E. P. Marques, H. Wang and J. Zhang, *Electrochim. Acta*, 2008, **53**, 4937.

147. C. He, J. J. Zhang and P. K. Shen, *J. Mater. Chem. A*, 2014, **2**, 3231.

148. A. L. Bouwkamp-Wijnoltz, W. Visscher, J. A. R. van Veen, E. Boellaard, A. M. van der Kraan and S. C. Tang, *J. Phys. Chem. B*, 2002, **106**, 12993.

149. D. Deng, L. Yu, X. Chen, G. Wang, L. Jin, X. Pan, J. Deng, G. Sun and X. Bao, *Angew. Chem., Int. Ed.*, 2013, **52**, 371.

150. Y. Hu, J. O. Jensen, W. Zhang, L. N. Cleemann, W. Xing, N. J. Bjerrum and Q. Li, *Angew. Chem., Int. Ed.*, 2014, **53**, 3675.

151. D. H. Lee, W. J. Lee, S. O. Kim and Y. H. Kim, *Phys. Rev. Lett.*, 2011, **106**, 175502.

152. M. Lefèvre, J. P. Dodelet and P. Bertrand, *J. Phys. Chem. B*, 2005, **109**, 16718.

153. M. Lefèvre, E. Proietti, F. Jaouen and J. P. Dodelet, *Science*, 2009, **324**, 71.

154. M. S. Thorum, J. M. Hankett and A. A. Gewirth, *J. Phys. Chem. Lett.*, 2011, **2**, 295.

155. H. W. Liang, W. Wei, Z. S. Wu, X. Feng and K. Müllen, *J. Am. Chem. Soc.*, 2013, **135**, 16002.

156. Z. W. Chen, D. Higgins, A. P. Yu, L. Zhang and J. J. Zhang, *Energy Environ. Sci.*, 2011, **4**, 3167.

157. R. Zhang, S. He, Y. Lu and W. Chen, *J. Mater. Chem. A*, 2015, **3**, 3559.

158. X. Bo, M. Li, C. Han, Y. Zhang, A. Nsabimana and L. Guo, *J. Mater. Chem. A*, 2015, **3**, 1058.

159. K. Parvez, S. Yang, Y. Hernandez, A. Winter, A. Turchanin, X. Feng and K. Müllen, *ACS Nano*, 2012, **6**, 9541.

160. Y. Jiang, Y. Lu, X. Wang, Y. Bao, W. Chen and L. Niu, *Nanoscale*, 2014, **6**, 15066.

161. M. Wang, J. Wang, Y. Hou, D. Shi, D. Wexler, S. D. Poynton, R. C. T. Slade, W. Zhang, H. Liu and J. Chen, *ACS Appl. Mater. Interfaces*, 2015, **7**, 7066.

162. Z. S. Wu, S. Yang, Y. Sun, K. Parvez, X. Feng and K. Mullen, *J. Am. Chem. Soc.*, 2012, **134**, 9082.

163. Y. Zhao, C. Hu, Y. Hu, H. Cheng, G. Shi and L. Qu, *Angew. Chem.*, 2012, **124**, 11533.

164. C. Vallès, P. Jimènez, E. Muñoz, A. M. Benito and W. K. Maser, *J. Phys. Chem. C*, 2011, **115**, 10468.

165. G. Wu, Z. Chen, K. Artyushkova, F. H. Garzon and P. Zelenay, *ECS Trans.*, 2008, **16**, 159.

166. G. Wu, C. M. Johnston, N. H. Mack, K. Artyushkova, M. Ferrandon, M. Nelson, J. S. Lezama-Pacheco, S. D. Conradson, K. L. More, D. J. Myers and P. Zelenay, *J. Mater. Chem.*, 2011, **21**, 11392.

167. G. Wu, K. L. More, C. M. Johnston and P. Zelenay, *Science*, 2011, **332**, 443.

168. J. Liang, X. Du, C. Gibson, X. W. Du and S. Z. Qiao, *Adv. Mater.*, 2013, **25**, 6226.

169. S. L. Gojković, S. Gupta and R. F. Savinell, *Electrochim. Acta*, 1999, **45**, 889.

170. Y. Nabae, S. Moriya, K. Matsubayashi, S. M. Lyth, M. Malon, L. Wu, N. M. Islam, Y. Koshigoe, S. Kuroki, M. a. Kakimoto, S. Miyata and J. i. Ozaki, *Carbon*, 2010, **48**, 2613.

171. J. Liang, Y. Zheng, J. Chen, J. Liu, D. Hulicova-Jurcakova, M. Jaroniec and S. Z. Qiao, *Angew. Chem., Int. Ed.*, 2012, **51**, 3892.

172. K. N. Kudin, B. Ozbas, H. C. Schniepp, R. K. Prud'homme, I. A. Aksay and R. Car, *Nano Lett.*, 2008, **8**, 36.

173. F. d. r. Jaouen, J. Herranz, M. Lefèvre, J. P. Dodelet, U. I. Kramm, I. Herrmann, P. Bogdanoff, J. Maruyama, T. Nagaoka, A. Garsuch, J. R. Dahn, T. Olson, S. Pylypenko, P. Atanassov and E. A. Ustinov, *ACS Appl. Mater. Interfaces*, 2009, **1**, 1623.

174. A. Morozan, P. Jegou, B. Jousselme and S. Palacin, *Phys. Chem. Chem. Phys.*, 2011, **13**, 21600.

175. K. Artyushkova, S. Levendosky, P. Atanassov and J. Fulghum, *Top. Catal.*, 2007, **46**, 263.

176. R. L. Arechederra, K. Artyushkova, P. Atanassov and S. D. Minteer, *ACS Appl. Mater. Interfaces*, 2010, **2**, 3295.

177. J. M. Ziegelbauer, T. S. Olson, S. Pylypenko, F. Alamgir, C. Jaye, P. Atanassov and S. Mukerjee, *J. Phys. Chem. C*, 2008, **112**, 8839.

178. S. Pylypenko, S. Mukherjee, T. S. Olson and P. Atanassov, *Electrochim. Acta*, 2008, **53**, 7875.

179. D. Ohms, S. Herzog, R. Franke, V. Neumann, K. Wiesener, S. Gamburcev, A. Kaisheva and I. Iliev, *J. Power Sources*, 1992, **38**, 327.

180. G. Wu, K. Artyushkova, M. Ferrandon, A. J. Kropf, D. Myers and P. Zelenay, *ECS Trans.*, 2009, **25**, 1299.

181. G. Liu, X. G. Li, J. W. Lee and B. N. Popov, *Catal. Sci. Technol.*, 2011, **1**, 207.

182. J. Herranz, F. d. r. Jaouen, M. Lefèvre, U. I. Kramm, E. Proietti, J. P. Dodelet, P. Bogdanoff, S. Fiechter, I. Abs-Wurmbach, P. Bertrand, T. M. Arruda and S. Mukerjee, *J. Phys. Chem. C*, 2011, **115**, 16087.

183. F. Barbir, *PEM Fuel Cells: Theory and Practice*, Elsevier Academic Press, 2005.

184. E. Proietti, F. Jaouen, M. Lefèvre, N. Larouche, J. Tian, J. Herranz and J.-P. Dodelet, *Nature Communications*, 2011, **2**.

185. A. Serov, K. Artyushkova, E. Niangar, C. Wang, N. Dale, F. Jaouen, M.-T. Sougrati, Q. Jia, S. Mukerjee and P. Atanassov, *Nano Energy*, 2015, **16**, 293-300.

186. P. Zamani, D. C. Higgins, F. M. Hassan, X. Fu, J.-Y. Choi, M. A. Hoque, G. Jiang and Z. Chen, *Nano Energy*, 2016, **26**, 267-275.

187. D. Banham, S. Ye, K. Pei, J.-i. Ozaki, T. Kishimoto and Y. Imashiro, *Journal of Power Sources*, 2015, **285**, 334-348.

188. L. Birry, J. H. Zagal and J.-P. Dodelet, *Electrochemistry Communications*, 2010, **12**, 628-631.

189. M. Lefèvre, J. P. Dodelet and P. Bertrand, *The Journal of Physical Chemistry B*, 2002, **106**, 8705-8713.

190. J. Herranz, F. Jaouen and J.-P. Dodelet, *ECS Transactions*, 2009, **25**, 117-128.

191. N. R. Sahraie, U. I. Kramm, J. Steinberg, Y. Zhang, A. Thomas, T. Reier, J. P. Paraknowitsch and P. Strasser, *Nat Commun*, 2015, **6**, 8618.

192. E. F. Holby and C. D. Taylor, *Scientific Reports*, 2015, **5**, 9286.

193. A. Serov, M. H. Robson, K. Artyushkova and P. Atanassov, *Applied Catalysis B: Environmental*, 2012, **127**, 300-306.

194. Z. M. Hongliang Peng, Shijun Liao, Huagen Liang, Lijun Yang, Fan Luo, Huiyu Song, Yiliang Zhong, Bingqing Zhang, *Scientific Reports*, 2013, **3**.

195. B. Wang, *Journal of Power Sources*, 2005, **152**, 1-15.

196. C. H. Choi, C. Baldizzone, G. Polymeros, E. Pizzutilo, O. Kasian, A. K. Schuppert, N. Ranjbar Sahraie, M.-T. Sougrati, K. J. J. Mayrhofer and F. Jaouen, *ACS Catalysis*, 2016, **6**, 3136-3146.

197. J. A. Varnell, E. C. Tse, C. E. Schulz, T. T. Fister, R. T. Haasch, J. Timoshenko, A. I. Frenkel and A. A. Gewirth, *Nat Commun*, 2016, **7**, 12582.

198. C. H. Choi, C. Baldizzone, J.-P. Grote, A. K. Schuppert, F. Jaouen and K. J. J. Mayrhofer, *Angewandte Chemie International Edition*, 2015, n/a-n/a.

199. V. Goellner, V. Armel, A. Zitolo, E. Fonda and F. Jaouen, *Journal of the Electrochemical Society*, 2015, **162**, H403-H414.

200. G. Liu, X. Li and B. Popov, *ECS Transactions*, 2009, **25**, 1251-1259.

201. J. Herranz, F. Jaouen, M. Lefèvre, U. I. Kramm, E. Proietti, J.-P. Dodelet, P. Bogdanoff, S. Fiechter, I. Abs-Wurmbach, P. Bertrand, T. M. Arruda and S. Mukerjee, *The Journal of Physical Chemistry C*, 2011, **115**, 16087-16097.

202. G. Zhang, R. Chenitz, M. Lefèvre, S. Sun and J.-P. Dodelet, *Nano Energy*, 2016.

203. M. Shao, Q. Chang, J. P. Dodelet and R. Chenitz, *Chem Rev*, 2016.

204. L. Yang, N. Larouche, R. Chenitz, G. Zhang, M. Lefèvre and J.-P. Dodelet, *Electrochimica Acta*, 2015, **159**, 184-197.

205. Y.-C. Wang, Y.-J. Lai, L. Song, Z.-Y. Zhou, J.-G. Liu, Q. Wang, X.-D. Yang, C. Chen, W. Shi, Y.-P. Zheng, M. Rauf and S.-G. Sun, *Angewandte Chemie International Edition*, 2015, **54**, 9907-9910.

206. F. Jaouen, M. Lefèvre, J.-P. Dodelet and M. Cai, *The Journal of Physical Chemistry B*, 2006, **110**, 5553-5558.

207. F. Jaouen and J.-P. Dodelet, *Electrochimica Acta*, 2007, **52**, 5975-5984.

208. F. d. r. Jaouen, J. Herranz, M. Lefèvre, J.-P. Dodelet, U. I. Kramm, I. Herrmann, P. Bogdanoff, J. Maruyama, T. Nagaoka, A. Garsuch, J. R. Dahn, T. Olson, S. Pylypenko, P. Atanassov and E. A. Ustinov, *ACS Applied Materials & Interfaces*, 2009, **1**, 1623-1639.

209. W. Li, A. Yu, D. C. Higgins, B. G. Llanos and Z. Chen, *J. Am. Chem. Soc.*, 2010, **132**, 17056-17058.

210. H. A. Gasteiger and N. M. Marković, *Science*, 2009, **324**, 48-49.

211. Y.-C. Wang, Y.-J. Lai, L. Song, Z.-Y. Zhou, J.-G. Liu, Q. Wang, X.-D. Yang, C. Chen, W. Shi, Y.-P. Zheng, M. Rauf and S.-G. Sun, *Angew. Chem. Int. Ed.*, 2015, **54**, 9907–9910.

212. X. Fu, J.-Y. Choi, P. Zamani, G. Jiang, M. A. Hoque, F. M. Hassan and Z. Chen, *ACS Applied Materials & Interfaces*, 2016, **8**, 6488-6495.

213. D. C. Higgins and Z. Chen, *The Canadian Journal of Chemical Engineering*, 2013, **91**, 1881-1895.

214. P. Zamani, D. Higgins, F. Hassan, G. Jiang, J. Wu, S. Abureden and Z. Chen, *Electrochim. Acta*, 2014, **139**, 111-116.

215. X. Fu, Y. Liu, X. Cao, J. Jin, Q. Liu and J. Zhang, *Applied Catalysis B: Environmental*, 2013, **130-131**, 143-151.

216. W. Ding, L. Li, K. Xiong, Y. Wang, W. Li, Y. Nie, S. Chen, X. Qi and Z. Wei, *J. Am. Chem. Soc.*, 2015, **137**, 5414–5420.

217. M. Zhou, C. Yang and K.-Y. Chan, *Advanced Energy Materials*, 2014, **4**, 1400840.

218. G. He, M. Qiao, W. Li, Y. Lu, T. Zhao, R. Zou, B. Li, J. A. Darr, J. Hu, M.-M. Titirici and I. P. Parkin, *Advanced Science*, 2016, 1600214.

219. E. Proietti, F. Jaouen, M. Lefèvre, N. Larouche, J. Tian, J. Herranz and J.-P. Dodelet, *Nat Commun*, 2011, **2**, 416.

220. G. Wu, K. L. More, P. Xu, H.-L. Wang, M. Ferrandon, A. J. Kropf, D. J. Myers, S. Ma, C. M. Johnston and P. Zelenay, *Chem. Commun.*, 2013, **49**, 3291-3293.

221. G. Wu, C. M. Johnston, N. H. Mack, K. Artyushkova, M. Ferrandon, M. Nelson, J. S. Lezama-Pacheco, S. D. Conradson, K. L. More, D. J. Myers and P. Zelenay, *J. Mater. Chem.*, 2011, **21**, 11392-11405.

222. D. S. Su and G. Sun, *Angew. Chem. Int. Ed.*, 2011, **50**, 11570-11572.

223. Z. W. Chen, D. Higgins, A. P. Yu, L. Zhang and J. J. Zhang, *Energy Environ. Sci.*, 2011, **4**, 3167-3192.

224. G. Wu, N. H. Mack, W. Gao, S. Ma, R. Zhong, J. Han, J. K. Baldwin and P. Zelenay, *ACS Nano*, 2012, **6**, 9764-9776.

225. G. Wu, M. A. Nelson, N. H. Mack, S. Ma, P. Sekhar, F. H. Garzon and P. Zelenay, *Chem. Commun.*, 2010, **46**, 7489-7491.

226. D. B. Spry, A. Goun, K. Glusac, D. E. Moilanen and M. D. Fayer, *Journal of the American Chemical Society*, 2007, **129**, 8122-8130.

227. T. D. Gierke, G. E. Munn and F. C. Wilson, *Journal of Polymer Science: Polymer Physics Edition,*, 1981, **19**, 1687-1704.

228. E. Antolini, *Applied Catalysis B: Environmental*, 2009, **88**, 1-24.

229. M. Uchida, Y. Fukuoka, Y. Sugawara, N. Eda and A. Ohta, *Journal of The Electrochemical Society*, 1996, **143**, 2245-2252.

230. K. Shinozaki, H. Yamada and Y. Morimoto, *Journal of The Electrochemical Society*, 2011, **158**, B467-B475.

231. J. Bockris, A. Reddy and M. Gamboa-Aldeco, *Modern Electrochemistry 2A Fundamentals of Electrodics*, Kluwer Academic/Plenum Publishers, New York, 2000.

232. S. Lowell, J. E. Shields, M. A. Thomas and M. Thommes, *Characterization of Porous Solids and Powders: Surface Area, Pore Size and Density*, Springer, Dordrecht, Netherlands, 2006.

233. S. Komini Babu, H. T. Chung, G. Wu, P. Zelenay and S. Litster, *ECS Transactions*, 2014, **64**, 281-292.

234. D. Banham, F. Feng, J. Burt, E. Alsrayheen and V. Birss, *Carbon*, 2010, **48**, 1056-1063.

235. A. Young, J. Stumper, S. Knights and E. Gyenge, *Journal of The Electrochemical Society*, 2010, **157**, B425-B436.

236. N. Larouche, R. Chenitz, M. Lefèvre, E. Proietti and J.-P. Dodelet, *Electrochimica Acta*, 2014, **115**, 170-182.

237. J. Maruyama and I. Abe, *Chemistry of Materials*, 2005, **17**, 4660-4667.

238. M. Ferrandon, X. Wang, A. J. Kropf, D. J. Myers, G. Wu, C. M. Johnston and P. Zelenay, *Electrochimica Acta*, 2013, **110**, 282-291.

239. G. Wu, K. Artyushkova, M. Ferrandon, A. J. Kropf, D. Myers and P. Zelenay, *ECS Transactions*, 2009, **25**, 1299-1311.